Neutral kaon femtoscopy in Pb-Pb collisions at $\sqrt{s_{\mathrm{NN}}} = 2.76$ TeV at the LHC with ALICE

DISSERTATION

Presented in Partial Fulfillment of the Requirements for the Degree Doctor of Philosophy in the Graduate School of The Ohio State University

By

Matthew Steinpreis, M.S., B.S.

Graduate Program in Physics

The Ohio State University

2014

Dissertation Committee:

Professor Thomas Humanic, Advisor

Professor Michael Lisa

Professor Yuri Kovchegov

Professor Klaus Honscheid

Abstract

Femtoscopy is an experimental method used to study the spatio-temporal characteristics of the particle-emitting "sources" of ultra-relativistic particle collisions. This method allows us to measure the size, shape, and lifetime of the kinetic freeze-out region of the particles created in the collisions as they are emitted from the expanding system. Studying these source regions allows us to investigate the dynamics of the system as it evolves from the hot, dense state of matter known as the Quark-Gluon Plasma into a dilute, free-streaming hadronic gas. The analysis of the extracted femtoscopic radii and their dependences on event centrality, momentum, and particle species can help put constaints on unknown quantities used in theoretical models such as time-scales and particle-particle scattering parameters. The femtoscopic tool is the two-particle relative momentum correlation function, which connects the final-state momentum distributions measured by the detector to the space-time distributions of particle emission, which are on the order of 10^{-15} m, or femtometers, and cannot be directly measured. These correlations are sensitive to the quantum statistics of identical particles as well as the strong and/or Coulomb interactions between particles.

Neutral kaon femtoscopy acts as an excellent complement to similar analyses of other particle species. Kaon analyses are generally able to reach higher values of transverse momentum (K_{T}) and transverse mass ($M_{\mathrm{T}} = \sqrt{K_{\mathrm{T}}^2 + m^2}$) than the more commonly studied pion analyses. The comparison of kaon radii with those of pions and protons allows us to check for universal M_{T}-scaling, which is predicted by some hydrodynamic models. The study of neutral kaons also acts as a convenient consistency check for the charged kaon analysis, as both analyses are expected to produce similar results while employing significantly different analysis methods, e.g. directly measured tracks vs. decay vertex reconstruction

and Coulomb-dominated vs. strong-dominated final-state interactions.

This thesis will present $K^0_S K^0_S$ femtoscopic correlations in Pb-Pb collisions at $\sqrt{s_{NN}} = 2.76$ TeV at the LHC with ALICE. This analysis will be the first centrality- and K_T-differential study of $K^0_S K^0_S$ correlations in heavy-ion collisions, presenting femtoscopic results for three centrality bins and four K_T bins. This thesis will present results for both one-dimensional and three-dimensional femtoscopic analyses, the latter being the first of its kind for the $K^0_S K^0_S$ system.

To my parents and grandparents.

Acknowledgments

First, I would like to thank my advisor, Tom Humanic, for his support, guidance, and patience over the past five years. I would also like to thank Mike Lisa for his additional support and guidance. I would like to thank Tom and Mike both for accepting me into their research group, for encouraging and critiquing my work when necessary, and for providing me with the opportunities and means to travel to CERN and to various conferences. I also thank the rest of the OSU Nuclear Physics group for their collaboration and the professors at The Ohio State University and the University of Wisconsin-Madison for their tutelage.

Next, I would like to thank my fellow researchers in the heavy-ion community, especially the ALICE collaboration and the ALICE femtoscopy group. I would especially like to thank Dhevan Gangadharan for helping me kickstart my analysis, providing daily guidance on all things experimental, theoretical, and computational, and accompanying me on our global travels.

I would like to acknowledge financial support from the U.S. National Science Foundation under grant PHY-1307188 and computing support from the Ohio Supercomputer Center.

Lastly, I would like to give special thanks to my friends and family. To my friends: thank you for your love, support, joviality, and shared interest in music, food, sports, and trivia contests, which have been extremely crucial to my sanity and enjoyment of life over the past six years. To my family: thank you for your undying love, support, and provision over the past thirty years. I could not have succeeded without you.

Vita

September 5, 1984	Born, Plymouth, Wisconsin
June 2003	Diploma, Plymouth High School, Plymouth, Wisconsin
August 2008	B.S., University of Wisconsin-Madison, Madison, Wisconsin
September 2008 - May 2010	Graduate Teaching Assistant, The Ohio State University, Columbus, Ohio
December 2010	M.S., Physics, The Ohio State University, Columbus, Ohio
September 2010 - present	Graduate Research Assistant, The Ohio State University, Columbus, Ohio

Publications

Abelev, B. *et al.* [ALICE Collaboration] "Performance of the ALICE experiment at the CERN LHC". *Int. J. Mod. Phys A*, 29(24):1430044, Sep. 2014.

Abelev, B. *et al.* [ALICE Collaboration] "Production of charged pions, kaons and protons at large transverse momenta in pp and Pb-Pb collisions at $\sqrt{s_{\rm NN}} = 2.76$ TeV". *Phys. Lett. B*, 736:196–207, Sep. 2014.

Abelev, B. *et al.* [ALICE Collaboration] "Measurement of quarkonium production at forward rapidity in pp collisions at $\sqrt{s} = 7$ TeV". *Eur. Phys. J. C*, 74(8):2974, Aug. 2014.

Abelev, B. *et al.* [ALICE Collaboration] "Upgrade of the ALICE Experiment Letter Of Intent". *J. Phys. G: Nucl. Part. Phys.*, 41(8):087001, Aug. 2014.

Abelev, B. *et al.* [ALICE Collaboration] "Technical Design Report for the Upgrade of the ALICE Inner Tracking System". *J. Phys. G: Nucl. Part. Phys.*, 41(8):087002, Aug. 2014.

Abelev, B. *et al.* [ALICE Collaboration] "Centrality, rapidity and transverse momentum dependence of J/ψ suppression in Pb-Pb collisions at $\sqrt{s_{\rm NN}} = 2.76$ TeV". *Phys. Lett. B*, 734:314-327, Jun. 2014.

Abelev, B. *et al.* [ALICE Collaboration] "Measurement of charged jet suppression in Pb-Pb collisions at $\sqrt{s_{\rm NN}} = 2.76$ TeV". *J. High Energy Phys.*, 3:013, Mar. 2014.

Abelev, B. *et al.* [ALICE Collaboration] "Two- and three-pion quantum statistics correlations in Pb-Pb collisions at $\sqrt{s_{\rm NN}} = 2.76$ TeV at the CERN Large Hadron Collider". *Phys. Rev. C*, 89(2):024911, Feb. 2014.

Abelev, B. *et al.* [ALICE Collaboration] "J/ψ production and nuclear effects in p-Pb collisions at $\sqrt{s_{\rm NN}} = 5.02$ TeV". *J. High Energy Phys*, 2:073, Feb. 2014.

Abelev, B. *et al.* [ALICE Collaboration] "Multiplicity dependence of pion, kaon, proton and lambda production in p-Pb collisions at $\sqrt{s_{\rm NN}} = 5.02$ TeV". *Phys. Lett. B*, 728:25-38, Jan. 2014.

Abelev, B. *et al.* [ALICE Collaboration] "Multi-strange baryon production at mid-rapidity in Pb-Pb collisions at $\sqrt{s_{\rm NN}} = 2.76$ TeV". *Phys. Lett. B*, 728:216-227, Jan. 2014.

Abelev, B. *et al.* [ALICE Collaboration] "Multiplicity dependence of the average transverse momentum in pp, p-Pb, and Pb-Pb collisions at the LHC". *Phys. Lett. B*, 727:371-380, Dec. 2013.

Abelev, B. *et al.* [ALICE Collaboration] "Energy dependence of the transverse momentum distributions of charged particles in pp collisions measured by ALICE". *Eur. Phys. J. C*, 73(12):2662, Dec. 2013.

Abelev, B. *et al.* [ALICE Collaboration] "Directed Flow of Charged Particles at Midrapidity Relative to the Spectator Plane in Pb-Pb Collisions at $\sqrt{s_{\rm NN}} = 2.76$ TeV". *Phys. Rev. Lett.*, 111(23):232302, Dec. 2013.

Abelev, B. *et al.* [ALICE Collaboration] "$K^0_{\rm S}$ and Λ Production in Pb-Pb Collisions at $\sqrt{s_{\rm NN}} = 2.76$ TeV". *Phys. Rev. Lett.*, 111(22):222301, Nov. 2013.

Abbas, E. *et al.* [ALICE Collaboration] "Charmonium and e^+e^- pair photoproduction at mid-rapidity in ultra-peripheral Pb-Pb collisions at $\sqrt{s_{\rm NN}} = 2.76$ TeV". *Eur. Phys. J. C*, 73(11):2617, Nov. 2013.

Abbas, E. *et al.* [ALICE Collaboration] "Centrality dependence of the pseudorapidity density distribution for charged particles in Pb-Pb collisions at $\sqrt{s_{\rm NN}} = 2.76$ TeV". *Phys. Lett. B*, 726(4-5):610-622, Nov. 2013.

Abbas, E. *et al.* [ALICE Collaboration] "J/ψ Elliptic Flow in Pb-Pb Collisions at $\sqrt{s_{\rm NN}} = 2.76$ TeV". *Phys. Rev. Lett.*, 111(16):162301, Oct. 2013.

Abelev, B. *et al.* [ALICE Collaboration] "Centrality determination of Pb-Pb collisions at $\sqrt{s_{\rm NN}} = 2.76$ TeV". *Phys. Rev. C*, 88(4):044909, Oct. 2013.

Abelev, B. *et al.* [ALICE Collaboration] "Centrality dependence of π, K, and p production in Pb-Pb collisions at $\sqrt{s_{\rm NN}} = 2.76$ TeV". *Phys. Rev. C*, 88(4):044910, Oct. 2013.

Abelev, B. *et al.* [ALICE Collaboration] "Long-range angular correlations of π, K and p in p-Pb collisions at $\sqrt{s_{\rm NN}} = 5.02$ TeV". *Phys. Lett. B*, 726(1-3):164-177, Oct. 2013.

Abelev, B. *et al.* [ALICE Collaboration] "Multiplicity dependence of two-particle azimuthal correlations in pp collisions at the LHC". *J. High Energy Phys.*, 9:049, Sep. 2013.

Abelev, B. *et al.* [ALICE Collaboration] "D Meson Elliptic Flow in Noncentral Pb-Pb Collisions at $\sqrt{s_{\rm NN}} = 2.76$ TeV". *Phys. Rev. Lett.*, 111(10):102301, Sep. 2013.

Abbas, E. *et al.* [ALICE Collaboration] "Mid-rapidity anti-baryon to baryon ratios in pp collisions at $\sqrt{s} = 0.9$, 2.76, and 7 TeV". *Eur. Phys. J. C*, 73(7):2496, Jul. 2013.

Abelev, B. *et al.* [ALICE Collaboration] "Charge correlations using the balance function in Pb-Pb collisions at $\sqrt{s_{\rm NN}} = 2.76$ TeV". *Phys. Lett. B*, 723(4-5):267-279, Jun. 2013.

Abelev, B. *et al.* [ALICE Collaboration] "Measurement of inelastic, single- and double-diffraction cross sections in proton-proton collisions at the LHC with ALICE". *Eur. Phys. J. C*, 73(6):2456, Jun. 2013.

Abelev, B. *et al.* [ALICE Collaboration] "Measurement of the inclusive differential jet cross section in pp collisions at $\sqrt{s} = 2.76$ TeV". *Phys. Lett. B*, 722(4-5):262-272, May 2013.

Abelev, B. *et al.* [ALICE Collaboration] "Net-Charge Fluctuations in Pb-Pb Collisions at $\sqrt{s_{\rm NN}} = 2.76$ TeV". *Phys. Rev. Lett.*, 110(15):152301, Apr. 2013.

Abelev, B. *et al.* [ALICE Collaboration] "Measurement of electrons from beauty hadron decays in pp collisions at $\sqrt{s} = 7$ TeV". *Phys. Lett. B*, 721(1-3):13-23, Apr. 2013.

Abelev, B. *et al.* [ALICE Collaboration] "Charged kaon femtoscopic correlations in pp collisions at $\sqrt{s} = 7$ TeV". *Phys. Rev. D*, 87(5):052016, Mar. 2013.

Abelev, B. *et al.* [ALICE Collaboration] "Centrality dependence of charged particle production at large transverse momentum in Pb-Pb collisions at $\sqrt{s_{\rm NN}} = 2.76$ TeV". *Phys. Lett. B*, 720(1-3):52-62, Mar. 2013.

Abelev, B. *et al.* [ALICE Collaboration] "Transverse Momentum Distribution and Nuclear Modification Factor of Charged Particles in p-Pb Collisions at $\sqrt{s_{\rm NN}} = 5.02$ TeV". *Phys. Rev. Lett.*, 110(8):082302, Feb. 2013.

Abelev, B. *et al.* [ALICE Collaboration] "Anisotropic flow of charged hadrons, pions and (anti-)protons measured at high transverse momentum in Pb-Pb collisions at $\sqrt{s_{\rm NN}} = 2.76$ TeV". *Phys. Lett. B*, 719(1-3):18-28, Feb. 2013.

Abelev, B. *et al.* [ALICE Collaboration] "Long-range angular correlations on the near and away side in p-Pb collisions at $\sqrt{s_{\rm NN}} = 5.02$ TeV". *Phys. Lett. B*, 719(1-3):29-41, Feb. 2013.

Abelev, B. *et al.* [ALICE Collaboration] "Coherent J/ψ photoproduction in ultra-peripheral Pb-Pb collisions at $\sqrt{s_{\rm NN}} = 2.76$ TeV". *Phys. Lett. B*, 718(4-5):1273-1283, Jan. 2013.

Abelev, B. *et al.* [ALICE Collaboration] "Pseudorapidity Density of Charged Particles in p-Pb Collisions at $\sqrt{s_{\rm NN}} = 5.02$ TeV". *Phys. Rev. Lett.*, 110(3):032301, Jan. 2013.

Abelev, B. *et al.* [ALICE Collaboration] "Charge separation relative to the reaction plane in Pb-Pb collisions at $\sqrt{s_{\rm NN}} = 2.76$ TeV". *Phys. Rev. Lett.*, 110(1):012301, Jan. 2013.

Abelev, B. *et al.* [ALICE Collaboration] "Measurement of electrons from semileptonic heavy-flavor hadron decays in pp collisions at $\sqrt{s} = 7$ TeV". *Phys. Rev. D*, 86(11):112007, Dec. 2012.

Abelev, B. *et al.* [ALICE Collaboration] "Measurement of the Cross Section for Electromagnetic Dissociation with Neutron Emission in Pb-Pb Collisions at $\sqrt{s_{\rm NN}} = 2.76$ TeV". *Phys. Rev. Lett.*, 109(25):252302, Dec. 2012.

Abelev, B. *et al.* [ALICE Collaboration] "Pion, Kaon, and Proton Production in Central Pb-Pb Collisions at $\sqrt{s_{\rm NN}} = 2.76$ TeV". *Phys. Rev. Lett.*, 109(25):252301, Dec. 2012.

Abelev, B. *et al.* [ALICE Collaboration] "$\rm D_s^+$ meson production at central rapidity in proton-proton collisions at $\sqrt{s} = 7$ TeV". *Phys. Lett. B*, 718(2):279-294, Dec. 2012.

Abelev, B. *et al.* [ALICE Collaboration] "Inclusive J/ψ production in pp collisions at $\sqrt{s} = 2.76$ TeV". *Phys. Lett. B*, 718(2):295-306, Dec. 2012.

Abelev, B. *et al.* [ALICE Collaboration] "Measurement of prompt J/ψ and beauty hadron production cross sections at mid-rapidity in pp collisions at $\sqrt{s} = 7$ TeV". *J. High Energy Phys.*, 11:065, Nov. 2012.

Abelev, B. *et al.* [ALICE Collaboration] "$K^0_{\rm S} - K^0_{\rm S}$ correlations in pp collisions at $\sqrt{s} = 7$ TeV from the LHC ALICE experiment". *Phys. Lett. B*, 717(1-3):151-161, Oct. 2012.

Abelev, B. *et al.* [ALICE Collaboration] "Neutral pion and eta meson production in proton-proton collisions at $\sqrt{s} = 0.9$ TeV and $\sqrt{s} = 7$ TeV". *Phys. Lett. B*, 717(1-3):162-172, Oct. 2012.

Abelev, B. *et al.* [ALICE Collaboration] "Production of $K^*(892)^0$ and $\phi(1020)$ in pp collisions at $\sqrt{s} = 7$ TeV". *Eur. Phys. J. C*, 72(10):2183, Oct. 2012.

Abelev, B. *et al.* [ALICE Collaboration] "Production of Muons from Heavy Flavor Decays at Forward Rapidity in pp and Pb-Pb Collisions at $\sqrt{s_{\rm NN}} = 2.76$ TeV". *Phys. Rev. Lett.*, 109(11):112301, Sep. 2012.

Abelev, B. *et al.* [ALICE Collaboration] "Suppression of high transverse momentum D mesons in central Pb-Pb collisions at $\sqrt{s_{\rm NN}} = 2.76$ TeV". *J. High Energy Phys.*, 9:112, Sep. 2012.

Abelev, B. *et al.* [ALICE Collaboration] "Transverse sphericity of primary charged particles in minimum bias proton-proton collisions at $\sqrt{s} = 0.9$, 2.76 and 7 TeV". *Eur. Phys. J. C*, 72(9):2124, Sep. 2012.

Abelev, B. *et al.* [ALICE Collaboration] "J/ψ Suppression at Forward Rapidity in Pb-Pb Collisions at $\sqrt{s_{\rm NN}} = 2.76$ TeV". *Phys. Rev. Lett.*, 109(7):072301, Aug. 2012.

Abelev, B. *et al.* [ALICE Collaboration] "Underlying Event measurements in pp collisions at $\sqrt{s} = 0.9$ and 7 TeV with the ALICE experiment at the LHC". *J. High Energy Phys.*, 7:116, Jul. 2012.

Abelev, B. *et al.* [ALICE Collaboration] "Multi-strange baryon production in pp collisions at $\sqrt{s} = 7$ TeV with ALICE". *Phys. Lett. B*, 712(4-5):309-318, Jun. 2012.

Abelev, B. *et al.* [ALICE Collaboration] "J/ψ production as a function of charged particle multiplicity in pp collisions at $\sqrt{s} = 7$ TeV". *Phys. Lett. B*, 712(3):165-175, Jun. 2012.

Abelev, B. *et al.* [ALICE Collaboration] "Light vector meson production in pp collisions at $\sqrt{s} = 7$ TeV ALICE Collaboration". *Phys. Lett. B*, 710(4-5):557-568, Apr. 2012.

Abelev, B. *et al.* [ALICE Collaboration] "Measurement of event background fluctuations for charged particle jet reconstruction in Pb-Pb collisions at $\sqrt{s_{\rm NN}} = 2.76$ TeV". *J. High Energy Phys.*, 3:053, Mar. 2012.

Aamodt, K. *et al.* [ALICE Collaboration] "Particle-Yield Modification in Jetlike Azimuthal Dihadron Correlations in Pb-Pb Collisions at $\sqrt{s_{\rm NN}} = 2.76$ TeV". *Phys. Rev. Lett.*, 108(9):092301, Mar. 2012.

Aamodt, K. *et al.* [ALICE Collaboration] "Harmonic decomposition of two particle angular correlations in Pb-Pb collisions at $\sqrt{s_{\rm NN}} = 2.76$ TeV". *Phys. Lett. B*, 708(3-5):249-264, Feb. 2012.

Abelev, B. *et al.* [ALICE Collaboration] "Heavy flavour decay muon production at forward rapidity in proton-proton collisions at $\sqrt{s} = 7$ TeV". *Phys. Lett. B*, 708(3-5):265-275, Feb. 2012.

Abelev, B. *et al.* [ALICE Collaboration] "J/ψ Polarization in pp Collisions at $\sqrt{s} = 7$ TeV". *Phys. Rev. Lett.*, 108(8):082001, Feb. 2012.

Abelev, B. *et al.* [ALICE Collaboration] "Measurement of charm production at central rapidity in proton-proton collisions at $\sqrt{s} = 7$ TeV". *J. High Energy Phys.*, 1:128, Jan. 2012.

Aamodt, K. *et al.* [ALICE Collaboration] "Rapidity and transverse momentum dependence of inclusive J/ψ production in pp collisions at $\sqrt{s} = 7$ TeV". *Phys. Lett. B*, 704(5):442-455, Oct. 2011.

Aamodt, K. *et al.* [ALICE Collaboration] "Higher Harmonic Anisotropic Flow Measurements of Charged Particles in Pb-Pb Collisions at $\sqrt{s_{\rm NN}} = 2.76$ TeV". *Phys. Rev. Lett.*, 107(3):032301, Jul. 2011.

Aamodt, K. *et al.* [ALICE Collaboration] "Elliptic Flow of Charged Particles in Pb-Pb Collisions at $\sqrt{s_{\rm NN}} = 2.76$ TeV". *Phys. Rev. Lett.*, 105(25):252302, Dec. 2010.

Aamodt, K. *et al.* [ALICE Collaboration] "Charged-Particle Multiplicity Density at Midrapidity in Central Pb-Pb Collisions at $\sqrt{s_{\rm NN}} = 2.76$ TeV". *Phys. Rev. Lett.*, 105(25):252301, Dec. 2010.

Fields of Study

Major Field: Physics

Studies in Experimental Relativistic Heavy-Ion Collisions: Professor Thomas Humanic

Table of Contents

List of Figures

Figure **Page**

List of Tables

Chapter 1
Introduction

The field of ultra-relativistic heavy-ion collisions has been extremely influential in expanding the scientific community's collective knowledge of the strong interaction. Over the past several decades, high-energy nuclear collisions have been used to search for the Quark-Gluon Plasma (QGP), a new[1] state of matter which consists of deconfined quarks and gluons and exists only at very high temperatures and energy densities. Once the QGP was discovered, high-energy nuclear physicists continued to study these collisions in order to learn more about the characteristics of the QGP and the strong interaction in general, giving the physics world an experimental helping hand to better understand this fundamental force whose effects are notoriously difficult to calculate theoretically. During the past several years, the Large Hadron Collider (LHC) at the European Organization for Nuclear Research (CERN) has instituted a high-energy heavy-ion collision program, and the dedicated heavy-ion collaboration ALICE (A Large Ion Collider Experiment) has performed analyses and published results on all aspects of the exciting physics involved in these collisions.

Femtoscopy is one of the experimental tools used by physicists to study high-energy heavy-ion collisions. It is an interferometric analysis that connects the experimentally measureable final-state momentum of particles to the experimentally *un*measureable geometry of the particle-emitting sources and infers information about the dynamics of the hot, dense matter that exists between the initial collision and the subsequent dissolution of the sys-

[1] Before high-energy collision experiments, the QGP had probably already been formed on Earth during collisions of highly-energetic cosmic rays with our atmosphere. Besides these terrestrial occurrences, the QGP likely existed during the early stages of the evolution of the universe after the Big Bang and also possibly exists in the cores of high-density neutron stars.

tem. Femtoscopic analyses have been performed for many different particle types at several different collision energies, and studying all of these analyses together has helped physicists to better understand the interactions of particles during and after the QGP phase. The neutral kaon K^0_S is a particle species that has not been extensively studied by the community even though its femtoscopic correlation presents an excellent complement to the more commonly studied pion and charged kaon analyses.

In this thesis, we will present $K^0_S K^0_S$ femtoscopic correlations in Pb-Pb collisions at $\sqrt{s_{NN}} = 2.76$ TeV at the LHC with ALICE. This analysis will be the first centrality- and K_T-differential study of $K^0_S K^0_S$ correlations in heavy-ion collisions. This will also be the first three-dimensional K^0_S femtoscopic analysis. The thesis is organized as follows: Chapter 2 will discuss the strong interaction, the Quark-Gluon Plasma, and heavy-ion collisions; Chapter 3 will describe the experimental setup of the LHC accelerator and the ALICE detector; Chapter 4 will detail the theoretical formalism of femtoscopy and discuss the collision characteristics we can study using femtoscopic analyses; Chapter 5 will describe the various neutral kaon states and the combined two-kaon states and will derive the $K^0_S K^0_S$ femtoscopic correlation; Chapter 6 will explain many of the experimental details used to complete the work of this thesis; Chapter 7 will present the results from this analysis; and Chapter 8 will summarize this thesis.

Chapter 2

Ultra-relativistic Heavy-Ion Collisions and the Quark-Gluon Plasma

Ultra-relativistic heavy-ion collisions are the primary tool for physicists to study the workings of the *strong interaction*, or *strong nuclear force*, which is one of the fundamental forces which make up the Standard Model, the prevailing theory which describes the interactions of particle physics. The constituents of the strong force are *quarks*, which are subatomic particles that combine to form hadrons, and *gluons*, which are the massless bosons exchanged by quarks interacting via the strong force. In this chapter, we will briefly discuss ultra-relativistic heavy-ion collisions and then look at Quantum Chromodynamics, the theory that governs the dynamics of the strong interaction, as well as one of its most important predictions, the Quark-Gluon Plasma (QGP). We will study the various signatures of the QGP and look at some of the related results from ALICE.

2.1 Ultra-relativistic heavy-ion collisions

In ultra-relativistic heavy-ion collisions at the LHC, Pb^{208}_{82} nuclei collide with a center-of-mass energy per nucleon-nucleon pair of$\sqrt{s_{\mathrm{NN}}} = 2.76$ TeV. At these energies, the de Broglie wavelength ($\lambda = h/p$) of the nucleons is much smaller than the size of the nucleus. Also, the nucleon-nucleon interaction range is only ~ 1 fm. Thus, the nucleus-nucleus collision should really be understood as a combination of individual nucleon-nucleon collisions. In

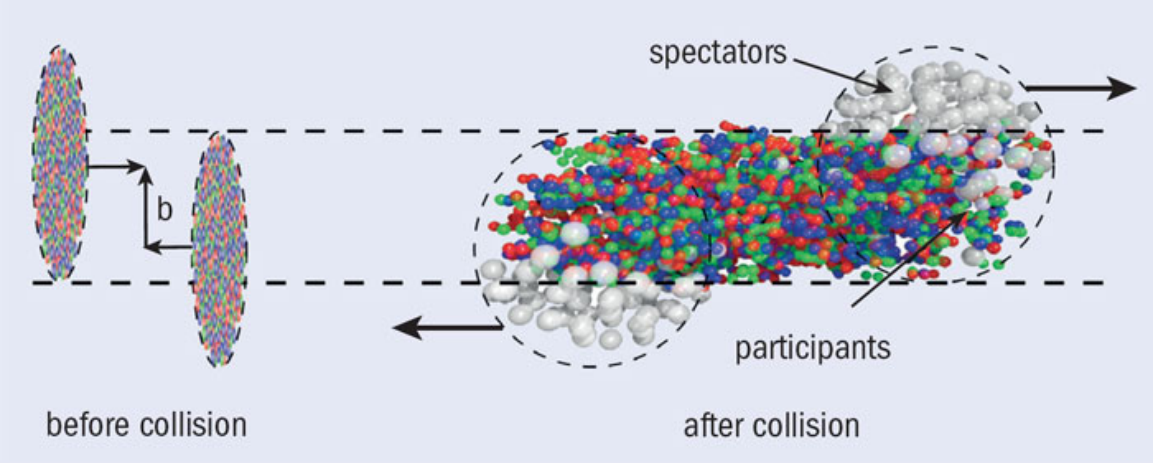

Figure 2.1: A representation of colliding nuclei in a high energy heavy-ion collision. Note the Lorentz-contracted incoming nuclei, the impact parameter b, and the denotion of the participant and spectator nucleons (plot taken from [1]).

this picture, the geometry of the incoming nuclei becomes very important. Fig. 2.1 shows a representation of colliding nuclei. The incoming nuclei are drawn as thin "pancakes" in the lab frame due to their relativistic Lorentz contraction; at energies of $E \sim 1$ TeV, the nucleon's Lorentz gamma factor is $\gamma = E/m \sim 1000$, so $r_{z,\text{rel}} = r_{z,\text{non-rel}}/1000$. We define the *impact parameter* b as the distance between the centers of the nuclei. $b = 0$ refers to a *central collision* where the two nuclei fully overlap. As b increases, the collisions become more *peripheral*, until $b \gtrsim 2R_{nucleus}$ where the nuclei may "collide" only electromagnetically or simply pass by each other. Fig. 2.2 shows a diagram depicting collisions of different centralities.

Since we stated that the nucleus-nucleus collision is really a series of nucleon-nucleon collisions, we define two group of nucleons: *participants* are nucleons within the nucleus overlap region which undergo collisions, and *spectators* are those nucleons outside the overlap region which simply pass by without colliding. While the specators do not participate in the collision, they are often detected down the beam line and used to measure global event parameters such as the centrality (size of b) or event plane (direction of $\vec{b}$). Using this simple geometry, one can estimate the number of participant nucleons, N_{part}, as well as the number of "binary" nucleon-nucleon collisions, N_{coll}, using the Glauber model [2, 3]. Briefly, the

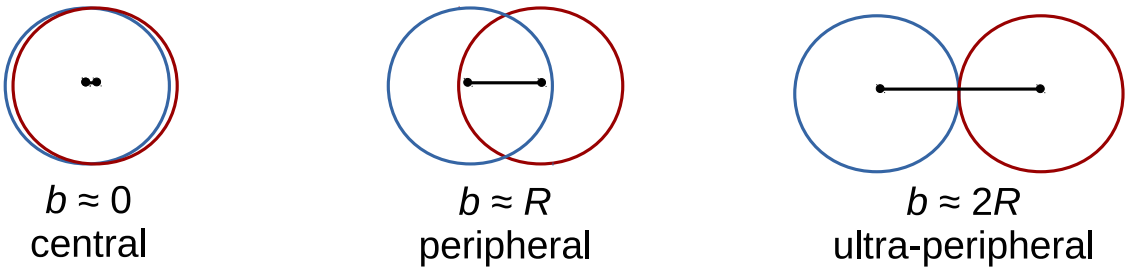

Figure 2.2: A representation of colliding nuclei at different centralities, shown in the plane transverse to the beam direction. The black line signifies the impact parameter b connecting the centers of the two nuclei.

Glauber model estimates the numbers of collisions and participants by distributing nucleons within a nucleus according to some assumed nuclear density profile and integrating over the geometries of the colliding nuclei (in both transverse and longitudinal directions), assuming some nucleon-nucleon inelastic cross section. Note that generally $N_{coll} \approx 2 - 3\ N_{part}$ because a nucleon can partipate in several collisions as it passes through the other nucleus. The Glauber model is extremely useful for setting up the initial geometric conditions (to first order) from which theoretical models can evolve the system to make predictions of final-state observables.

2.2 The strong interaction and Quantum Chromodynamics

As mentioned earlier, the strong interaction is the force that acts between quarks and gluons within the nuclei of matter. Quarks come in six *flavors*: **u**p, **d**own, **s**trange, **c**harm, **b**ottom, and **t**op (as well as the negative-flavor quarks, or "anti-"quarks). Quarks are electrically charged with fractional charges of $+2/3\,e$ (u,c,t) or $-1/3\,e$ (d,s,b); anti-quarks have opposite sign charges. Quarks also have another quantum number called *color*, which takes one of three values commonly known as red, blue, and green (as well as "anti-" colors). Gluons also have color, but they are bi-colored, while quarks carry only one color. This leads to the fact that quark-gluon interactions involve the changing of the quark color. Thus, the prevailing theory which describes the strong nuclear force interactions is known as Quantum

Chromodynamics[2], or QCD.

An interesting aspect of QCD is that since gluons carry color, they can interact with each other via the strong interaction. This is different than in Quantum Electrodynamics (QED), where the intermediary bosons, photons, do not carry electric charge and thus cannot interact with each other. Thus, the strong interactions have Feynman diagrams with gluon loops as well as quark loops (see Fig. 2.3). The quark loops lead to "charge screening", which makes the force weaker at large distances (similar to the electromagnetic force). However, the gluon loops lead to "charge *anti*-screening", which causes a stronger force at large distances. In QCD, the anti-screening actually dominates, and we see a coupling progression opposite to what we see in QED: strong interactions become weaker at short distances and stronger at large distances. The large and short distance regimes and their associated coupling values are known respectively as *confinement*, or *infrared slavery*, and *asymptotic freedom*. Fig. 2.4 shows a qualitative representation of the opposite trends of the QED and QCD coupling parameters. In the large momentum-transfer region, the weak coupling allows one to use perturbative methods to study QCD [4]; an example is the study of hard-scattered partons and the production of high-energy particles. However, perturbation theory cannot be used in the low-Q^2 regions where the coupling becomes stronger. This complicates any attempts of calculating production processes for the bulk of the matter produced in heavy-ion collisions.

The result of confinement is that in the low momentum-transfer regime $|Q| \lesssim 1$ GeV/c, quarks are confined together in color-neutral[3] groupings known as *hadrons*. Hadrons can be three-quark systems known as *baryons* or quark–anti-quark systems known as *mesons*. The property of confinement causes the interaction strength to increase as quarks are pulled apart from each other. In fact, at a certain critical interaction strength, it becomes more energetically favorable for an extra quark–anti-quark pair to be produced from the stored energy; these new quarks combine with the original quarks to form new hadrons. Hence, in experiments, we can only detect hadrons and never lone quarks.

[2] *Chromos* is the Greek word for "color".

[3] Color neutrality can consist of red+green+blue or anti-red+anti-green+anti-blue (baryons) or color+anti-color (mesons).

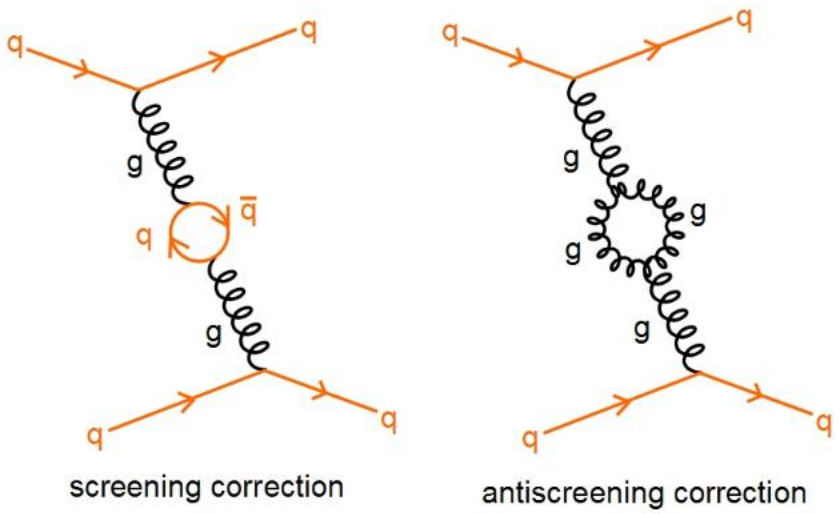

Figure 2.3: Examples of the one-loop Feynman diagrams showing quark and gluon loops which lead to color screening and anti-screening, respectively. Plot taken from http://cronodon.com/Atomic/QCD.html.

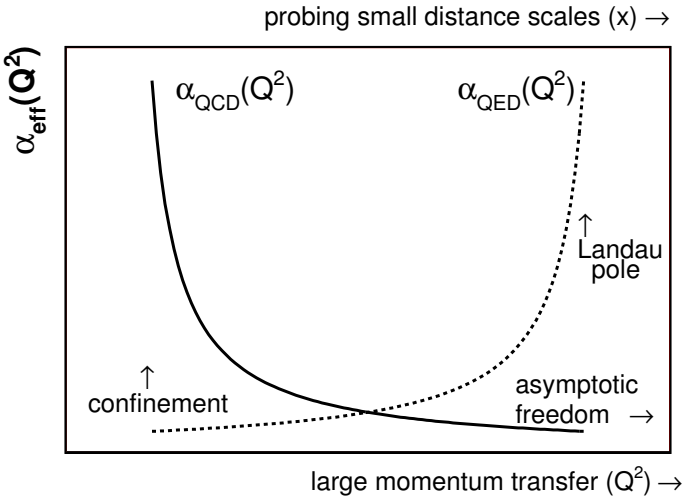

Figure 2.4: Qualitative diagram of the running coupling parameters for QCD and QED, showing the opposite trends exhibited by the two forces [5].

2.3 Quark-Gluon Plasma

The result of the running of the strong coupling constant and the concept of asymptotic freedom is that the interaction strength of the strong force drops in the region of high momentum transfer, or at very small distances. Thus, it was hypothesized that at very high energy density, the color force acting between quarks and gluons should become weak enough that this matter would be a weakly interacting gas. Instead of the usual case of quark confinement, there would be a new state of matter consisting of *deconfined* quarks and gluons. This state has been given the name Quark-Gluon Plasma[4] (QGP) due to the analogous relation to the electromagnetic plasma of dissociated ions and electrons. This novel state of matter has been found in the high-energy heavy-ion collisions at RHIC [7–10] and the LHC, and many physicists were surprised to find that the deconfined quarks and gluons did not act as a weakly interacting gas but as a strongly-coupled hydrodynamic system, behaving like a near-perfect liquid with extremely low viscosity [11].

After this hypothesis was proposed, subsequent questions arose about the transition from confined hadrons to a deconfined QGP. For example, is it a smooth transition or a canonical phase transition marked by critical (discontinuous) behavior of some parameter? At what energy or temperature does this transition happen? Lattice QCD, the computational technique used to study the complicated dynamical equations of the strong interaction, suggests that the critical temperature for the deconfinement of partons is around $T_c \approx 155 - 175$ MeV, which corresponds to a critical energy density of $\epsilon_c \sim 1$ GeV fm^{-3} [12]. Determining the type of phase transition is a bit tricky, as lattice results are very sensitive to the choice of the parameters used, such as quark masses and chemical potentials. Fig 2.5 shows the possible types of phase transitions predicted by lattice calculations for different values of the quark masses.

Another interesting aspect about the QGP is that there is another venue for this hot, dense state of matter outside of high-energy collisions: the early universe. In the evolution of the early universe according to Big Bang cosmology, the universe expanded from a sin-

[4]First coined by Shuryak in the late 1970s [6].

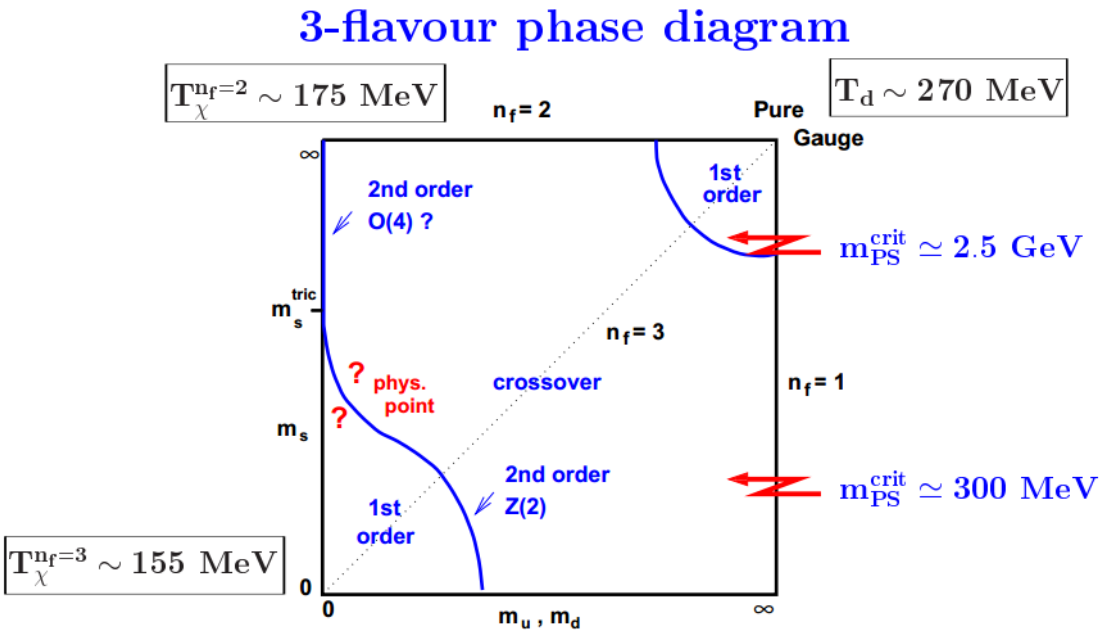

Figure 2.5: The QCD phase diagram of 3-flavor lattice QCD for various u/d (degenerate) and s quark masses [13].

gularity at time zero. After $\sim 10^{-5}$ s, the temperature of the universe had cooled to about ~ 100 MeV [12]. Shortly before this, the state of matter of the whole universe was likely a quark-gluon plasma similar to those created in the lab today. Thus, the heavy-ion studies at RHIC and the LHC help give us insight into the physics of the early universe.

2.4 Evolution of a heavy-ion collision

The key stages of a heavy-ion collision consist of pre-equilibrium, thermalization, expansion, and decoupling. We will take a brief look at each of these stages now.

Nucleons are often described by their *constituent*, or *valence*, quark content, e.g. $p = [u, u, d]$ and $n = [u, d, d]$. However, at the high energies of heavy-ion collisions, a nucleon actually contains many partons of various types. Fig. 2.7 shows the parton distribution function as a function of x, defined as the longitudinal momentum fraction carried by the parton, $x = p_z/\sqrt{s_{\mathrm{NN}}}$. This plot shows the effective multiplicity of each specific type of parton with a certain x. The collisions of high-energy nucleons generally

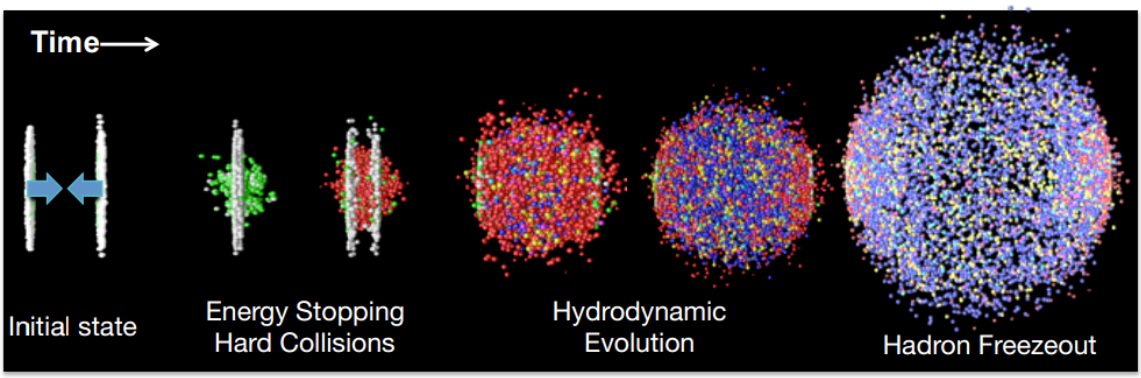

Figure 2.6: Evolution of a heavy-ion collision (plot taken from [14]).

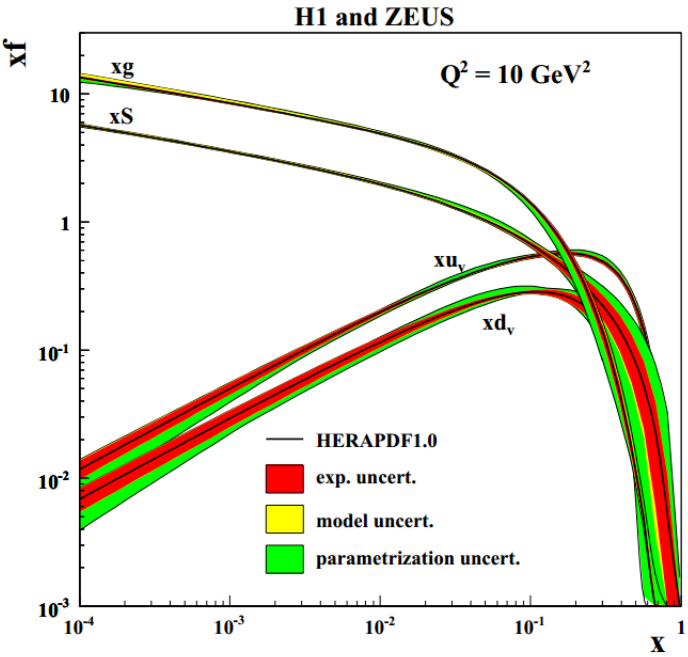

Figure 2.7: Parton distribution function as a function of longitudinal momentum fraction x (plot taken from [15]).

probe the low-x part of the distribution, and from Fig 2.7, we can see that in this dynamical region, the number of gluons dominates over the number of quarks. The quark content itself is actually dominated by the *sea quarks*, which are $q\bar{q}$ vacuum fluctuations coming from gluon splitting, while the valence quarks are a negligible factor. The large number of partons present in high-energy nucleons complicates the calculations necessary for theoretical models aiming to describe these collisions.

As the nuclei pass through each other, the colliding nucleons deposit their energy into the space between the outgoing nuclei, producing the bulk partonic matter which will later thermalize into the QGP. As stated earlier, these production processes cannot be calculated perturbatively and require phenomenological models to describe them. Exactly how the quarks and gluons of the bulk matter are created or "liberated" is not completely understood; see discussions of color strings [16] and Color Glass Condensate [17] for more details. The time shortly after the partons are created and before they have interacted enough to become thermalized is known as the *pre-equilibrium* stage. The dynamics of the partons in this stage can be described using various transport theories, such as the relativistic Boltzmann equation and quantum transport theory [18,19]. These microscopic transport theories attempt to explain the thermalization process of the partonic matter.

Another important aspect of the very early moments of the collision are hard parton-parton collisions that can hard-scatter partons with large momentum transfer. As stated earlier, the hard-scattered parton will create $q\bar{q}$ pairs which can combine with other partons to form particles with large momentum and/or large mass. Photons can also be produced by the interactions of the sea of quarks and anti-quarks present among the colliding nucleons. These particles produced early in the collision can be used as *hard probes* of the bulk matter which is produced shortly afterward; such probes and their uses are discussed in the next section.

The secondary partonic collisions that occur after the nuclei collide lead to a equipartioning of the deposited energy, and the matter develops into a locally thermalized system. In this stage, we can switch from microscopic transport theories to relativistic hydrodynamics to describe the system. Evidence [7,8] shows that the QGP behaves as a near-perfect liquid

with viscosity per entropy density near the quantum lower limit [20]. The thermalized system will expand according to the laws of hydrodynamics due to the pressure gradients that exist between the hot, dense system and the vacuum outside. This hydrodynamic behavior produces *collective flow*, in which the particles are boosted together radially outward from the system.

As the system expands, the temperature and energy density will decrease until the system reaches the critical values at which the partons will transition from a QGP to a deconfined hadronic system. The partons combine into hadronic bound states, either three-quark baryons or two-quark mesons. This occurs around the predicted critical values of $\epsilon_{\text{crit}} \sim 1$ GeV/fm^3 and $T_{\text{crit}} \approx 155 - 175$ MeV. After hadronization, the system is still dense enough that the hadrons can participate in elastic and inelastic rescatterings with each other. Also, many of the initial hadronic bound states created during hadronization will decay into more stable decay products.

Eventually, after resonances have decayed and the collisions are no longer energetic enough to be inelastic, the multiplicities of each hadronic species will become fixed; this is known as *chemical freeze-out*. Chemical freeze-out seems to happen shortly after hadronization; statistical thermal model comparisons with data have extracted temperatures of $T_{\text{chem}} \approx 150 - 160$ MeV [21]. Also, the chemical freeze-out is likely species-dependent, as light-quark and strange-quark hadrons seem to exhibit different chemical freeze-out temperatures [22]. The hadrons continue to rescatter elastically until the system is too dilute for any interactions to occur; this is known as *kinetic freeze-out*. Again, it is very likely that different particle species freeze-out kinetically at different times. Experimental results extract kinetic freeze-out temperatures of $T_{\text{kin}} \approx 100 - 150$ MeV [23], depending on the event centrality, since dense central collisions take longer (i.e. lower temperature) to freeze-out than more dilute peripheral collisions. After kinetic freeze-out, the particles will stream freely away from the collision site and enter the detector, where their momentum will be measured at the same value as when they "froze-out".

2.5 Signatures of the QGP

Since the QGP that exists inside heavy-ion collisions only lasts for ~ 10 fm/c, or $\sim 10^{-23}$ s, we cannot directly observe it in the laboratory. Instead, there are several signatures of the QGP that can be observed in the detection and analysis of the final-stage particles that are actually measured. The following subsections will list several of these signatures and will briefly discuss the results found by ALICE.

Direct photons: Temperature

As stated above, the critical energy density and temperature when deconfinement occurs are calculated to be $\epsilon_{\text{crit}} \sim 1$ GeV fm^{-3} and $T_{\text{crit}} \approx 155 - 175$ MeV. One way to estimate the temperature of the QGP is by the measurement of direct photons. Direct photons in pp collisions come from quark-gluon Compton scattering, quark–anti-quark annihilation, and jet fragmentation; if a QGP is formed, an additional photon signal is expected to come from the scattering of the thermalized partons [24–26]. Fig. 2.8 shows the ALICE results for direct photon measurement [27]. One can see the excess at low p_{T} of measured photon production in Pb-Pb collisions compared to calculations from scaled pp collisions, suggesting the existence of a thermalized medium.

One can then fit the low-p_{T} part of this distribution with a simple exponential $\frac{dN}{p_{\text{T}}dp_{\text{T}}} \sim e^{-p_{\text{T}}/T}$ to extract the temperature of the thermalized system which emitted the photons. ALICE extracted a temperature $T = 304 \pm 51$ MeV, concluding that the system was above the predicted QGP critical temperature and thus in the QGP phase. One should note here that recent research suggests that this temperature alone is not conclusive evidence of the presence of QGP, as this is only an "effective temperature" that can be significantly enhanced above the true temperature due to the presence of strong radial flow [28].

Charged-particle multiplicity: Energy density

In heavy-ion collisions, the charged-particle multiplicity (or pseudorapidity density) $dN_{\text{ch}}/d\eta$ can be related to the initial energy density of the system via a relation derived by

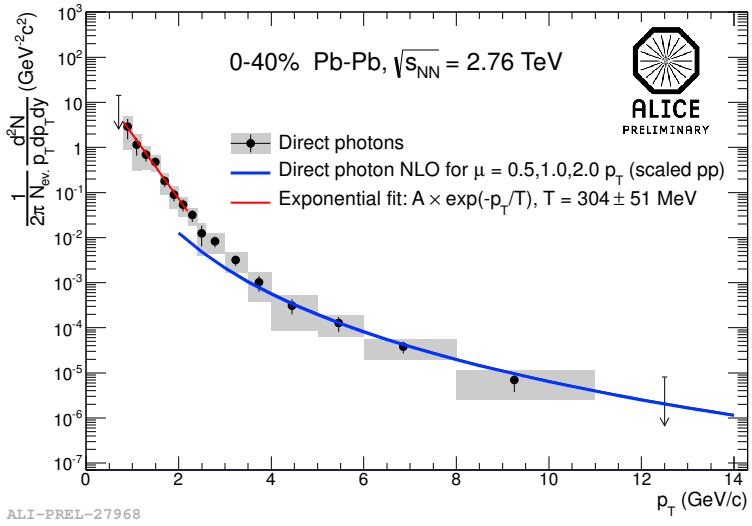

Figure 2.8: Direct photon invariant yield measured by ALICE in Pb-Pb collisions at $\sqrt{s_{\rm NN}} = 2.76$ TeV for 0-40% centrality. Note the excess of photons at low $p_{\rm T}$ over the NLO predictions from scaled pp collisions, suggesting a thermalized medium, i.e. QGP. The low-$p_{\rm T}$ distribution is fit with an exponential to extract an effective temperature.

Bjorken [29]. ALICE measured the density of primary charged particles at mid-rapidity in 0-5% central collisions to be $dN_{\rm ch}/d\eta \approx 1600$ [30]. This corresponds to an initial energy density of ~ 15 GeV fm^{-3} [5], which is well above the predicted QGP critical energy density of ~ 1 GeV fm^{-3}.

High-$p_{\rm T}$ suppression

High-energy partons that are scattered from a nucleon-nucleon collision will lose energy as they traverse the QGP medium [32]. There are several types of energy loss that will affect the partons: vacuum energy loss (i.e. color flux tubes due to confinement), collisional energy loss from multiple elastic collisions with thermal particles, and gluon radiation [12]. The vacuum energy loss, as its name suggests, is not specific to a QGP medium; however, the collisional and radiative energy losses are medium-induced effects which suggest the presence of a QGP. We can check for this additional energy loss by comparing the data from heavy-ion collisions to that from pp collisions, where we do not expect a QGP to have

[5] This number is quoted in many places and is generally attributed to [31], but the reference itself does not directly calculate this number, and no explicit calculation could be found elsewhere.

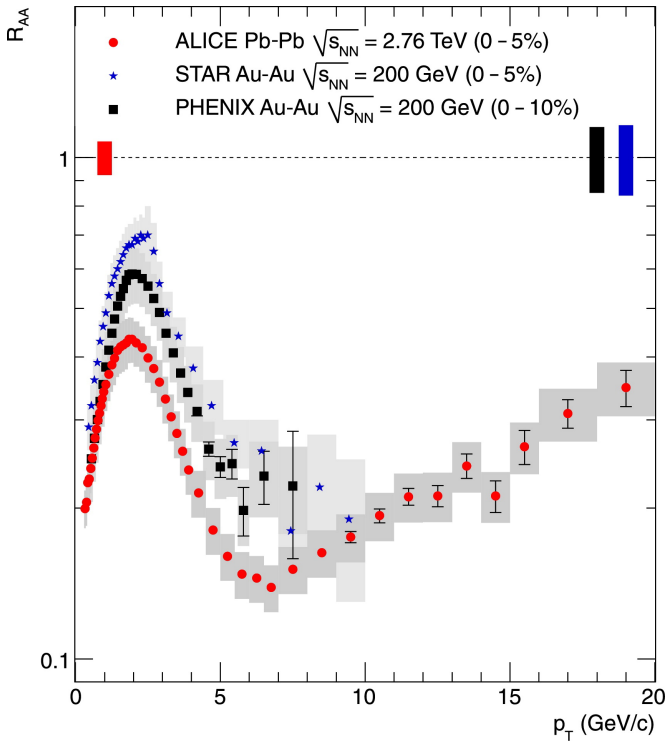

Figure 2.9: Charged-particle R_{AA} for central collisions from ALICE, STAR, and PHENIX. The ALICE data shows a stronger suppression than the RHIC data.

formed.

While the energy loss of the partons cannot be directly measured, it will be reflected in the final-state distribution of the hadrons measured in the detector. The common experimental method of measuring high-p_{T} suppression is to compare the p_{T} spectrum measured in AA collisions to that from pp collisions, where the latter has been scaled to match the number of colliding nucleons in the AA system. This is known as the *nuclear modification factor* or R_{AA}. Fig. 2.9 shows the R_{AA} in central collisions measured by ALICE, STAR, and PHENIX [33]. The plot shows a stronger suppression at the LHC, suggesting an enhanced energy loss and a denser medium than that found at RHIC.

Jet quenching

A similar effect to single-particle high-p_{T} suppression is *jet quenching*. As a hard-scattered parton flies away from the hadron in which it previously existed, it will fragment into many

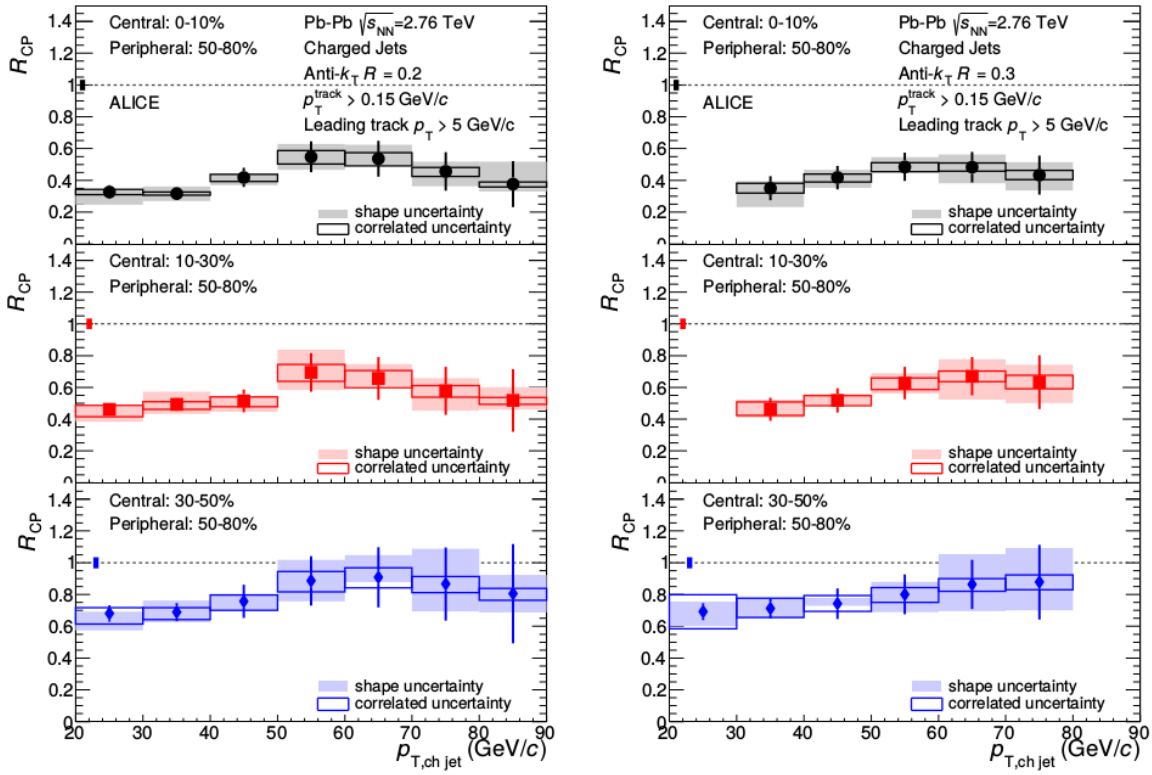

Figure 2.10: Nuclear modification factor R_{CP} for charged jets from ALICE.

new hadrons which will travel together in a "jet". Reconstruction of the entire jet, rather than just looking at each individual hadron, allows more direct access to the parton energy by integrating over the hadronic degrees of freedom. The effect on the jets should be similar to that of the individual hadrons: due to the energy loss suffered by the parton in the QGP medium, we expect a suppression of the number of high-p_{T} jets in AA collisions compared to that from a colliding system where we would not expect a QGP to form. Fig. 2.10 shows the ALICE jet-quenching results [34]; in this case, the ratio presented is R_{CP}, which is the ratio of central collisions divided by peripheral collisions (here, 50-80%), where we would expect to find a much less dense system. One can clearly see the suppression of $\approx 50-70\%$ in central collisions and a diminishing suppression as one goes to more peripheral collisions.

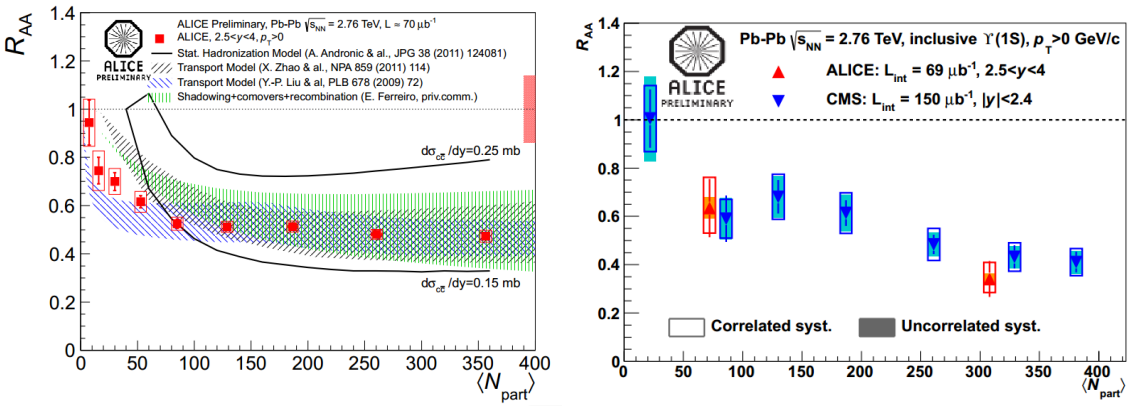

Figure 2.11: ALICE results for J/ψ (left) and Υ (right) suppression in Pb-Pb collisions.

Quarkonium suppression

Another method used to study the QGP is the analysis of heavy quark–anti-quark bound state mesons known as *quarkonium*. These come in two flavors: *charmonium*, a $c\bar{c}$ state whose ground state particle is known as J/ψ; and *bottomium*, the $b\bar{b}$ state represented by the Υ particle. In a QGP, the deconfined medium exhibits the effect of color screening, which is the damping of the color field caused by the presence of mobile color charge carriers, similar to Debye screening in electromagnetism. If the screening length becomes smaller than the binding radius of the $q\bar{q}$ system, the quarkonium will dissolve, i.e. the quark will no longer "see" its anti-quark partner. Thus, one should expect a suppression in the charmonium yield measured in heavy-ion collisions [35].

Fig. 2.11 shows the ALICE results [36] for J/ψ and Υ suppression, which is measured using R_{AA}, the aforementioned ratio of the yield in Pb-Pb collisions to that from scaled pp collisions. A clear suppression is seen, suggesting the presence of a hot, deconfined QGP medium. A similar analysis has been performed in p-Pb collisions, which allow one to study *cold nuclear effects*, i.e. the effects present before and during the collision due to the presence of a nucleus. While a suppression is seen in the p-Pb event, it agrees with the predictions of models taking into account these cold nuclear effects without the need for a hot QGP medium [36].

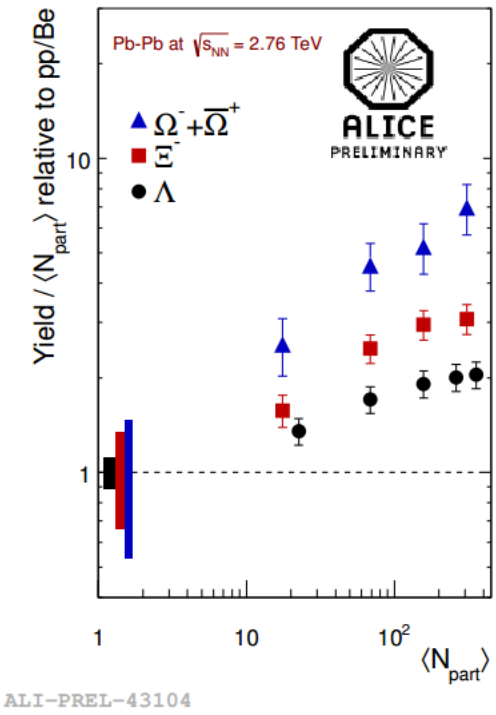

Figure 2.12: Strange hadron yields in Pb-Pb collisions relative to those from *pp* collisions from ALICE [38], showing strangeness enhancement. The reference to Be in the y-axis label is for a related plot that is not shown here.

Strangeness enhancement

Since the valence quarks of the colliding nuclei consist of only u and d quarks, s quarks must be produced in the hard collisions ($s\bar{s}$ created by broken color flux tubes) and will be suppressed compared to the lighter quarks due to their masses. However, in a QGP, extra $s\bar{s}$ pairs can be created via gluon fusion, and the deconfined partons (u, d, s, and g) can reach a chemical equilibrium which would lead to an increase in final-state strange hadron production [37].

Fig. 2.12 shows the ALICE results [38] of the strange particle yields in Pb-Pb collisions relative to those from *pp* collisions. A clear enhancement is seen for all particles and increases with event multiplicity. The enhancement also increases with the strangeness content of the particle, i.e. $\Omega^-(sss) > \Xi^-(dss) > \Lambda(uds)$.

Flow

Another signature of the QGP is the hydrodynamic flow of particles, specifically in the transverse direction where the flow must be created by pressure gradients between the hot center of the system and the vacuum beyond the edge. The discovery of hydrodynamic flow in high-energy nuclei collisions was one of the main forces behind the paradigm shift in the heavy-ion community from the expectations of the QGP exhibiting ideal-gas-like behavior to the realization that it is in fact a strongly-coupled plasma that behaves like a liquid. To be clear, while the formation of a QGP will necessitate a flowing system, the presence of flow does not by itself signal the presence of a QGP [39]. However, models which combine an early hydrodynamic QGP phase followed by a non-fluid hadronic phase describe the data well [40]. In fact, one of the main motivations for studying flow is to provide us with constraints on the properties of the system with respect to the different phases, e.g. initial conditions, equation of state, viscosity, and the specific contributions from the hadronic and partonic phases [41].

In particular, one usually looks at *anisotropic flow*, which measures the anisotropy of the detected momentum distribution as a function of the azimuthal angle. For non-central AA collisions, the overlapping region of the colliding nuclei has an almond shape, and the pressure gradients that arise between the center of the hot, dense medium and the edge of the system vary with the azimuthal angle ϕ. These anisotropic gradients lead to anisotropies in the momentum distribution of the emitted particles. The parameters that one studies are the flow coefficients [42], which are defined as

$$v_n = \langle \cos\left[n(\phi - \Psi_n)\right] \rangle, \tag{2.1}$$

where ϕ is the azimuthal angle, n is the order of the flow harmonic, Ψ_n is the n^{th}-order reaction plane, and the brackets denote the average over all particles and (usually) all events. Fig. 2.13 shows various results for the second-order flow coefficient v_2, commonly known as *elliptic flow*. The left plot shows an increase in v_2 of about 30% from RHIC to LHC. This increase is attributed to an overall increase in average p_{T}, as it can be shown

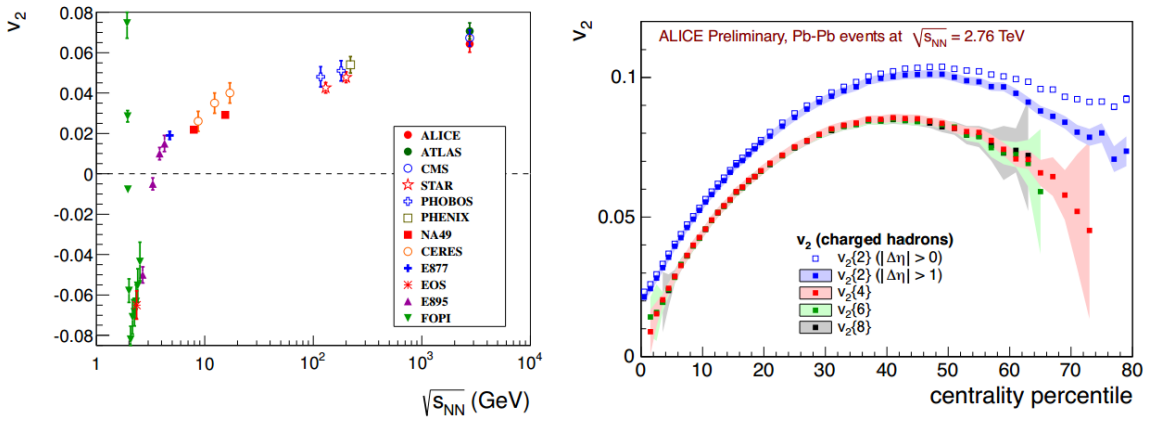

Figure 2.13: (Left) Results of integrated v_2 measurements by various experiments (plot taken from [41]. (Right) ALICE integrated v_2 vs. centrality [44].

that $v_2(p_T)$ does not depend on beam energy [43]. The right plot shows ALICE v_2 results as a function of centrality [44]. One can see that the flow coefficient initially increases with centrality percentile (more peripheral); this reflects the increasing initial spatial anisotropy of the collision zone (circular central collisions vs. almond peripheral collisions).

Besides v_2, higher-order flow coefficients have recently become a hot topic in the heavy-ion community. For example, the third-order flow coefficient v_3, or *triangular flow*, was originally expected to be zero due to the fact that there is no "triangular" shape to the collision overlap region; in fact, all odd coefficients were expected to be zero by symmetry considerations. However, fluctuations in the initial-state positions of the partons in the colliding nuclei can cause non-elliptic shapes in the collision region and subsequently generate non-zero higher-order flow coefficients. Since finding the coefficients of an event-averaged sample will wash out these fluctuations (at least for the odd harmonics), these coefficients are calculated using an event-by-event analysis, where one calculates the coefficients for each event separately, recovering the fluctuations, and then averages the single-event results over many events to increase statistics. The goal of these studies is to provide stronger constraints on the initial geometry and a more sensitive measure of viscosity [45].

Femtoscopy

As this is the main topic of this thesis, please see Chapter 4 for a discussion of femtoscopic results and their relation to the QGP.

Chapter 3
Experimental Set-up

This chapter will discuss the experimental set-up that was used to create the data upon which this analysis was performed. The two main sections will be about the Large Hadron Collider (LHC), the particle accelerator and collider at CERN used to create the data studied here, and ALICE (A Large Ion Collider Experiment), the specific experiment/detector/collaboration of which this analysis was a part.

3.1 The Large Hadron Collider at CERN

3.1.1 Motivation and history

The LHC project was approved by CERN in 1994, and was designed to be a 14 TeV center-of-mass energy proton-proton collider which would also be able to accelerate heavy ions to higher collision energies than ever before [46]. This new collider was constructed in the same tunnel used by the CERN LEP experiment, which ran from 1989 to 2000. The tunnel is 26.7 km in circumference and situated between 45 m and 170 m below the surface of the countryside along the France-Switzerland border near Geneva, Switzerland. The physics motivation of the LHC (as of its proposal stages in the early 1990s) focused on several main points: precise testing of the Standard Model of particle physics; investigating spontaneous symmetry breaking by looking for the Higgs boson; understanding dark matter by searching for supersymmetric particles or heavy neutrinos; and searching for the quark-gluon plasma [47]. The first three of these were to be studied by the CMS and ATLAS collaborations, while the fourth was to be investigated by the ALICE collaboration; all of

these groups were approved by the CERN research board in 1997 [48].

After nearly a decade of work, the LHC circulated its first proton beams in September 2008, but was soon forced to shut down for major repairs due to a magnet quenching accident [49]. The first particle collisions occurred in November 2009, followed shortly by an increase in the beam energy to 1.18 TeV, which made the LHC the world's highest-energy particle accelerator, beating Fermilab's record of 0.98 TeV per beam [50]. This record would be continuously broken by the LHC as it ramped up its beam energy until February 2010 when the beam energy reached 3.5 TeV, resulting in proton-proton collisions at $\sqrt{s_{\mathrm{NN}}} = 7$ TeV.

The first run of proton-proton collisions at $\sqrt{s_{\mathrm{NN}}} = 7$ TeV lasted from March 2010 until November 2010 and was followed by a month-long heavy-ion run of Pb-Pb collisions at $\sqrt{s_{\mathrm{NN}}} = 2.76$ TeV. The system created by these ultra-high-energy Pb-Pb collisions exhibited the hottest temperature ever reached in an experiment [51] and suggested the existence of the Quark-Gluon Plasma, confirming the findings of the RHIC experiments [7–10]. The second runs of both *pp* and Pb-Pb collisions occurred in 2011 at the same energies as 2010, with an additional small *pp* run at $\sqrt{s_{\mathrm{NN}}} = 2.76$ TeV that was used as a reference sample for heavy-ion analyses. During the main *pp* run, the LHC set the world record in beam intensity at a hadron collider with a luminosity of 4.67×10^{32} cm^{-2} s^{-1} [52]. In 2012, the *pp* collision energy was bumped up to $\sqrt{s_{\mathrm{NN}}} = 8$ TeV, and in July of that year, the ATLAS and CMS collaborations announced that they discovered a new particle which would later be identified as the Higgs boson [53,54]. This discovery directly led to the 2013 Nobel Prize for Physics being awarded to the theorists who discovered the Higgs mechanism [55]. By the end of the first *pp* physics program in December 2012, the LHC was operating at a peak luminosity of 7.7×10^{33} cm^{-2} s^{-1}, and had accumulated nearly 30 fb^{-1} of *pp* data in each of the ATLAS and CMS experiments [56]. To put this in perspective: in roughly 10 years of running since 2001, the Tevatron collider produced 10 fb^{-1} of data [57]; by the summer of 2012, the LHC was delivering a peak integrated luminosity of 1.35 fb^{-1} *each week* [58].

Instead of performing another Pb-Pb run, the heavy-ion program at the LHC decided to study *p*-Pb collisions at $\sqrt{s_{\mathrm{NN}}} = 5.02$ TeV in late 2012 and early 2013. These collisions

serve mainly as a reference sample for Pb-Pb studies; in particular, they are used to help disentangle between initial- and final-state effects in high-energy heavy-ion collisions [59]. After this run ended in February 2013, the LHC began its first scheduled "Long Shutdown" (LS1), which will last $\sim$ 2 years. The main purpose of the shutdown is to perform work on the magnet interconnections in order to prepare for the large energy increase up to $\sqrt{s_{\mathrm{NN}}} = 13$ TeV for pp collisions[6]. The individual experiments will also take this time to perform maintenance and install upgrades to their detectors (see [60–62] for more details). The end of LS1 and the recommencement of collisions and physics programs are scheduled for early 2015.

3.1.2 LHC accelerator

The LHC is composed of two counter-rotating beams of protons or Pb ions. Each of the beam paths is made up of eight arcs and eight straight sections. Four of these straight sections are used as beam crossing points and are the locations of the LHC's four main experiments: ATLAS, CMS, ALICE, and LHCb. Another one of the straight sections houses the RF system that is used to accelerate the beam. The LHC uses superconducting magnets to control the beams; dipole magnets are used to bend the particles in a circular path, while quadrupole magnets are used to keep the circulating particles focused along the beam line. The magnets are cooled with superfluid helium down to below 2 K and can produce fields up to 8 T needed for the maximum proton beam energy of 7 TeV.

The LHC is fed by a series of smaller accelerators (see Fig. 3.1). The proton injection chain [64] begins in Linac2, where they are accelerated up to 50 MeV. The Proton Synchtrotron Booster increases the energy to 1.4 GeV, followed by an acceleration up to 25 GeV in the Proton Synchrotron (PS). The Super Proton Synchrotron (SPS) boosts the protons to 450 GeV before feeding into the LHC, where the final acceleration takes place. The Pb ion injection chain [64] begins with the production of Pb^{27+} ions in the Electron Cyclotron Resonance Ion Source (ECRIS). Linac3 accelerates the Pb ions to 4.2 MeV/n(ucleon)

[6] A recent decision has been made to only go to 6.5 TeV per beam rather than the planned 7 TeV due to constraints on time needed to "train" the magnets to handle the larger necessary currents.

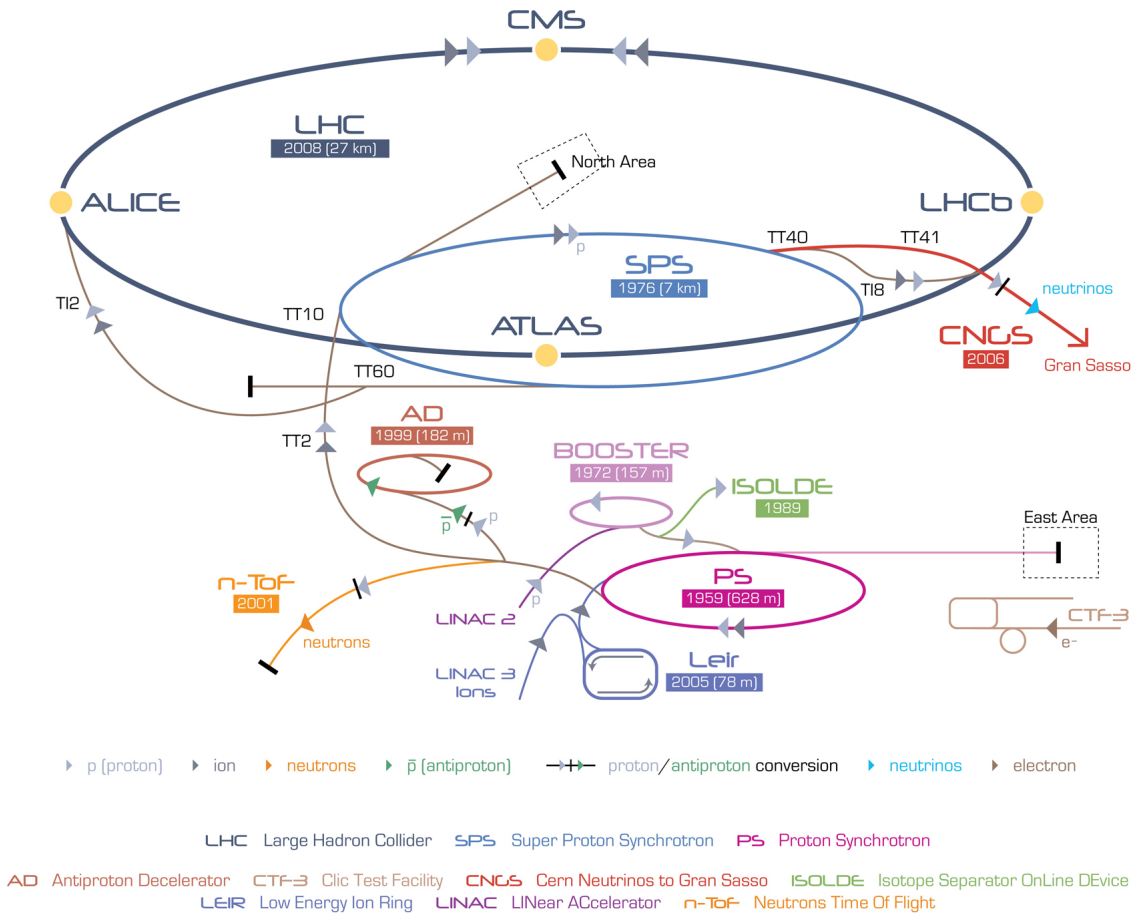

Figure 3.1: LHC layout and injection chain [63].

while stripping electrons to create Pb^{54+} ions. The heavy ions move to the Low Energy Ion Ring (LEIR), where they are accelerated to 72.2 MeV/n. Next, the PS boosts the Pb ions to 5.9 GeV/n and performs further electron stripping to create the desired Pb^{82+} ions, or simply Pb^{208}_{82} nuclei. The SPS then accelerates the Pb nuclei to 176.4 GeV/n, after which they are sent to the LHC for their final acceleration and subsequent collisions.

The proton and heavy-ion "beams" are actually several bunches of particles spaced out along the pipe length. The LHC is designed [46] to hold $\sim$ 2800 proton bunches with a bunch spacing of 25 ns. Each bunch contains $\sim 10^{11}$ protons. For heavy ions, the LHC can hold $\sim$ 600 bunches of 7×10^7 Pb ions with a bunch spacing of 100 ns. Note: these are the ultimate design values; the actual number of bunches used to date is generally lower than

this (but on the same order of magnitude).

3.1.3 LHC experiments

The LHC is home to many experiments which study high-energy collisions. The two largest collaborations, ATLAS (A Toroidal LHC ApparatuS) [65] and CMS (Compact Muon Solenoid) [66], are all-purpose collider experiments which study all sorts of high-energy particle physics, such as high-precision Standard Model (and "beyond") physics; searches for the Higgs boson, dark matter, and supersymmetric particles; and some heavy-ion physics. ALICE (A Large Ion Collider Experiment) [67] is the LHC's dedicated heavy-ion experiment, which focuses on the search for and subsequent study of the characteristics of the Quark-Gluon Plasma. The fourth "large" collaboration is LHCb [68], which studies CP-violation and rare decays of B hadrons. Three smaller experiments that also use the LHC are TOTEM (TOTal Elastic and diffractive cross-section Measurement) [69], which measures the total p-p cross section and studies elastic and diffractive scattering; LHCf [70], which measures neutral particles in the very forward rapidity region of collisions and uses this information for cosmic ray models; and MoEDAL (Monopole and Exotics Detector At the LHC) [71], which searches for the magnetic monopole and Stable Massive Particles (SMPs). The locations of these experiments can be seen in Fig. 3.1.

3.2 ALICE

3.2.1 Motivation and history

ALICE is an international collaboration and (mostly) heavy-ion physics experiment that includes over 1000 physicists from ~ 30 countries. The collaboration was formed in the early 1990s after discussions about setting up a dedicated heavy-ion program at the upcoming LHC accelerator complex at CERN. The collaboration submitted a technical proposal [72] to CERN in 1995, outlining their proposed detector and research program, and the proposal was accepted by CERN in 1997. The initial motivation for the ALICE heavy-ion program was to investigate strongly-interacting matter at extremely high energy densi-

ties [72], specifically to study the QCD-predicted phase transition from hadronic matter to deconfined quarks and gluons, i.e. the Quark-Gluon Plasma [73, 74].

By the time the LHC and ALICE became operational in 2010, it was established by the heavy-ion community that the QGP had indeed been found by the experiments at RHIC [7–10], and possibly even earlier at the CERN SPS [75]. Therefore, ALICE's main goals [76] during its first physics program were not simply to "find" the QGP, but to study its characteristics; to explore the phase diagram of strongly-interacting matter; to study the phase transition between hadronic matter and the QGP; and to investigate the physical properties of the QGP (see Ch. 2 for more details). Also, besides QGP physics, ALICE researchers investigate proton-proton and proton-nucleus collisions, which are often used as reference samples for Pb-Pb collisions while also exhibiting interesting physics of their own; ultra-peripheral heavy-ion collisions, where electromagnetic interactions can be studied; and cosmic-ray physics.

3.2.2 The ALICE detector

The ALICE detector [67], which is sometimes referred to as the "smaller" LHC detector compared to ATLAS and CMS, is a $16 \times 16 \times 26$ m^3 machine made up of many subdetectors that each perform different tasks and are used for various analyses. I will first briefly describe all of the subdetectors and other parts of the ALICE detector and then more thoroughly discuss several subdetectors that are important for the analysis in this thesis. A schematic view of the ALICE detector and its subdetectors can be seen in Fig. 3.2.

The central barrel of the ALICE detector covers the pseudorapidity region $|\eta| < 0.9$ and the full azimuthal range and is used mainly for particle tracking and identification. Closest to the beam line lies the Inner Tracking System (ITS) [77], which consists of layers of silicon pixel (SPD), drift (SDD), and strip (SSD) detectors. The ITS performs high-resolution tracking and helps localize the primary vertex of the collision . The Time Projection Chamber (TPC) [78] is the main tracking detector of the ALICE central barrel and helps with particle identification (PID). The Transition-Radiation Detector (TRD) [79] is used for electron identification at high momentum. The Time-Of-Flight (TOF) detector [80] is a

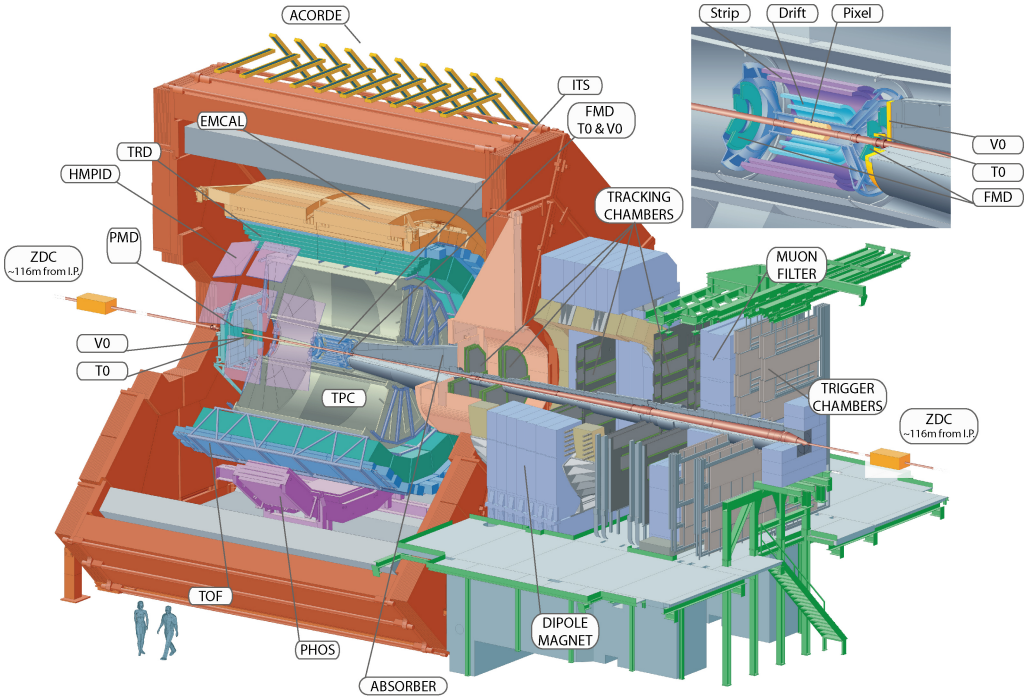

Figure 3.2: An inside look at the ALICE detector with all of its subdetectors.

Multi-Gap Resistive-Plate Chamber (MRPC) used for PID. The High-Momentum Particle Identification Detector (HMPID) [81] uses Ring Imaging Cherenkov (RICH) detection to perform PID at momentum up to several GeV/c. The PHOton Spectrometer (PHOS) [82] is an electromagnetic spectrometer which provides identification of photons and, by extension, neutral mesons (through the two-photon decay channel). The ElectroMagnetic Calorimeter (EMCal) [83] helps measure high-momentum photons and electrons which are important for the reconstruction of high-momentum jets.

Several smaller detectors are located in the forward (and/or backword) η regions of the ALICE detector and are used primarily for triggering or measuring global event characteristics. The Zero Degree Calorimeter (ZDC) [84] measures spectator nucleons (both protons and neutrons), which help determine the event centrality as well as the event plane (i.e. direction of the impact parameter). The Photon Multiplicity Detector (PMD) [85] provides estimates of the event transverse electromagnetic energy and the event plane. The Forward Multiplicity Detector (FMD) [86] helps with multiplicity and event plane determination.

The VZERO detector [86](formerly V0), located on either side of the interaction point, is a series of scintillator counters whose multiplicity measurements are very useful for triggering and event centrality determination. The T0 detector [86] uses Cherenkov counters to provide a start time for the TOF detector and early ("L0") triggering.

Other subdetectors in the ALICE machine include the muon spectrometer [87], which is located in the backward η region and is used in the reconstruction of heavy-flavor decays, and the ALICE COsmic Ray Detector (ACORDE) [88]. ALICE has two main magnets: a room-temperature solenoid around the central detector, used to bend charged particles for the purpose of particle identification; and a dipole magnet which is part of the forward muon spectrometer [67].

3.2.3 Main subdetectors used in this analysis

Here, I briefly describe the subdetectors that are important to this analysis. The descriptions will focus mainly on the design and performance of each detector; for a more in-depth discussion about certain aspects of the experimental analysis associated with the detectors, such as tracking and particle identification, see Ch. 6.

Inner Tracking System (ITS)

The ITS [77] is the detector closest to the beam, ranging from 4 to 43 cm radially from the beam line, and is centered around the collision interaction point. It is made up of six individual cylindrical layers, two layers each of silicon pixel (SPD), drift (SDD), and strip (SSD) detectors. These silicon layers detect charged particles passing through them, and are used together to reconstruct the particle paths as they leave the interaction region. Some of the layer specifications can be found in Table 3.1. The main goal of the ITS is to be able to track individual particle paths near the interaction point, where the particle density is very high ($\sim$8000 tracks per unit rapidity). This allows the ITS to locate the primary vertex of the event with a resolution better than 100 μm. The ITS is used together with the TPC for overall particle tracking and PID, though it can be used by itself to reconstruct and identify tracks which travel along dead zones in the TPC (e.g. between TPC sectors)

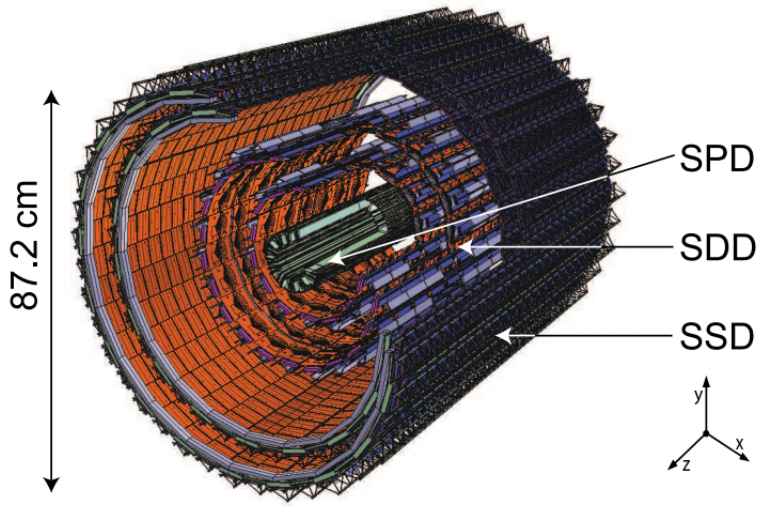

Figure 3.3: An inside look at the ALICE ITS [67].

Layer	r (cm)	z (cm)	# of modules	Active area per module $r\phi \times z$ (mm^2)	Resolution (μm)	
					$r\phi$	z
pixel	3.9	14.1	80	12.8 × 70.1	12	100
pixel	7.6	14.1	160	12.8 × 70.7	12	100
drift	15.0	22.2	84	70.2 × 75.3	35	25
drift	23.9	29.7	176	70.2 × 75.3	35	25
strip	38.0	43.1	748	73.0 × 40.0	20	830
strip	43.0	48.9	950	73.0 × 40.0	20	830

Table 3.1: Specifications of the ITS.

or decay before reaching the TPC.

The two SPD layers are used primarily for primary vertex determination due to their ability to work in high track-density regions (as high as 50 tracks/cm^2). The SDD and SSD are used together for the ITS PID of low-momentum particles (up to $p_{\mathrm{T}} \sim 1$ GeV/c), and the SDD is important for matching tracks between the ITS and the TPC. Figs. 3.4 and 3.5 show the PID capabilities and vertex efficiencies of the ITS, respectively. ITS PID is performed using specific energy loss dE/dx measurements and can identify pions down to $p_{\mathrm{T}} \sim 100$ MeV/c with a dE/dx resolution of 10-15% [89].

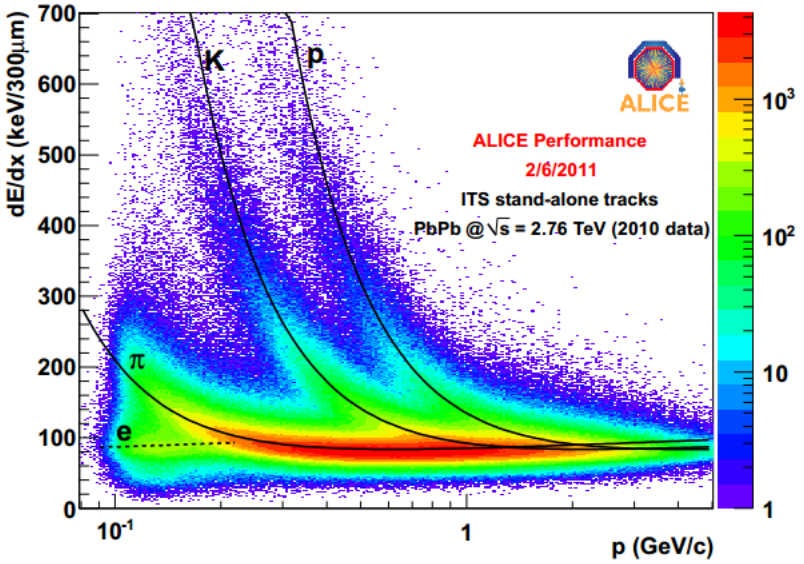

Figure 3.4: dE/dx measurements as a function of momentum measured by ITS standalone tracks [90].

.

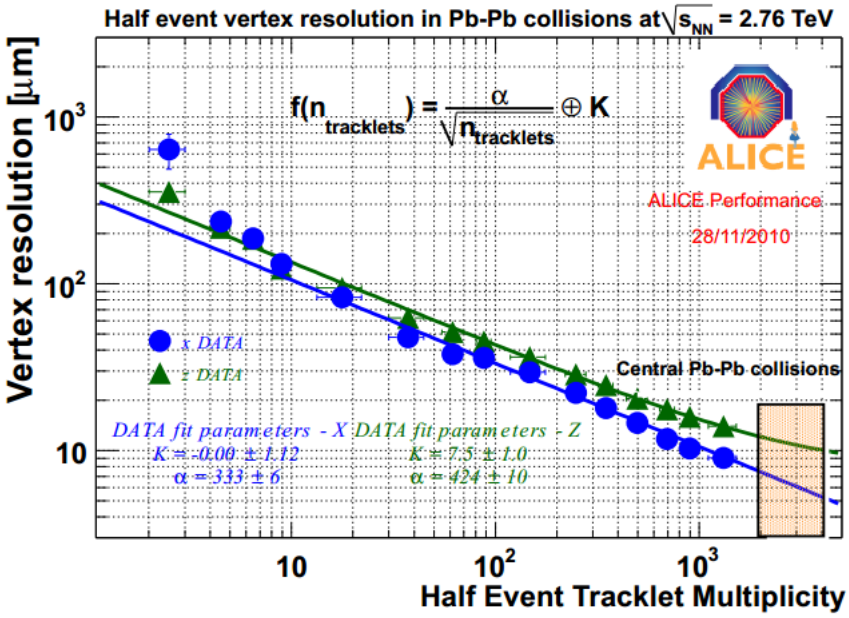

Figure 3.5: Vertex resolution in Pb-Pb collisions as a function of half of the event tracklet multiplicity, where a tracklet is defined as a pair of aligned SPD hits, one in each layer [90]. The orange box denotes the 0-5% centrality class.

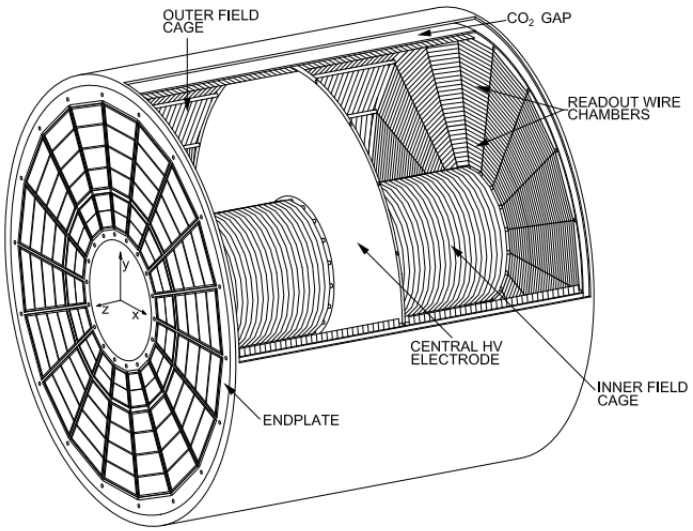

Figure 3.6: 3D view of the TPC field cage [91].

Time Projection Chamber (TPC)

The TPC [78] is located in the central barrel surrounding the ITS and stretches from 85 cm out to 250 cm radially and 5 m along the beam direction, allowing full radial track-length coverage in the pseudorapidity region $|\eta| < 0.9$ and an acceptance out to $|\eta| < 1.5$ for reduced track length. The TPC covers the full azimuthal range. Fig. 3.6 shows a simple view of the TPC cage.

The ALICE TPC is a traditional drift chamber in which charged particles ionize the constituent gas (here, an 85/10/5% mixture of $Ne/CO_2/N_2$), and the freed electrons "drift" through an electric potential toward cathodes situated at the end plates. The end plates are segmented into $\sim$ 560000 "pads", which register the "hits" of the ionized electrons. The z-direction of the track is determined by the time taken by the electron drift, while r and ϕ are determined by recording which end-plate pad received the "hit". For the ALICE TPC, the resolution on the track position is $\sim$ 1000 μm in both $r\phi$ and z [91]. The TPC has a tracking efficiency of $\approx$ 80% in the central-η region and momentum resolution of $\approx$ 5%. The TPC also uses dE/dx measurements to identify charged particles up to $p \sim$ 1-2 GeV/c with a resolution of $\approx$ 5% for isolated tracks.

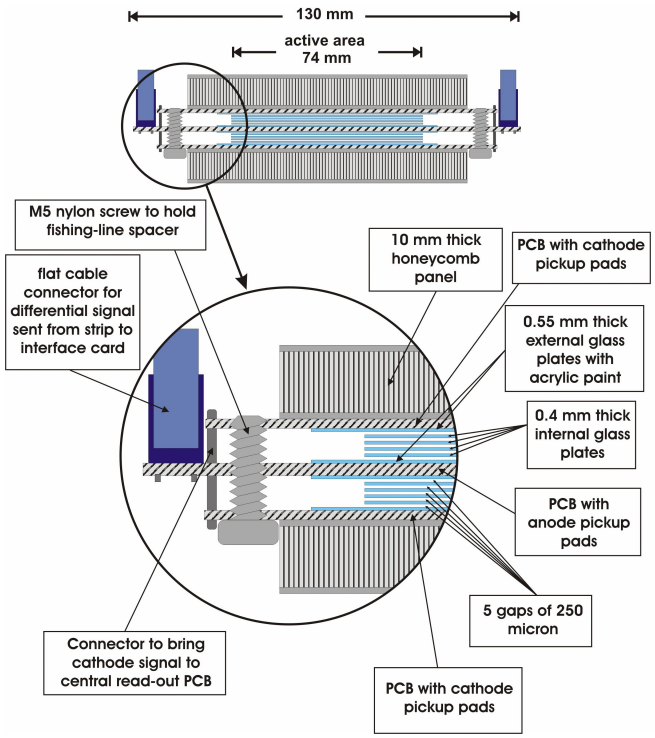

Figure 3.7: A close-up view of the parallel plate setup of the ALICE Time-Of-Flight (TOF) detector (picture taken from ALICE Bologna Group).

Time-Of-Flight (TOF) detector

The TOF detector [80] has a cylindrical surface covering 141 m^2 at a radius of 3.7 m from the beam line. It has a pseudorapidity acceptance of $|\eta| < 0.9$ and full azimuthal acceptance. It uses Multigap Resistive Plate Chambers (MRPCs), which consist of two stacks of glass plates (400 μm thick) separated by gas gaps (250 μm width). The TOF detector uses 1593 of these stacks, which can be seen in Fig. 3.7. The TOF matching efficiency, which is defined as the ratio of the number of TPC tracks that also produced a TOF signal over the total number of TPC tracks, is about 0.6-0.7 for $p_{\mathrm{T}} > 0.5$ GeV/c [92].

The TOF detector is used to obtain charged-particle velocities by measuring the time difference between an initial time (usually taken from the T0 detector or calculated using the TOF detector itself) and the time of detection. The ALICE TOF has a time resolution of ≈ 80 ps for pions around $p \sim 1$ GeV/c [93], which allows for a two-sigma separation up

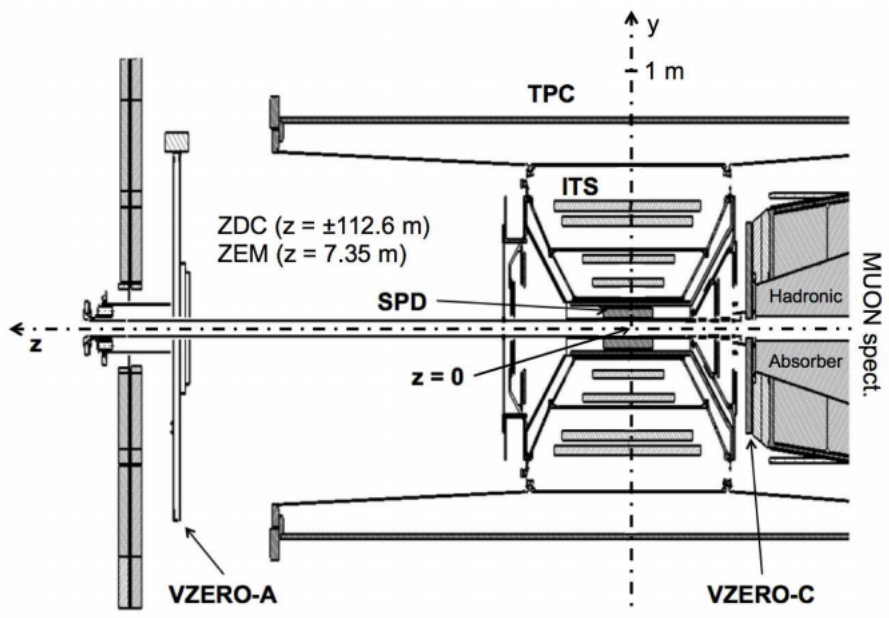

Figure 3.8: The positions of the two VZERO arrays within the ALICE detector [94].

to $p \approx 3$ GeV/c for π–K and up to $p \approx 5$ GeV/c for K–p.

VZERO detectors

The VZERO detector [86] consists of circular arrays of scintillator counters, one located at each end of the ALICE machine. The two arrays VZERO-A and VZERO-C are located at 329 cm and -86 cm from the ALICE coordinate origin and cover the pseudorapidity ranges $2.8 < \eta < 5.1$ and $-3.7 < \eta < -1.7$, respectively. Fig. 3.8 shows a picture of the VZERO detectors and their positions within the ALICE detector.

The VZERO detector is used as the default collision centrality determinator for ALICE Pb-Pb collisions. The charged-particle amplitudes measured by the VZERO arrays are used to define centrality classes (see Ch. 6 for details). The centrality-percentile resolution for the VZERO is better than 2% for all centralities and reaches as good as 0.5% for very central collisions [95]. The VZERO also participates in the triggering system for ALICE and, with its centrality-determination capabilities, was able to deliver three centrality-dependent triggers (minimum bias, 0-50%, and 0-10%) during the 2011 Pb-Pb run.

Chapter 4
Femtoscopy

Femtoscopy is an analysis method used by physicists to extract information about the spatial and temporal characteristics of the kinetic freeze-out of particles escaping from a high-energy collision. In short, the method involves studying the relative momentum distributions of detected particles, which are sensitive to various factors affecting the momenta of a pair of particles, such as quantum statistics (Bose-Einstein or Fermi-Dirac) and final-state interactions (Coulomb or strong). From these distributions, one can extract the size of the particle-emitting regions of the collision system as well as gain additional information about emission duration, the shape of the emission region (via azimuthal femtoscopy), and relative emission positions (via non-identical femtoscopy). These characteristics can shed light on the dynamics of the evolving reaction zone of collision systems and are sensitive to several factors related to the presence of the QGP, such as the system lifetime and collective flow.

4.1 Introduction

The basic idea behind femtoscopy is known as *intensity interferometry*, which began with the work of Hanbury Brown and Twiss [96, 97], who developed this form of interferometry in order to measure the angular size of stars. The original method of measuring the size of astronomical objects was through the use of Michelson interferometry, where one interferes the amplitudes of light at two different "detection points" by converging them with a lens and studying the diffraction pattern. However, the resolution of this method was limited by the distance of separation between the detection points. Hanbury Brown and Twiss

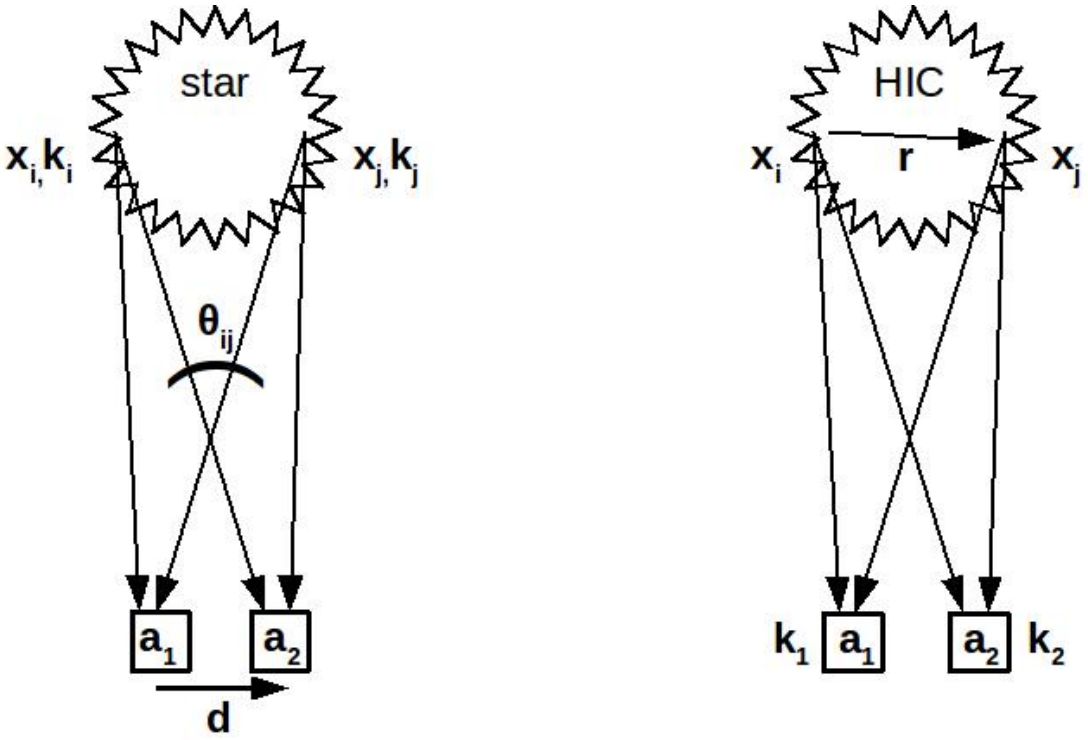

Figure 4.1: Schematic diagram [98] of intensity interferometry used in astronomy (left) and particle physics (right).

realized that if the radiation measured at two different places was mutually coherent, then one could find a correlation in the fluctuations of the intensities of the signals rather than their amplitudes. Without the need for explicit amplitude interference, the measurement method would not be limited by space needed for detection. Even though the interferometry used in femtoscopic analyses today is different than this original method, the importance of this work is noted in the fact that femtoscopy has historically been known as "HBT interferometry".

Intensity interferometry was independently discovered and first used in particle collisions by the team of Goldhaber, Goldhaber, Lee, and Pais [99], who lent their names to another historical name for femtoscopic correlations, the "GGLP effect". The methods used in particle physics and astronomy are different in a subtle but important way. Fig. 4.1 shows the two-particle interference mechanisms used in astronomy (left) and particle physics (right). In astronomy, the photon wavevector is associated with a definite emission point, and the

ambiguity in the two-particle coincident measurement comes from the interchange of the detectors. In particle physics, the particle wavevector is associated with a certain detection point, and the ambiguity comes from the interchange of the emission points.

More rigorously, the two-particle wavefunction corresponding to the two-photon detection coincidence in astronomy (left diagram of Fig. 4.1) is

$$\Psi(\vec{k}_{\rm i},\vec{k}_{\rm j};\vec{x}_{\rm i},\vec{x}_{\rm j}) \sim e^{i\vec{k}_{\rm i}\cdot(\vec{a}_1-\vec{x}_{\rm i})}e^{i\vec{k}_{\rm j}\cdot(\vec{a}_2-\vec{x}_{\rm j})} + e^{i\vec{k}_{\rm i}\cdot(\vec{a}_2-\vec{x}_{\rm i})}e^{i\vec{k}_{\rm j}\cdot(\vec{a}_1-\vec{x}_{\rm j})} \tag{4.1}$$

where the second term reflects the path ambiguity in detecting identical bosons. The probability of coincident detection $P_{\rm i,j}$ is the square of the wavefunction $|\Psi|^2$, or

$$P_{\rm i,j}(\Delta\vec{k},\vec{d}) \sim 1+\cos(\Delta\vec{k}\cdot\vec{d}) \tag{4.2}$$

where $\Delta\vec{k}=\vec{k}_{\rm i}-\vec{k}_{\rm j}$ and $\vec{d}=\vec{a}_1-\vec{a}_2$. Using the approximations $k_{\rm i}\approx k_{\rm j}\equiv k$, $\Delta\vec{k}\cdot\vec{d}\approx|\Delta\vec{k}|d$, and $|\Delta\vec{k}|\approx\theta_{\rm ij}k=2\pi\theta_{\rm ij}/\lambda$, one gets

$$P_{\rm i,j}(d) \sim 1+\cos(2\pi\theta_{\rm ij}d/\lambda) \tag{4.3}$$

Then, one simply varies the separation of the detectors to create the distribution $P_{\rm i,j}(d)$ and extract the angular size $\theta_{\rm ij}$.

In particle physics, the two-particle wavefunction corresponding to the two-boson detection coincidence (right diagram of Fig. 4.1) is

$$\Psi(\vec{k}_1,\vec{k}_2;\vec{x}_{\rm i},\vec{x}_{\rm j}) \sim e^{i\vec{k}_1\cdot(\vec{a}_1-\vec{x}_{\rm i})}e^{i\vec{k}_2\cdot(\vec{a}_2-\vec{x}_{\rm j})} + e^{i\vec{k}_1\cdot(\vec{a}_1-\vec{x}_{\rm j})}e^{i\vec{k}_2\cdot(\vec{a}_2-\vec{x}_{\rm i})} \tag{4.4}$$

where the wavevector is associated with the detection point, and the emission point is now exchanged. The probability is then

$$P_{\rm i,j}(\Delta\vec{k},\vec{d}) \sim 1+\cos(\Delta\vec{k}\cdot\vec{r}) \tag{4.5}$$

where $\vec{r}=\vec{x}_{\rm i}-\vec{x}_{\rm j}$. Then, one can study a distribution of $\Delta\vec{k}$ to gain information about the emission separation $\vec{r}$.

These expressions are assuming discrete sources, when in actuality we are dealing with a continuum of sources. Thus, rather than simply looking at the discrete probability $|\Psi|^2$,

we want to average over the relative distance distribution $\rho(\mathbf{r})$ and look at $\int d^3\mathbf{r}\rho(\mathbf{r})|\Psi|^2$.

The prescription shown above can be amended for use with fermions. Instead of the wavefunction symmetrization due to the two-boson exchange, the two-fermion exchange will lead to an anti-symmetrized wavefunction, changing the "+" signs in Eqs. 4.4 and 4.5 to "–" signs. Since this thesis deals with bosons, we will generally assume a bosonic system.

4.2 Theoretical formalism

The theoretical formalism in this section follows the formalism presented in the excellent reviews by Heinz [100], Heinz and Jacak [101], and Lisa *et al.* [102]. After the first observations of the GGLP group, the early foundations of correlation femtoscopy were mostly developed in several papers by Kopylov and Podgoretsky in the early 1970s (see [103–105], among others). Many others later built upon these foundations and are cited in the remaining sections of this chapter.

4.2.1 Correlation function

The main tool of femtoscopy is the two-particle correlation function, which is defined as the ratio of the covariant two-particle and single-particle spectra:

$$C(\vec{p}_1,\vec{p}_2) = \frac{E_1E_2\dfrac{dN}{d^3p_1d^3p_2}}{\left(E_1\dfrac{dN}{d^3p_1}\right)\left(E_2\dfrac{dN}{d^3p_2}\right)}. \tag{4.6}$$

In order to gain information about the particle emission, we can relate this experimentally measureable expression to the *source function* $S(x,p)$, which is the single-particle Wigner function that gives the probability of emitting a particle with momentum p from position x. The single- and two-particle spectra and the correlation function can be written as

$$E_p\frac{dN}{d^3p} = \int d^4x\, S(x,p), \tag{4.7}$$

$$E_1E_2\frac{dN}{d^3p_1d^3p_2} = \int d^4x_1\, d^4x_2\, S(x_1,p_1;x_2,p_2)|\Psi(x_1,x_2,p_1,p_2)|^2, \tag{4.8}$$

$$C(\vec{p}_1,\vec{p}_2) = \frac{\int d^4x_1\, d^4x_2\, S(x_1,p_1;x_2,p_2)|\Psi(x_1,x_2,p_1,p_2)|^2}{\int d^4x_1\, S(x_1,p_1)\int d^4x_2\, S(x_2,p_2)}. \tag{4.9}$$

To relate $C(p_1, p_2)$ to $S(x, p)$ in a convenient way, we make a few approximations. First, we assume the bosons are emitted independently, and thus $S(x_1, p_1; x_2, p_2) = S(x_1, p_1)S(x_2, p_2)$. Second, we assume that higher-order symmetrization can be neglected due to small freeze-out phase-space density. Third, we will often talk about the source function and correlation function in terms of the average pair momentum $K = (p_1 + p_2)/2$ and the relative momentum $q = p_1 - p_2$, rewriting the source functions in the denominator of Eq. 4.9 as functions of $p_1 = K + \frac{1}{2}q$ and $p_2 = K - \frac{1}{2}q$. Then, we make the *smoothness approximation* [106], which assumes that the source function has a sufficiently weak momentum dependence at low q that we can write $S(x, K \pm \frac{1}{2}q) \approx S(x, K)$.

In the absence of final-state interactions, the two-boson symmetrized wavefunction (similarly to Eqs. 4.4 and 4.5) is $|\Psi|^2 = 1 + \cos(\mathrm{q} \cdot \mathrm{r})$, where $r = x_1 - x_2$. Then, we can use the assumptions above to write Eq. 4.9 as

$$\begin{aligned} C(\vec{q}, \vec{K}) &\approx \frac{\int d^4x_1 d^4x_2 S(x_1, K)S(x_2, K)\left[1 + \cos(q \cdot (x_1 - x_2))\right]}{\int d^4x_1 S(x_1, K) \int d^4x_2 S(x_2, K)} \\ &= 1 + \frac{\int d^4x_1 d^4x_2 S(x_1, K)S(x_2, K)\left(\frac{1}{2}e^{iq\cdot x_1}e^{-iq\cdot x_2} + \frac{1}{2}e^{-iq\cdot x_1}e^{iq\cdot x_2}\right)}{\int d^4x_1 S(x_1, K) \int d^4x_2 S(x_2, K)} \\ &= 1 + \frac{1}{2}\frac{\int d^4x_1 S(x_1, K)e^{iq\cdot x_1} \int d^4x_2 S(x_2, K)e^{-iq\cdot x_2}}{\int d^4x_1 S(x_1, K) \int d^4x_2 S(x_2, K)} \\ &\quad + \frac{1}{2}\frac{\int d^4x_1 S(x_1, K)e^{-iq\cdot x_1} \int d^4x_2 S(x_2, K)e^{iq\cdot x_2}}{\int d^4x_1 S(x_1, K) \int d^4x_2 S(x_2, K)} \\ &= 1 + \left|\frac{\int d^4x\, S(x, K)e^{iq\cdot x}}{\int d^4x\, S(x, K)}\right|^2 \end{aligned} \tag{4.10}$$

From this, we see that the relative momentum correlation function is essentially a Fourier transform of the relative position source function.

The source function $S(x, p)$ must be evaluated on-shell ($p^0 = E_{\vec{p}} = \sqrt{m^2 + \vec{p}^2}$) for the single-particle spectrum of Eq. 4.8. However, for the on-shell particles we measure in the detector, the momentum combinations q and K will generally be off-shell. Thus, the source function $S(x, K)$ in Eq. 4.10 will not be evaluated on-shell, which means we would need to know its off-shell behavior, i.e. its quantum mechanical structure, in order to fully evaluate the expression for the correlation function [107]. However, the interesting part of the correlation function is at low $|\vec{q}|$, and expanding K^0 around small $|\vec{q}|$ gives $K^0 \approx E_K$.

This is known as the *on-shell approximation*. Using this approximation, we are able to treat the source function $S(x, K)$ as a classical phase-space distribution for on-shell particle pairs of momentum K [107].

For identical particles,

$$\begin{aligned} q_\mu K^\mu &= \frac{1}{2}(m_1^2 - m_2^2) = 0 \\ &\iff q^0 = \vec{\beta}\cdot\vec{q}, \quad \vec{\beta} = \frac{\vec{K}}{K^0} \approx \frac{\vec{K}}{E_{\vec{K}}} \\ &\iff q_\mu x^\mu = -\vec{q}'\cdot\vec{x}' \end{aligned} \tag{4.11}$$

We see that q^0 is not an independent variable, and thus we cannot use Eq. 4.10 to fully reconstruct the four-dimensional $S(x, K)$ via Fourier transform. We can use Eqs. 4.11 and 4.10 to rewrite the correlation function in a convenient way using the pair rest frame (PRF) where $\vec{K}' = 0$ (PRF variables are denoted with primes) as

$$C(\vec{q}, \vec{K}) - 1 = \int d^3\vec{r}' S_{\vec{K}}(\vec{r}') \cos(\vec{q}'\cdot\vec{r}') \tag{4.12}$$

where

$$S_{\vec{K}}(\vec{r}') = \frac{\int d^4x_1\, d^4x_2\, S(x_1, p_1)\, S(x_2, p_2)\, \delta(\vec{r}' - \vec{x}'_1 + \vec{x}'_2)}{\int d^4x_1\, d^4x_2\, S(x_1, p_1)\, S(x_2, p_2)}. \tag{4.13}$$

Here, $S_{\vec{K}}(\vec{r}')$ gives the probability density for two particles with pair momentum $\vec{K}$ being emitted at relative distance $\vec{r}'$ in the PRF when averaged over all emission times.

Eq. 4.12 tells us three important things about the femtoscopic correlation function. First, it allows to use the pair wavefunction $|\Psi|^2$ (here, $|\Psi|^2 = 1 + \cos(\vec{q}'\cdot\vec{r}')$) as a kernel to transform from coordinate space ($S_{\vec{K}}(\vec{r}')$) to momentum space ($C(\vec{q}, \vec{K})$). Section 4.2.2 will discuss the more general case with final-state interactions, and we will do this explicitly using the neutral kaon pair wavefunction in Ch. 5. Second, the coordinate space information that we are studying via the correlation function, i.e. Eq. 4.13, is $\vec{K}$-dependent; we can gain information only about the area of the source emitting particles of a specific pair momentum and not the entire source. This area is often called the "region of homogeneity"[7]. For a static source, these regions of homogeneity can approach the full size of the source; however,

[7]Originally coined by Sinyukov [108].

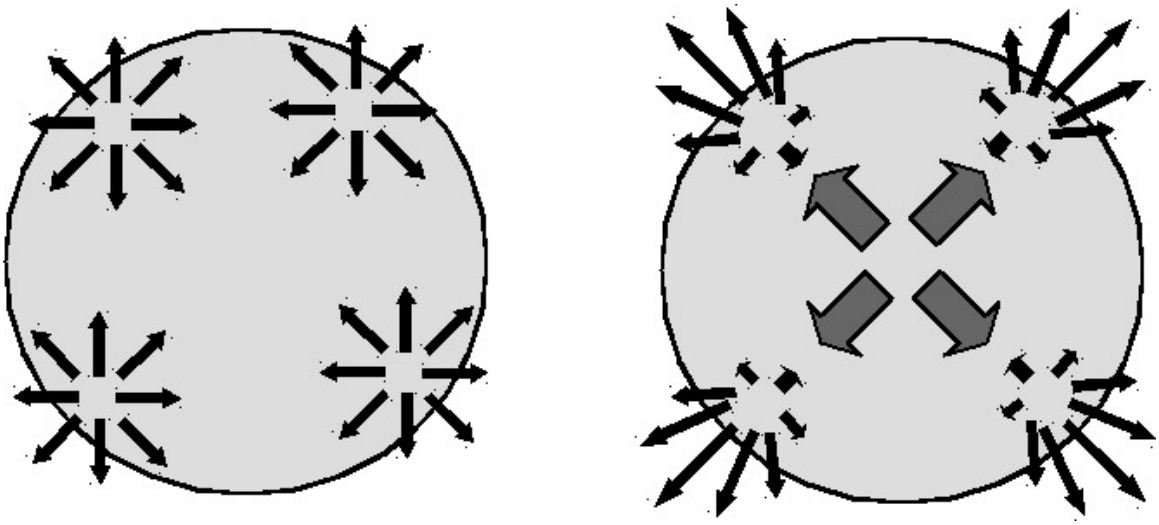

Figure 4.2: View of particle emission in transverse plane. Black arrows represent particle momentum. (Left) Thermal emission[8]from a static source. The region of particles with similar momenta approaches the full source size. (Right) Emission from an expanding source, with collective flow (represented by gray arrows) added to thermal emission. It is still possible for pairs with similar momenta at low pair momentum K_{T} to be emitted from different sides of the source; however, pairs with large K_{T} will only be emitted from the same side of the source.

for an expanding source as we find in heavy-ion collisions, particles with similar momentum will only be found close to each other, and the regions of homogeneity will be smaller than the full size of the source (see Fig. 4.2 for an illustration of this effect).

Lastly, the source function in Eq. 4.13 has been integrated over time, and the correlation function is explicitly three-dimensional, as we stated earlier. No direct information about the temporal aspects of the emission system is extractable. However, one can indirectly study the temporal components by studying the momentum dependence of the extracted source sizes along with some knowledge about the dynamics of the system; this will be discussed later.

[8]Thermal particles will obviously have a distribution of momenta. Here, only one momentum value is drawn for simplicity.

4.2.2 Final-state interactions

The formalism so far has assumed no final-state interactions (FSI). To incorporate FSI, we would replace the factor $e^{iq\cdot x}$ in Eq. 4.10 and, subsequently, the cosine factor in Eq. 4.12 with a distorted wavefunction which describes the scattering interaction. One would then get the *Koonin-Pratt equation* [109, 110]

$$C(\vec{q},\vec{K}) = \int d^3\,\vec{r}\,'\, S_{\vec{K}}(\vec{r}\,')|\Psi(\vec{q}\,',\vec{r}\,')|^2\,, \tag{4.14}$$

where $\Psi(\vec{q}\,',\vec{r}\,')$ is the FSI-distorted scattering wave for the relative motion of the particle pair with asymptotic relative momentum $\vec{q}\,'$, i.e. the solution to the stationary Schrödinger equation [111]. For simplicity, the integral in Eq. 4.14 is written in the pair rest frame. For identical bosons, the wavefunction used in the Koonin-Pratt equation must be symmetrized to reflect the ambiguity under momentum exchange, i.e. $\Psi(\vec{q}\,',\vec{r}\,') \to \frac{1}{\sqrt{2}}\left[\Psi(\vec{q}\,',\vec{r}\,') + \Psi(-\vec{q}\,',\vec{r}\,')\right]$.

For Coulomb FSI, the unsymmetrized wavefunction takes the form [112]

$$\Psi^{\text{Coul}}(\vec{q}\,',\vec{r}\,') = \Gamma(1+\eta)e^{-\frac{1}{2}\pi\eta}e^{\frac{i}{2}\vec{q}\,'\cdot\vec{r}\,'}F(-i\eta;1;iz)\,, \tag{4.15}$$

where $\eta = m\alpha_{\text{QED}}/q$, $z = \frac{1}{2}(|\vec{q}\,'||\vec{r}\,'| - \vec{q}\,'\cdot\vec{r}\,')$, and $F(-i\eta;1;iz)$ is a confluent hypergeometric function. In the past, this formula was used to correct the correlation functions before fitting (see the next section for fitting details); today, analyses generally include the Coulomb effects in the fitting function by using the *Bowler-Sinyukov* formula [112, 113]

$$C(\vec{q},\vec{K}) = (1-\lambda) + \lambda\, K_{\text{Coul}}(q_{\text{inv}})\, C_{\text{BE}}(\vec{q},\vec{K}) \tag{4.16}$$

where $K_{\text{Coul}}(q_{\text{inv}})$ is the two-particle Coulomb wavefunction integrated over a static spherical Gaussian source[9], q_{inv} is the invariant relative momentum $\sqrt{-q_\mu q^\mu}$, and $C_{\text{BE}}(\vec{q},\vec{K})$ is the expression for the correlation function expected from Bose-Einstein correlations without the FSI (see the next section for details). The λ parameter denotes the fraction of pairs that are correlated via Bose-Einstein statistics (again, see below for more details), used primarily to

[9] Other source shapes can be used, but the common prescription is the spherical Gaussian source with a single characteristic width R.

account for the infiltration of non-correlated pairs coming from long-lived decay products.

For strong final-state interactions, the non-symmetrized wavefunction describing elastic transitions is written as a superposition of the plane and spherical waves. For the usual case of s-wave dominated spherical waves, the wavefunction is [111]

$$\Psi(\vec{q}', \vec{r}') = e^{-i\frac{1}{2}\vec{q}'\cdot\vec{r}'} + f\left(\frac{\vec{q}'}{2}\right)\frac{e^{\frac{i}{2}q'r'}}{r'} \tag{4.17}$$

where the s-wave scattering amplitude $f(\frac{\vec{q}'}{2}) = \left(\frac{1}{f_0} + \frac{1}{2}d_0\left(\frac{\vec{q}'}{2}\right)^2 - \frac{i\vec{q}'}{2}\right)^{-1}$, f_0 is the scattering length, and d_0 is the effective range of the interaction. For neutral kaons, the scattering amplitude is written differently due to the interaction being dominated by the presence of near-threshold resonances (see Ch. 5).

4.2.3 Gaussian parametrization

In order to extract information about the source function from the measured correlation, one can insert an ansatz expression for the source function over which we can integrate the wavefunction kernel. The most common expression used is the *Gaussian parametrization*, where we make a Gaussian approximation to the space-time dependence of the source function $S(x, K)$ [108, 114, 115]. We write the source function as

$$S(x, K) \approx S(\bar{x}(\vec{K}), K)\exp\left[-\frac{1}{2}\tilde{x}^\mu(\vec{K})\, B_{\mu\nu}(\vec{K})\, \tilde{x}^\nu(\vec{K})\right] \tag{4.18}$$

where

$$\begin{aligned} \bar{x}^\mu(\vec{K}) &= \langle x^\mu \rangle \\ \tilde{x}^\mu(\vec{K}) &= x^\mu - \bar{x}^\mu(\vec{K}) \\ (B^{-1})_{\mu\nu}(\vec{K}) &= \langle \tilde{x}_\mu \tilde{x}_\nu \rangle \end{aligned} \tag{4.19}$$

with the brackets $\langle ... \rangle$ referring to the space-time averaged expectation values according to

$$\langle f(x) \rangle = \frac{\int d^4x\, f(x)\, S(x, K)}{\int d^4x\, S(x, K)}. \tag{4.20}$$

Thus, $\bar{x}(\vec{K})$ refers to the spacetime "center" of the source, i.e. the point of maximum probability of emission with momentum $\vec{K}$, and $\tilde{x}$ is the offset from the center.

Combining Eqs. 4.18 and 4.10, the correlation function becomes

$$C(\vec{q},\vec{K}) = 1 + \exp\left[-q^{\mu}q^{\nu}\langle\tilde{x}_{\mu}\tilde{x}_{\nu}\rangle(\vec{K})\right]. \tag{4.21}$$

Thus, the Gaussian approximation of the source function leads to a Gaussian form of the correlation function, where the widths of the correlation function are related to the rms widths of the source function. Then, one can use the mass constaint of Eq. 4.11 to eliminate one of the q components in the correlator. The common way to do so is by using the *Cartesian parametrization* [116, 117], where we write the correlation function as

$$C(\vec{q},\vec{K}) = 1 + \exp\left(-\sum_{i,j=o,s,l} R_{ij}^2(\vec{K})\, q_i q_j\right), \tag{4.22}$$

$$R_{ij}^2(\vec{K}) = \langle(\tilde{x}_i - \beta_i\tilde{t})(\tilde{x}_j - \beta_j\tilde{t})\rangle, \quad i,j = o,s,l\,. \tag{4.23}$$

The Gaussian width parameters R_{ij}, also known as *femtoscopic radii* or (historically) *HBT radii*, are 6 functions of three variables: the pair average longitudinal momentum K_z, the length of the pair average transverse momentum $|\vec{K}_{\mathrm{T}}|$, and the angle ϕ of $\vec{K}_{\mathrm{T}}$ with respect to the collision impact parameter. As you can see from Eq. 4.23, these radii are a non-trivial mixture of the spatial and temporal characteristics of the source. The o,s,l in Eq. 4.23 refer to the commonly used *out-side-long* coordinate system (see Fig. 4.3), where

$$\hat{out} = \hat{\vec{K}}_{\mathrm{T}}\,, \quad \hat{long} = \hat{z}\ (\text{i.e. beam})\,, \quad \hat{side} = \hat{long} \times \hat{out}\,. \tag{4.24}$$

A convenient frame to work in is the **L**ongitudinally **C**o-**M**oving **S**ystem (LCMS), in which the pair longitudinal momentum $P_z = 0$. This causes one of the variable dependences of the radii to drop out, i.e. $R_{ij}^2(\vec{K}) \to R_{ij}^2(|\vec{K}_{\mathrm{T}}|,\phi)$. It also imparts a reflection symmetry around $z \to -z$; thus, for analyses at mid-rapidity, the crossterms R_{ol}^2 and R_{sl}^2 vanish. Also, in azimuthally-symmetric collisions, the $x_s \to -x_s$ symmetry leads to $R_{os}^2 = R_{sl}^2 = 0$ as well as dropping the ϕ-dependence of the remaining radii. Thus, in many analyses, including the work presented in this thesis, the quantum statistical correlation function takes the simple form

$$C(\vec{q},|\vec{K}_{\mathrm{T}}|) = 1 + \exp\left[-R_o^2 q_o^2 - R_s^2 q_s^2 - R_l^2 q_l^2\right]. \tag{4.25}$$

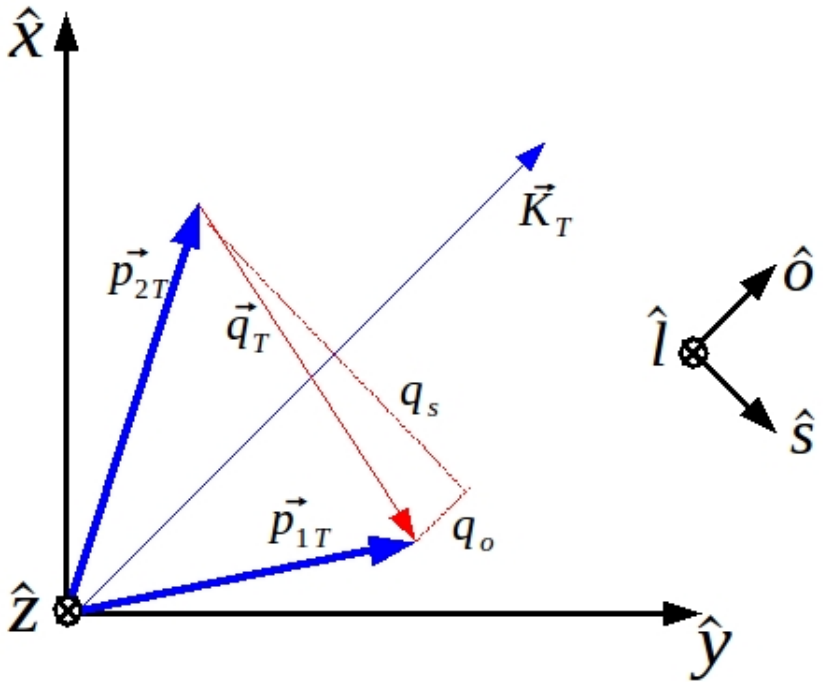

Figure 4.3: The out-side-long coordinate system.

This expression shows us the usual theoretical correlation function used in (azimuthally-integrated) experimental femtoscopic analyses. One can simply fit this expression to the experimentally-measured correlation function and extract the three radii, which are related to the Gaussian variances as

$$\begin{aligned} R_o^2 &= \langle \tilde{x}_o^2 \rangle - 2\beta_{\mathrm{T}} \langle \tilde{x}_o \tilde{t} \rangle + \beta_{\mathrm{T}}^2 \langle \tilde{t}^2 \rangle \\ R_s^2 &= \langle \tilde{x}_s^2 \rangle \\ R_l^2 &= \langle \tilde{x}_l^2 \rangle \,. \end{aligned} \tag{4.26}$$

4.2.4 Lambda parameter

An additional parameter often included in femtoscopic correlation functions is the *lambda parameter*. It is usually included in the correlation function as

$$C(\vec{q}, \vec{K}) = 1 - \lambda + \lambda K_{\mathrm{FSI}} \left(1 + \exp\left[-R_o^2 q_o^2 - R_s^2 q_s^2 - R_l^2 q_l^2\right]\right) . \tag{4.27}$$

λ measures the deviation of the correlation function from its expected theoretical value at $q = 0$. The bosonic femtoscopic correlation function (for no FSI[10]) will reach a maximum of 2.0 at $q = 0$ (assuming no higher-order symmetrization); however, several factors can affect the correlation and make $\lambda < 1$. The presence of long-lived resonance decay products will dilute the signal, as their correlation function will have a very large radius and, thus, only contribute at very small relative momentum, which is generally smaller than the experimental momentum resolution. Particles that are produced coherently (e.g. pion condensate [118]) will not have a quantum statistical enhancement and will also dilute the signal; a recent analysis suggests that the coherent contribution to pion production in central heavy-ion collisions may be as large as 20-30% [119]. The experiment-specific issue of misidentified particles will also lead to a diluted signal.

4.2.5 Experimental correlation function

The expressions for the theoretical correlation function seen above will eventually be compared to the experimental correlation function, which is defined as

$$C_{\vec{K}_{\mathrm{T}}}(\vec{q}) = \frac{A_{\vec{K}_{\mathrm{T}}}(\vec{q})}{B_{\vec{K}_{\mathrm{T}}}(\vec{q})} \tag{4.28}$$

where $A_{\vec{K}_{\mathrm{T}}}(\vec{q})$ is a relative momentum distribution built from pairs taken from the same event, and $B_{\vec{K}_{\mathrm{T}}}(\vec{q})$ is a similar distribution of pairs from different events. The process of dividing by mixed-event pairs allows us to remove the combinatoric phase-space background and retain the desired femtoscopic correlation, since the mixed-event pairs will have no physical correlation. This also allows us to remove detector-specific effects on the single-particle distributions. To account for the $\vec{K}_{\mathrm{T}}$ dependence of the radii, the correlation functions are formed in separate $\vec{K}_{\mathrm{T}}$ bins, and then the $\vec{K}_{\mathrm{T}}$ (or $\vec{M}_{\mathrm{T}}$) distributions of the extracted radii can be studied.

[10]The λ parameter also measures the deviation of the correlation function from its expected theoretical value at $q = 0$ with the inclusion of the FSI factor; however, the expected intercept may or may not be 2.0 depending on the effect of the FSI.

4.3 Extracting source information from radius parameters

In this section, we will look at the different characteristics of the source function that are extracted via the femtoscopic radii.

4.3.1 Source size and dynamics

We can study the interpretations of the extracted femtoscopic radii and their relation to the dynamics of the source by using a hydrodynamically-expanding Gaussian source model[11] ([101] and references within; see footnote below for parameter explanations)

$$S(x,K) = \frac{M_{\mathrm{T}}\,\cosh(\eta - Y)}{8\pi^4 \Delta\tau} \exp\left[-\frac{K\cdot u(x)}{T(x)} - \frac{(\tau-\tau_0)^2}{2(\Delta\tau)^2} - \frac{r^2}{2R^2(\eta)} - \frac{(\eta-\eta_0)^2}{2(\Delta\eta)^2}\right]. \quad (4.29)$$

Integrating this source function in Eq. 4.10 at pair mid-rapidity, one can write the radii from Eqs. 4.26 as

$$\begin{aligned} R_o^2 &= R_*^2 + \beta_{\mathrm{T}}^2 (\Delta t_*)^2 \\ R_s^2 &= R_*^2 \\ R_l^2 &= L_*^2 \end{aligned} \quad (4.30)$$

where

$$\begin{aligned} \frac{1}{R_*^2} &= \frac{1}{R^2} + \frac{1}{R_{\mathrm{flow}}^2} \\ (\Delta t_*)^2 &= (\Delta\tau)^2 + 2\left(\sqrt{\tau_0^2 + L_*^2} - \tau_0\right)^2 \\ \frac{1}{L_*^2} &= \frac{1}{(\tau_0\Delta\eta)^2} + \frac{1}{L_{\mathrm{flow}}^2} \\ R_{\mathrm{flow}}(M_{\mathrm{T}}) &= \frac{R}{\eta_{\mathrm{f}}}\sqrt{\frac{T}{M_{\mathrm{T}}}} = \frac{1}{\partial\eta_{\mathrm{T}}(r)/\partial r} \\ L_{\mathrm{flow}}(M_{\mathrm{T}}) &= \tau_0\sqrt{\frac{T}{M_{\mathrm{T}}}} = \frac{1}{\partial\cdot u_l}\sqrt{\frac{T}{M_{\mathrm{T}}}}. \end{aligned} \quad (4.31)$$

Here, η_{f} characterizes the transverse flow rapidity profile, $\eta_{\mathrm{T}} = \eta_{\mathrm{f}}(r/R)$.

[11] Here, the space-time coordinates are parametrized by the transverse radius $r^2 = x^2 + y^2$, the space-time rapidity $\eta = \frac{1}{2}\ln[(t+z)/(t-z)]$, and $\tau = (t^2 - z^2)^{1/2}$. The pair momentum $\vec{K}$ is parametrized by $Y = \frac{1}{2}\ln[(E_K + K_{\mathrm{L}})/(E_K - K_{\mathrm{L}})]$ and $M_{\mathrm{T}} = (m^2 + K_{\mathrm{T}}^2)^{1/2}$. $\sqrt{2}R$ is the transverse rms radius of the source. τ_0 is the average freeze-out proper time and $\Delta\tau$ is the mean duration of particle emission. The Boltzmann factor $\exp[-K\cdot u(x)/T(x)]$ describes the momentum-space structure of the source controlled by a collective component given by the flow velocity field $u^\mu(x)$ and a thermal component characterized by the slope parameter, i.e. effective temperature, $T(x)$.

We see that, in the absence of flow, the sideward radius equals the geometric transverse size of the source, while the outward radius has an additional component coming from the emission duration. The ratio R_o/R_s is often studied to extract information about the emission duration, though the exact relationship is non-trivial. It was originally expected that the formation of a QGP would lead to an extended emission period and thus an increase in both the outward radius and the R_o/R_s ratio. In fact, this was one of the main QGP "signals" expected for femtoscopic analyses. However, experiments at RHIC and ALICE both see this ratio consistent with unity [120]. Several factors, including the $x-t$ correlations seen in Eq. 4.26, can have contributions here, and this "HBT puzzle" has yet to be fully resolved [100, 121].

The longitudinal radius is sensitive to the time parameter τ_0, the average freeze-out proper time. For a boost invariant source with weak tranverse expansion, one can calculate the relation [117, 122]

$$R_l^2 = \tau_0^2 \frac{T}{M_\mathrm{T}} \frac{K_2(M_\mathrm{T}/T)}{K_1(M_\mathrm{T}/T)} \,, \tag{4.32}$$

where $K_{1,2}$ are Bessel functions, and T is a common freeze-out temperature. This has been used by experimental analyses to extract the average freeze-out proper time for pions in heavy-ion collisions at various collision energies [120].

From the expressions (4.30) and (4.31), we see two main instances of parameter interplay that dictate the value of the extracted radii: thermal smearing vs. flow gradients, and geometric size (R and $\tau\Delta\eta$) vs. "dynamical lengths" (R_flow and L_flow). The first interplay is apparent in the factor $\sqrt{T/M_\mathrm{T}}$; high temperatures, i.e. broader momentum spectra, tend to increase the regions of homogeneity, while large flow contributions cause these regions to shrink (as discussed in Fig. 4.2). The second interplay is a tradeoff between geometric and dynamical sizes, where the smaller of the two "dominates"; the larger the size, the less it contributes to the "radii" R_* and L_* in Eq. 4.31.

From these equations, both transverse and longitudinal source sizes have an approximate $M_\mathrm{T}^{-1/2}$ dependence. The exponent in the M_T dependence of the radii can be shown analytically to be $-\frac{1}{2}$ for a one-dimensional longitudinal hydrodynamic expansion with

negligible transverse flow and common freeze-out characteristics, regardless of particle species [122, 123]. This leads to the idea of "universal M_{T}-scaling" for different particle species, which is often searched for in femtoscopic analyses. However, it is unclear exactly how this picture changes when one includes significant transverse flow, viscosity corrections, and hadronic rescatterings, all of which are important in LHC Pb-Pb collisions. A recent model using 3D+1 hydrodynamics (with statistical hadronization and resonance decays, but no hadronic rescatterings) [124] finds different values of the M_{T} exponent for the different *out-side-long* radii and for different particle species when each is fit separately; though, they also find that a common scaling can be found to within 10-20% for pions, kaons, and protons when fit together, with values of the exponent between -0.40 and -0.70. Another recent study [125], which includes hadronic rescattering, predicts no common scaling between pions and kaons at LHC energies. Their results also predict that the inclusion or exclusion of initial transverse flow does not significantly affect the kaon data, suggesting that it is the effects of final-state hadronic rescattering that can drive different species to exhibit different freeze-out characteristics.

4.3.2 Additional femtoscopic considerations

The work in this thesis uses the approximations and the forms of the correlation functions used above, i.e. Eq. 4.25, as well as the simplified 1D form seen in the next paragraph. The remaining paragraphs will briefly discuss other aspects of the source function or wavefunction one can study with femtoscopic correlations.

1D femtoscopy

A simplification of the correlation function can be employed by assuming a spherical Gaussian source function with a single width parameter R_{inv} (read "R invariant")

$$S_{\vec{K}}(\vec{r}') \sim \exp\left(-\frac{r'^2}{4R_{\mathrm{inv}}^2}\right) \tag{4.33}$$

The correlation function is then studied as the function of a single variable $q_{\mathrm{inv}} \equiv \sqrt{-q_\mu q^\mu}$ (read "q invariant") and takes the form of a one-dimensional Gaussian,

$$C(q_{\text{inv}}) = 1 + \exp(-q_{\text{inv}}^2 R_{\text{inv}}^2) \ . \tag{4.34}$$

This simplified form is generally used for analyses with low statistics, e.g. heavier particles or lower collision energies. This thesis will show R_{inv} and 1D λ in addition to the three-dimensional results.

Azimuthally-sensitive femtoscopy

If one studies collisions that do not have azimuthal symmetry, e.g. heavy-ion collisions at peripheral centralities, one no longer has the $x_s \to -x_s$ symmetry, and the *out-side* cross-term cannot be ignored. The correlation function then takes the form

$$C(\vec{q}, \vec{K}_{\text{T}}) = 1 + \exp\left[-R_o^2 q_o^2 - R_s^2 q_s^2 - R_l^2 q_l^2 - 2R_{ol}^2 q_o q_l\right] \ . \tag{4.35}$$

Azimuthally-differential femtoscopy is performed in ϕ bins measuring the angle of $\vec{K}_{\text{T}}$ with respect to the impact parameter or, experimentally, the second-order flow plane. The anisotropic shape of the collision region in the transverse plane gives rise to oscillations of the extracted transverse radii parameters with respect to the viewing angle ϕ. These oscillations can be used to measure the source freeze-out eccentricity, and comparisons to the centrality-specified initial-state eccentricity can illuminate the dynamics of the transverse expansion of the collision region [126]. Fig. 4.4 shows azimuthally-sensitive femtoscopy results from ALICE, showing the oscillations in R_o^2, R_s^2, and R_{os}^2.

Non-identical femtoscopy

Femtoscopic analyses can also be done with pairs of non-identical particles. These pairs will not have a Bose-Einstein enhancement (or Fermi-Dirac repulsion); however, the final-state interactions between the particles can still be used to extract information about their emission processes via Eq. 4.14. Not only can these correlations study the size and shape of the emission region, but they can also measure the *relative emission shifts* between different species, i.e. whether different species freeze-out closer to or farther from the center of the collision, which is not possible with pairs of identical particles. This shift is related to

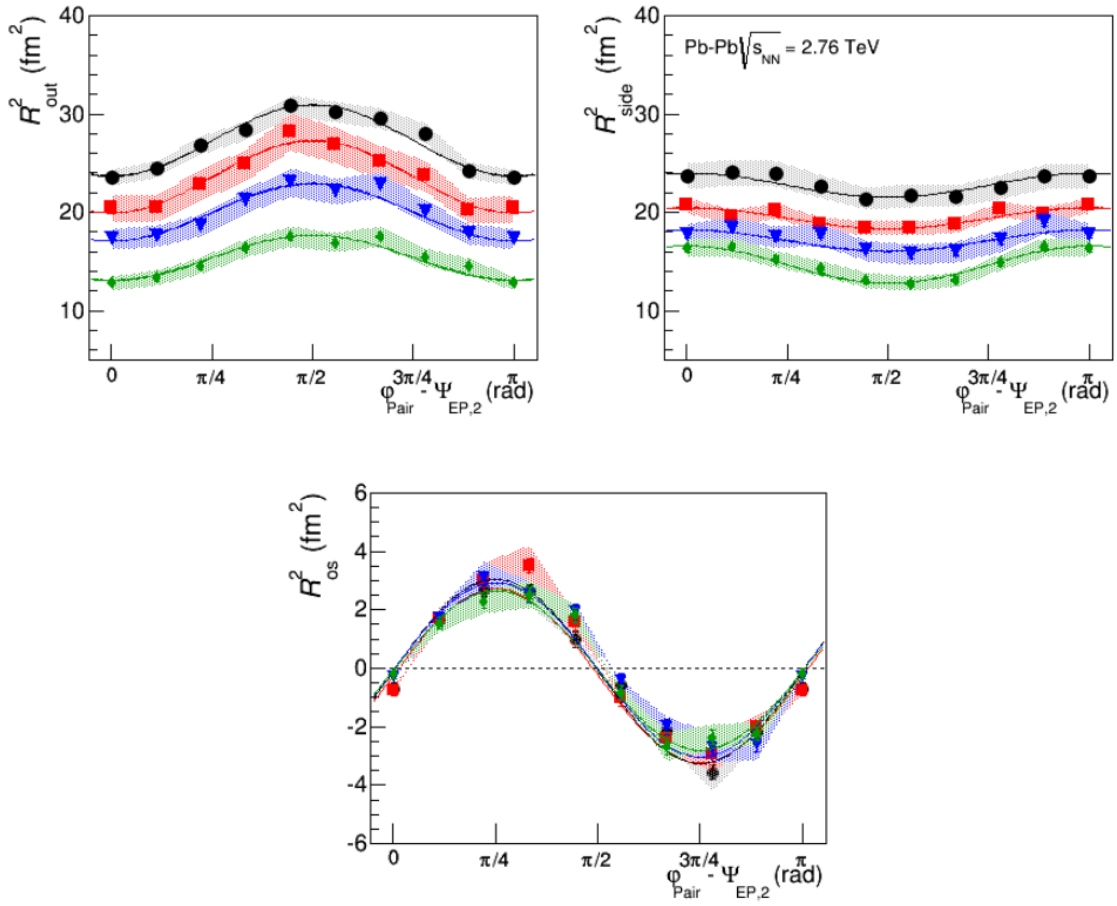

Figure 4.4: ALICE results [127] of azimuthally-sensitive femtoscopy, showing the oscillations of R_o^2, R_s^2, and the cross-term R_{os}^2. The different colors refer to different K_{T} bins (black/low $\rightarrow$ green/high).

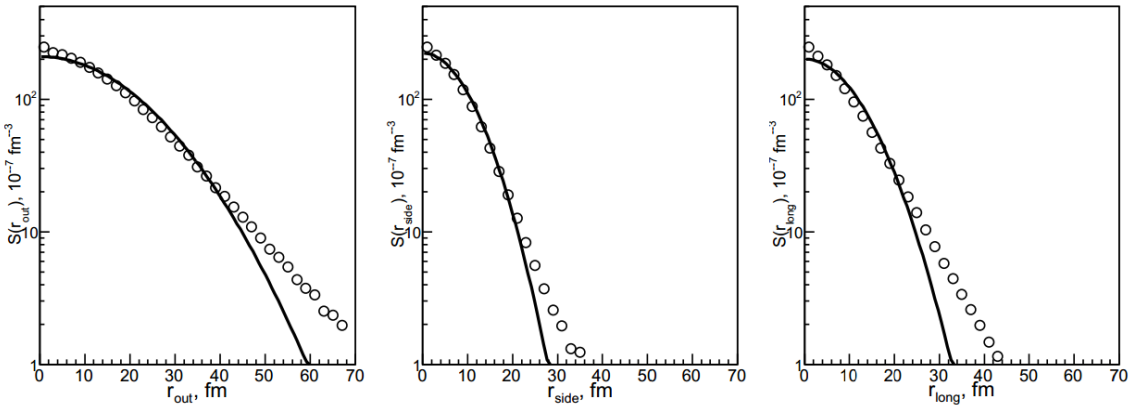

Figure 4.5: Pion source function projections using the imaging technique from HKM correlations [130] for Pb-Pb collisions at $\sqrt{s_{\rm NN}} = 2.76$ TeV. Solid lines represent Gaussian fits.

the collective behavior of the matter, i.e. flow, and is a consequence of x-p correlations. Hydrodynamic calculations predict that lighter particles will, on average, freeze-out closer to the center of the source [128].

Source imaging

Rather than inserting a model-dependent ansatz for the source function in order to extract information about the source, one can invert the Fourier transform in Eq. 4.12 as

$$S_{\vec{K}}(\vec{r}) \approx \int d^3\vec{q}\, \cos(\vec{q}\cdot\vec{r})\, (C_{\vec{K}}(\vec{q}) - 1)\ . \tag{4.36}$$

This process is known as *source imaging* [129]. Using this method, one can build the shape of the source function without any *a priori* assumptions. Fig. 4.5 shows the results of imaging predictions from the HKM model [130]. An interesting thing to note is the distinct non-Gaussian tails of the source function, especially considering that the majority of non-imaging femtoscopic analyses assume a Gaussian source.

Extracting interaction parameters

In the same way that one assumes knowledge of the pair interaction (i.e. wavefunction) and extracts the unknown source function parameters, one can instead assume knowledge of

the source function and extract information about the interaction parameters. For certain systems, such as $p\Lambda$ or $\Lambda\Lambda$ (and similar pairs using anti-particles), where the strong interaction parameters are not well known, it is possible to use better understood correlations such as pp and $p\bar{p}$ to predict source sizes and make some assumptions about the interaction parameters, which can then be used in the correlation functions of the poorly understood systems. Ref. [131] studies baryonic systems and attempts to gain information about their strong interaction potentials using STAR data. ALICE currently has an ongoing $\Lambda\Lambda$ / $\Lambda\bar{\Lambda}$ analysis that will look to other femtoscopic analyses in this manner.

Multi-particle correlations: Coherence

The above formalism for femtoscopic correlations generally assumes that the particles are emitted chaotically with no contribution from partially coherent sources, such as a pion condensate [118], whose presence would suppress the correlation. Three-particle and higher-order femtoscopic correlations are increasingly sensitive to the suppression from coherence and can be used to access the fraction of coherent pairs in the sample [132]. ALICE has performed a three-pion analysis and has measured correlations consistent with a coherent fraction of $\approx$ 20-30% [119].

Chapter 5
Neutral kaon femtoscopy

Neutral kaon femtoscopy acts as a wonderful complement to other femtoscopic analyses. Pion and charged kaon analyses are more common because of the increased statistics; however, these analyses have some problematic issues which the neutral kaons can avoid. Pion femtoscopy is affected significantly by resonance decays. The pions coming from long-lived resonances will essentially not contribute to the correlation (or contribute only a very narrow enhancement) and dilute the signal, while pions coming from semi-long-lived decays can extend the source size and introduce a non-Gaussian distortion to the correlation. Kaons suffer less from resonance decays, simply due to their heavier masses, and present a clearer signal. Charged-particle analyses also must deal with the Coulomb interaction, which is significant at low q, precisely the region where femtoscopic correlations are important; neutral kaons, of course, do not interact via Coulomb. Charged kaon tracks can only be confidently identified for $p_{\mathrm{T}} < 0.5$ without TOF and for $p_{\mathrm{T}} < 1.5$ with TOF. Neutral kaon identification, which utilizes topological features of the decay geometry, is excellent even at high momentum, allowing us to extend femtoscopic studies to higher momentum than other species. Lastly, charged and neutral kaon analyses act as a convenient consistency check for each other because they are expected to have the same results while using significantly different analysis methods, e.g. charged-particle tracking vs. secondary vertex reconstruction and Coulomb vs. strong FSI.

In this chapter, we will discuss the theoretical aspects of the neutral kaon system. We will look at the interesting two-particle wavefunction, which includes contributions from

quantum statistics and strong final-state interactions, and build the theoretical correlation function that is necessary to fit the experimental data.

Much of this chapter follows the work of Lednický and Lyuboshitz regarding final-state interactions [133] and the more recent work of Lednický and Bekele regarding the $K^0_S K^0_S$ system [134].

5.1 The neutral kaon

The neutral kaon states K^0 and $\bar{K}^0$ carry definite strangeness $+1$ and -1, respectively, and thus are strong interaction eigenstates. In the quark model,

$$|K^0\rangle = |d\bar{s}\rangle \quad \text{and} \quad |\bar{K}^0\rangle = |s\bar{d}\rangle\,. \tag{5.1}$$

The neutral kaon mass is $m_{K^0} = 497.6$ MeV/c^2, which is slightly bigger than the charged kaon mass due to the u-d quark mass difference. They are related under CP transformation as [12]

$$CP\,|K^0\rangle = |\bar{K}^0\rangle\,, \quad CP\,|\bar{K}^0\rangle = |K^0\rangle\,. \tag{5.2}$$

Since these are the strong interaction eigenstates, these are the particles that are produced in heavy-ion collisions.

Due to weak charged current interactions, $K^0 - \bar{K}^0$ mixing [135] occurs (see Fig. 5.1), and the physical mass eigenstates and CP eigenstates are given by

$$|K^0_1\rangle = \frac{K^0 + \bar{K}^0}{\sqrt{2}} \quad \text{and} \quad |K^0_2\rangle = \frac{K^0 - \bar{K}^0}{\sqrt{2}}\,, \tag{5.3}$$

with CP eigenvalues of $+1$ and -1, respectively. Assuming CP is conserved in weak interactions, K^0_1 can only decay into a state with $CP = +1$, e.g. $\pi^+\pi^-$ or $\pi^0\pi^0$, and K^0_2 must go to $\pi^+\pi^-\pi^0$ or $\pi^0\pi^0\pi^0$.[13] Since the decay phase space is much larger for 2π than for 3π, K^0_1 has a much shorter lifetime than K^0_2; hence, K^0_1 and K^0_2 are usually called K^0_S (**S**hort)

[12] The CP transformation is actually, in the $|K^0\rangle$, $|\bar{K}^0\rangle$ basis, $\left(\begin{smallmatrix} 0 & \eta \\ \eta^* & 0 \end{smallmatrix}\right)$, where η is a phase. We express the freedom to choose $\eta = 1$.

[13] $K^0_1 \to \pi^+\pi^-\pi^0$ is only forbidden due to CP conservation for certain isospin values, but the allowed isospin value decays are greatly suppressed due to orbital angular momentum considerations.

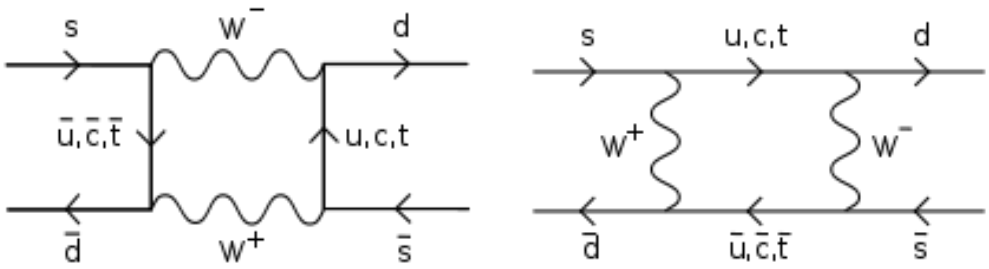

Figure 5.1: Second-order weak interaction Feynman diagrams showing $K^0 - \bar{K}^0$ mixing.

and K^0_{L} (**L**ong). The idea of different lifetimes for neutral kaons was first predicted by Gell-Mann and Pais [135]. The experimentally measured proper lifetimes of the K^0_{S} and K^0_{L} are 0.90×10^{-10} s and 5.12×10^{-8} s, which correspond to decay lengths of 2.7 cm and 15.3 m. This is one of the reasons why K^0_{S} is the preferred neutral kaon for high-energy experiments, as the K^0_{L} will often escape the detector before decaying.[14] An interesting note about the role of neutral kaons in particle physics history is that the observation of $K^0_{\mathrm{L}} \to 2\pi$ decays established the first observation of CP violation [136]. Table 5.1 shows the principal branching ratios for neutral kaon decays.

5.2 Two-particle state

5.2.1 Bose-Einstein enhancement

For neutral kaon femtoscopic correlations, we are interested in the two-particle $K^0_{\mathrm{S}}K^0_{\mathrm{S}}$ wavefunction. From Eq. 5.3, we get

$$|K^0_{\mathrm{S}}K^0_{\mathrm{S}}\rangle = \frac{1}{2}\left(|K^0K^0\rangle + |K^0\bar{K}^0\rangle + |\bar{K}^0K^0\rangle + |\bar{K}^0\bar{K}^0\rangle\right) . \tag{5.4}$$

The two-K^0_{S} state is made up of a combination of K^0K^0 ($\bar{K}^0\bar{K}^0$) and $K^0\bar{K}^0$ states. Since the K^0K^0 and $\bar{K}^0\bar{K}^0$ states are pairs of identical bosons, they will produce a Bose-Einstein enhancement due to a symmetrized wavefunction. For the mixed $K^0\bar{K}^0$ terms, one can show that even though they are not identical bosons, they will produce a Bose-Einstein-like

[14] Also, π^0 is harder to detect than charged pions; hence, the K^0_{S} are only reconstructed via their charged pion decay channel.

K^0_S	$\rightarrow$	$\pi^+\pi^-$	69.2%	
	$\rightarrow$	$\pi^0\pi^0$	30.7%	
	$\rightarrow$	$\pi^\pm e^\mp \nu_e$	7.0×10^{-4}	
	$\rightarrow$	$\pi^\pm \mu^\mp \nu_\mu$	4.7×10^{-4}	
	$\rightarrow$	$\pi^+\pi^-\pi^0$	3.5×10^{-7}	non-CP-violating
	$\rightarrow$	$\pi^+\pi^-\pi^0$	not given	CP-violating
	$\rightarrow$	$3\pi^0$	$< 1.2 \times 10^-7$ (90% C.L.)	CP-violating
K^0_L	$\rightarrow$	$\pi^\pm e^\mp \nu_e$	40.5%	
	$\rightarrow$	$\pi^\pm \mu^\mp \nu_\mu$	27.0%	
	$\rightarrow$	$3\pi^0$	19.6%	
	$\rightarrow$	$\pi^+\pi^-\pi^0$	12.6%	
	$\rightarrow$	$\pi^+\pi^-$	2.0×10^{-3}	CP-violating
	$\rightarrow$	$\pi^0\pi^0$	8.7×10^{-4}	CP-violating

Table 5.1: Principal branching ratios for neutral kaon decays [137].

enhancement at low $\vec{q}$. In general, a boson–anti-boson pair ($B\bar{B}$) is an eigenstate of the charge conjugation operator. We can write the probability amplitude for a given charge conjugation eigenvalue C_n as [138]

$$|B\bar{B}\rangle_{C_n=\pm1} = \frac{1}{\sqrt{2}}\left(|B(\vec{p}')\bar{B}(-\vec{p}')\rangle \pm |B(-\vec{p}')\bar{B}(\vec{p}')\rangle\right) \ , \tag{5.5}$$

where $\vec{p}'$ is the momentum in the PRF. As $\vec{q} \rightarrow 0$, i.e. $\vec{p}' \rightarrow 0$,

$$|B\bar{B}\rangle_{C_n=\pm1} \rightarrow \frac{1}{\sqrt{2}}\left(|B(0)\bar{B}(0)\rangle \pm |B(0)\bar{B}(0)\rangle\right) \tag{5.6}$$

which is maximally enhanced for $C_n = +1$ and suppressed for $C_n = -1$. By looking at $K^0_S K^0_S$ pairs, we are explicitly choosing the $C_n = +1$ state. Thus, the whole $K^0_S K^0_S$ system will produce a Bose-Einstein-like enhancement at low $\vec{q}$. It is interesting to note that any spinless boson–anti-boson pair, e.g. K^+K^-, $\pi^+\pi^-$, etc., has this property; however, if one does not select a specific charge eigenvalue, the enhanced and suppressed contributions will cancel each other, and the correlation (excluding FSI) will be flat. The neutral kaon system is special in that it presents an easy way to explicitly select a state with a definite charge eigenvalue.

5.2.2 Strong FSI

(Throughout the rest of this chapter, we will use the variables $\vec{k}^*$ and $\vec{r}^*$ instead of $\vec{p}'$ and $\vec{r}'$ to represent the momentum of a particle and the emission separation of the pair in the pair rest frame, as they are more commonly used in the literature. Also, $k^* = |\vec{k}^*| = \frac{1}{2}q_{\rm PRF} = \frac{1}{2}q_{\rm inv}$.)

Strong final-state interactions have an important effect on $K^0_{\rm S}K^0_{\rm S}$ correlations. Particularly, the $K^0\bar{K}^0$ channel is affected by the near-threshold resonances $f_0(980)$ and $a_0(980)$. Using an equal emission-time approximation in the pair rest frame[15], the elastic $K^0\bar{K}^0$ transition is written as a stationary solution $\Psi^{(+)}_{-\vec{k}^*}(\vec{r}^*)$ of the scattering problem in the PRF (the $-\vec{k}^*$ subscript refers to a reversal of time from the emission process), which at large distances has the asymptotic form of the superposition of a plane wave and an outgoing spherical wave,

$$\Psi^{(+)}_{-\vec{k}^*}(\vec{r}^*) = e^{-i\vec{k}^*\cdot\vec{r}^*} + f(k^*)\frac{e^{ik^*r^*}}{r^*} \,, \tag{5.7}$$

where $f(k^*)$ is the s-wave scattering amplitude for a given system. For $K^0\bar{K}^0$, $f(k^*)$ is dominated by the f_0 and a_0 resonances and written in terms of the resonance masses and decay couplings [134, 140]:

$$f(k^*) = \frac{1}{2}[f_0(k^*) + f_1(k^*)] \,, \tag{5.8}$$

$$f_{\rm I}(k^*) = \frac{\gamma_{\rm r}}{m_{\rm r}^2 - s - i\gamma_{\rm r}k^* - i\gamma'_{\rm r}k'_{\rm r}} \,. \tag{5.9}$$

Here, $s = 4(m_K^2 + k^{*2})$; $\gamma_{\rm r}(\gamma'_{\rm r})$ refers to the couplings of the resonances to the $f_0 \to K^0\bar{K}^0(f_0 \to \pi\pi)$ and $a_0 \to K^0\bar{K}^0(a_0 \to \pi\eta)$ channels; $m_{\rm r}$ is the resonance mass; and $k'_{\rm r}$ refers to the momentum in the PRF for the second decay channel ($f_0 \to \pi\pi$ or $a_0 \to \pi\eta$) with the corresponding partial width $\Gamma'_{\rm r} = \gamma'_{\rm r}k'_{\rm r}/m_{\rm r}$. The amplitudes f_I of isospin $I = 0$ and $I = 1$ refer to the f_0 and a_0, respectively. The parameters associated with the resonances and their decays are taken from several experiments, and the values are listed in Table 5.2.

In general, Eq. 5.7 can be used for any two-particle FSI interaction. For K^0K^0 or

[15]The approximation is justified for heavy-mass particles such as the kaon and will only lead to a slight overestimation of the FSI effect for pions [139].

Ref	m_{f_0}	$\gamma_{f_0 K\bar{K}}$	$\gamma_{f_0\pi\pi}$	m_{a_0}	$\gamma_{a_0 K\bar{K}}$	$\gamma_{a_0\pi\eta}$
[141]	0.973	2.763	0.5283	0.985	0.4038	0.3711
[142]	0.996	1.305	0.2684	0.992	0.5555	0.4401
[143]	0.996	1.305	0.2684	1.003	0.8365	0.4580
[140]	0.978	0.792	0.1990	0.974	0.3330	0.2220

Table 5.2: The $f_0(980)$ and $a_0(980)$ masses and coupling parameters from various experiments, all in GeV.

$\bar{K}^0\bar{K}^0$, the s-wave scattering amplitude $f(k^*)$ is small, i.e. ~ 0.1 fm, and can be neglected; this is the same for the non-resonant s-wave contributions for $K^0\bar{K}^0$ [144]. However, the FSI contributions to $K^0\bar{K}^0$ due to the f_0 and a_0 have non-negligible scattering amplitudes ~ 1.0 fm and must be accounted for.

5.3 $K^0_S K^0_S$ correlation function

To build the full $K^0_S K^0_S$ correlation function, we combine the average squares of the symmetrized K^0K^0 and $\bar{K}^0\bar{K}^0$ wavefunctions and the non-symmetrized $K^0\bar{K}^0$ wavefunction and integrate over the source function. Here, we will use the Lednický and Lyuboshitz analytical model to perform the integration [133]. The model assumes a one-dimensional Gaussian source function of the PRF relative distance $|\vec{r}^*|$ with a Gaussian width R of the form

$$S(|\vec{r}^*|) \sim e^{-|\vec{r}^*|^2/(4R^2)} \ . \tag{5.10}$$

For K^0K^0 and $\bar{K}^0\bar{K}^0$, neglecting the small FSI contribution, the wave function reduces to the symmetrized plane wave

$$\Psi_{K^0K^0}(\vec{r}^*) = \frac{1}{\sqrt{2}}\left[e^{-i\vec{k}^*\cdot\vec{r}^*} + e^{+i\vec{k}^*\cdot\vec{r}^*}\right] \ . \tag{5.11}$$

This simple integration gives the expected Gaussian form for the correlation function from Eq. 4.34. Combining the K^0K^0, $\bar{K}^0\bar{K}^0$, and $K^0\bar{K}^0$ contributions with the proper $K^0_S K^0_S$ weight fractions[16] and using the Lednický and Lyuboshitz model to perform the averaging

[16]To be rigorous, one should replace the 1/2 factor in front of the FSI contributions in Eq. 5.12 with $\alpha = (1-\epsilon^2)/2$, where ϵ is the $K^0 - \bar{K}^0$ abundance asymmetry. However, in heavy-ion collisions at high energies, this asymmetry is basically zero [23](see Fig. 5.2), and $\alpha \approx 0.5$, meaning 1/2 of the pairs will

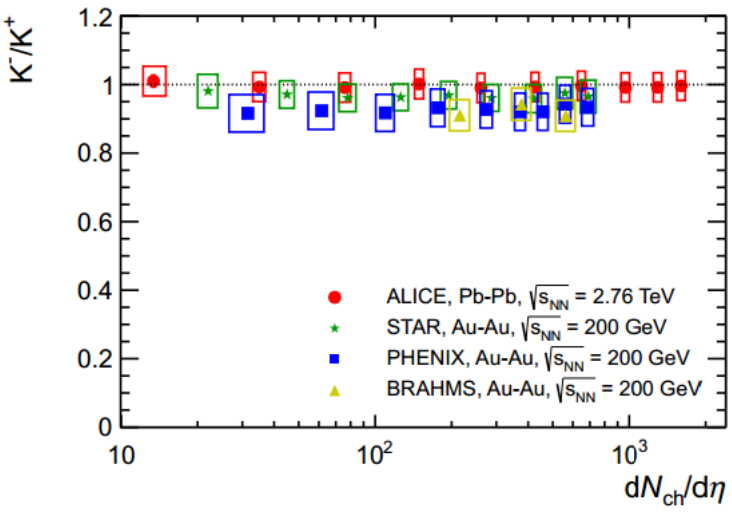

Figure 5.2: K^-/K^+ asymmetry results from ALICE [23], suggesting the lack of $K^0/\bar{K}^0$ asymmetry.

over $\vec{r}^*$, we get

$$C(q) = 1 + e^{-q^2R^2} + \frac{1}{2}\left[\left|\frac{f(k^*)}{R}\right|^2 + \frac{4\mathcal{R}f(k^*)}{\sqrt{\pi}R}F_1(qR) - \frac{2\mathcal{I}f(k^*)}{R}F_2(qR)\right] , \tag{5.12}$$

where

$$F_1(z) = \int_0^z dx \frac{e^{x^2-z^2}}{z} \quad \text{and} \quad F_2(z) = \frac{1-e^{-z^2}}{z} . \tag{5.13}$$

Here, $q = q_{\text{PRF}} = q_{\text{inv}}$ from Eq. 4.34 and R is R_{inv} from Eq. 4.33.

Figures 5.3 to 5.5 show examples of the different contributions to the $K^0_S K^0_S$ correlation function for various source sizes R_{inv}. Fig. 5.3 shows the Bose-Einstein contribution, i.e. the Gaussian found in Eq. 4.34. Note that the enhancement gets wider for smaller source sizes, as expected from a Fourier transform. Fig. 5.4 shows the contribution from the final-state interactions (including the corrections of Sec. 5.3.1 and Appendix A). We see that the effect of the $K^0\bar{K}^0$ interaction is repulsive in character, similar to an annihilation process. Again, the structure gets wider for smaller source sizes; the depression also gets deeper for smaller R.

Fig. 5.5 shows the complete $K^0_S K^0_S$ correlation function including Bose-Einstein effects

undergo significant FSI.

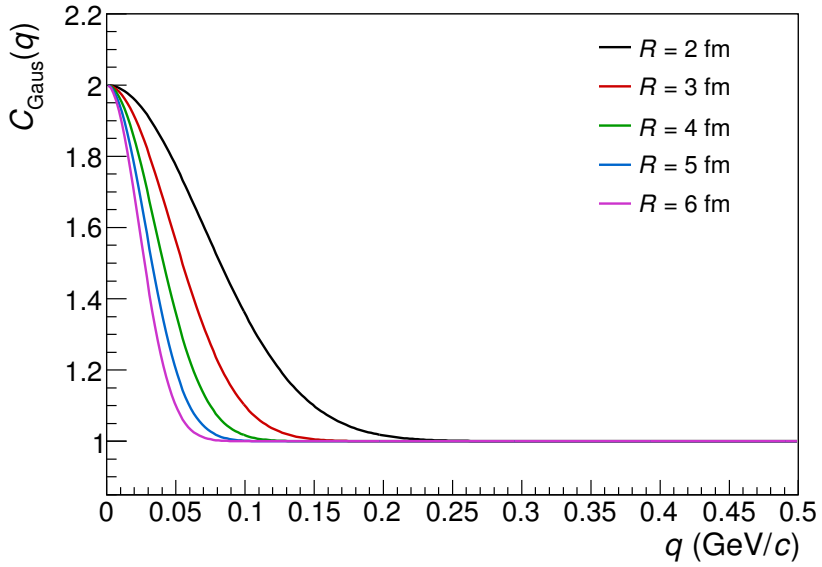

Figure 5.3: Bose-Einstein contribution to the $K^0_{\text{S}}K^0_{\text{S}}$ correlation function for various radii.

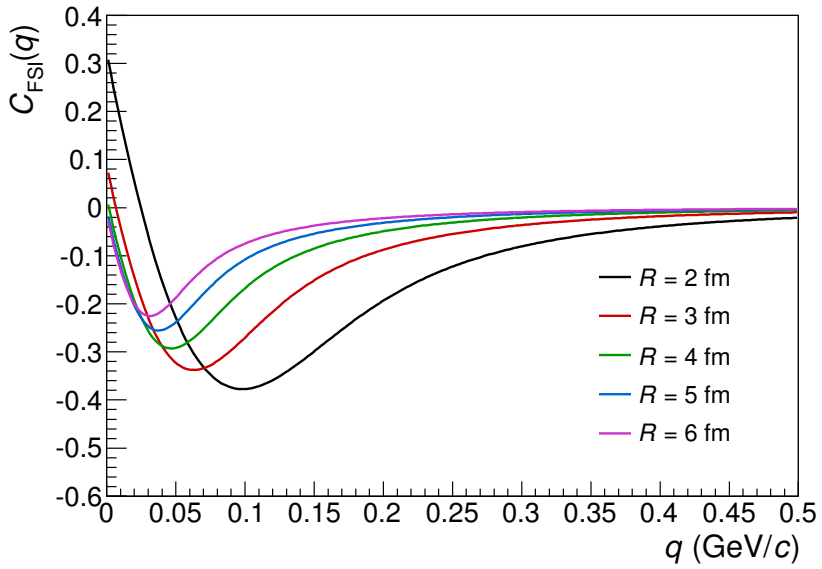

Figure 5.4: Final-state interaction contribution to the $K^0_{\text{S}}K^0_{\text{S}}$ correlation function for various radii.

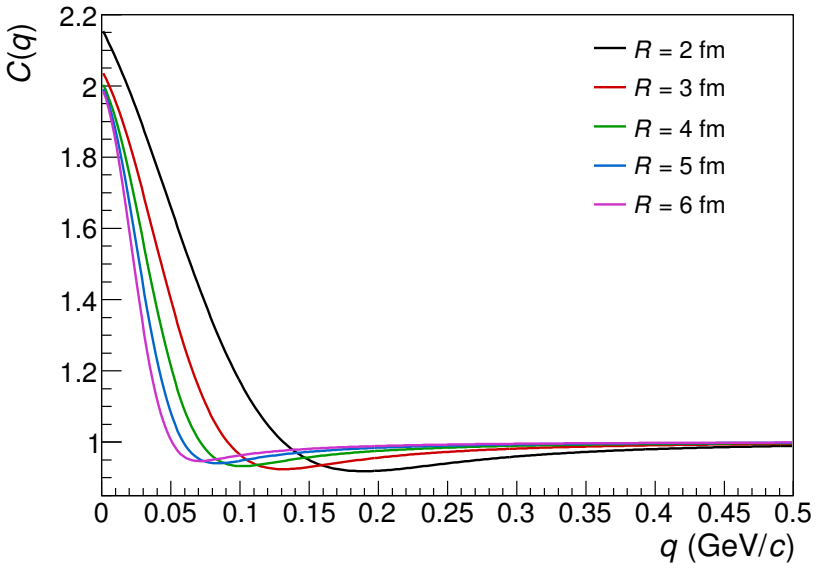

Figure 5.5: 1D $K^0_S K^0_S$ correlation function for various radii, including contributions from quantum statistics and final-state interactions. The FSI include the corrections discussed in Appendix A.

and final-state interactions according to Eq. 5.12, including the corrections below. One can see that while the Bose-Einstein enhancement is the most significant contribution, the FSI are certainly non-negligible, causing a $\approx 10\%$ depression in the mid-q range. This depression moves out to larger q for smaller radii.

Fig. 5.6 shows the correlation functions for the different sets of resonance parameters seen in Table 5.2, which are used in the FSI scattering amplitudes. Although the parameter values can vary by a significant amount, the dominant part of the scattering amplitude is determined by the ratios of the decay channel couplings, which remain fairly consistent between experiments. Still, there are some non-negligible variations in the correlation functions due to these values, which can lead to systematic differences up to 5% in the radii extracted from fits to the data.

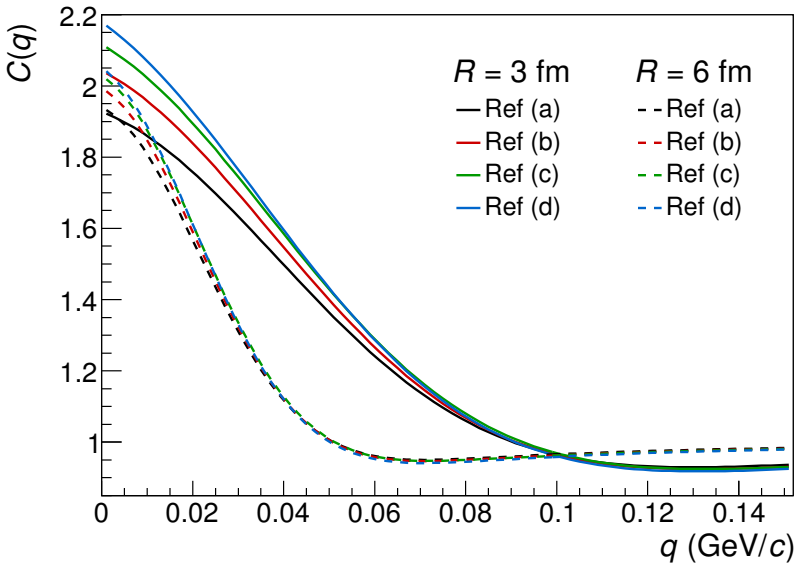

Figure 5.6: 1D $K^0_S K^0_S$ correlation function using different FSI parameters extracted from various experiments: (a) [140], (b) [141], (c) [142], (d) [143].

5.3.1 Corrections to the $K^0_S K^0_S$ correlation function

Included in the plots above are two corrections to the $K^0_S K^0_S$ correlation function. The first correction involves the inclusion of the inelastic transition $K^+K^- \to K^0\bar{K}^0$. The second deals with the deviation of the spherical waves from the true scattered waves in the inner region of the short range potential. Both of these corrections are small for the source sizes probed in high-energy heavy-ion collisions ($R \gtrsim 2$ fm), but can become significant at lower radii. See Appendix A for more details on these corrections.

5.4 Three-dimensional correlation function

The analytical derivation of the $K^0_S K^0_S$ correlation in Eq. 5.12 incorporating FSI done via the Lednický and Lyuboshitz model [133] is specific to the one-dimensional case. For the 3D case, the integration of Eq. 4.14 including the FSI contributions to the wavefunction cannot be performed analytically. In order to form the 3D correlation function, we combine a Monte Carlo emission simulation with a calculation of the two-particle wavefunction, thus perform-

ing a numerical integration of Eq. 4.14. The Monte Carlo emission simulation consists of generating the pair positions sampled from a three-dimensional Gaussian (out-side-long) in the PRF, with three input radii as the width parameters, and generating the particle momenta sampled from a distribution taken from data. Using the MC-sampled positions and momenta, we calculate the equal-time-approximated two-particle PRF wavefunction using Eqs. 5.7 and 5.11. We then build a correlation function using the wavefunction weights to form the signal distribution, and an unweighted distribution acts as a phase-space background:

$$C(\vec{q}) = \frac{\langle |\Psi(\vec{q}, \vec{r}')|^2 \rangle_{S(\vec{r}')}}{\langle 1 \rangle_{S(\vec{r}')}} , \tag{5.14}$$

where $\langle ... \rangle_{S(\vec{r}')}$ refers to the process of sampling many times over the Gaussian source function and momentum distribution. This theoretical correlation function is then used to fit the data. More details on the 3D fitting process can be found in Ch. 6.

5.5 Past $K^0_S K^0_S$ analyses

Neutral kaon femtoscopy has been studied in the past, but only a few times. Early analyses were performed in $p\bar{p}$ and e^+e^- collisions at CERN [145, 146]. Also, the WA97 experiment at the CERN SPS presented [147] a $K^0_S K^0_S$ correlation function from central Pb-Pb collisions at 158 GeV/c per nucleon (see Fig. 5.7). The statistics (only 2000 pairs) were too small to extract any conclusive information about the source.

The STAR experiment at RHIC was the first to extract radii from $K^0_S K^0_S$ correlations in heavy-ion collisions. They presented [148] a K_T-integrated 1D analysis for 0-10% central collisions of Au+Au collisions at $\sqrt{s_{NN}} = 200$ GeV. Using the Lednický-Lyuboshitz analytical model discussed above, they extracted a source size of $R = 4.09 \pm 0.46 \pm 0.31$ fm at $\langle M_T \rangle = 1.07$ GeV. Fig. 5.8 shows their correlation function with fit.

ALICE has presented [149] $K^0_S K^0_S$ correlations from pp collisions at $\sqrt{s} = 7$ TeV. This was the first differential $K^0_S K^0_S$ analysis in both event multiplicity and M_T (2 bins each). This analysis also used the Lednický-Lyuboshitz analytical model. Fig. 5.9 shows the correlation functions and Fig. 5.10 shows the extracted radii.

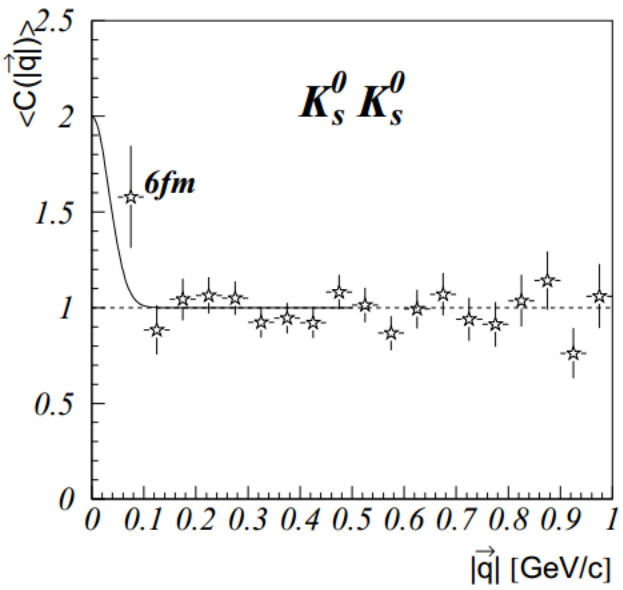

Figure 5.7: $K^0_S K^0_S$ correlation function from the WA97 experiment [147]. The line shows a Gaussian line of width $R = 6$ fm and is not a fit to the data.

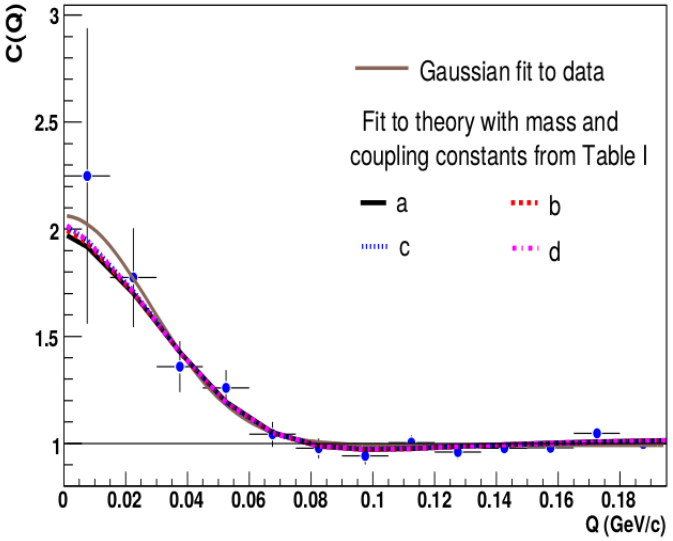

Figure 5.8: $K^0_S K^0_S$ correlation function from the STAR experiment [148]. The different fits refer to different sets of FSI parameters, similar to Fig. 5.6 of this thesis.

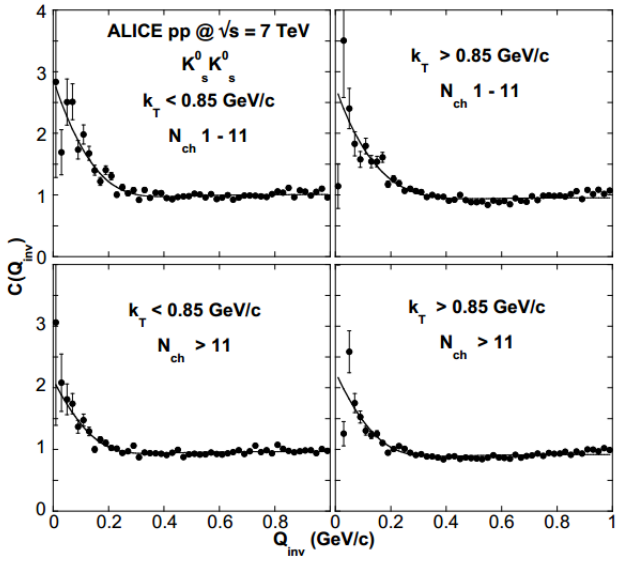

Figure 5.9: $K^0_S K^0_S$ correlation functions from ALICE [149] in pp collisions at $\sqrt{s} = 7$ TeV. Two multiplicity and two K_T bins are shown. The experimental correlation functions are divided by PYTHIA correlation functions to account for a non-femtoscopic background and fit with the Lednický-Lyuboshitz parametrization.

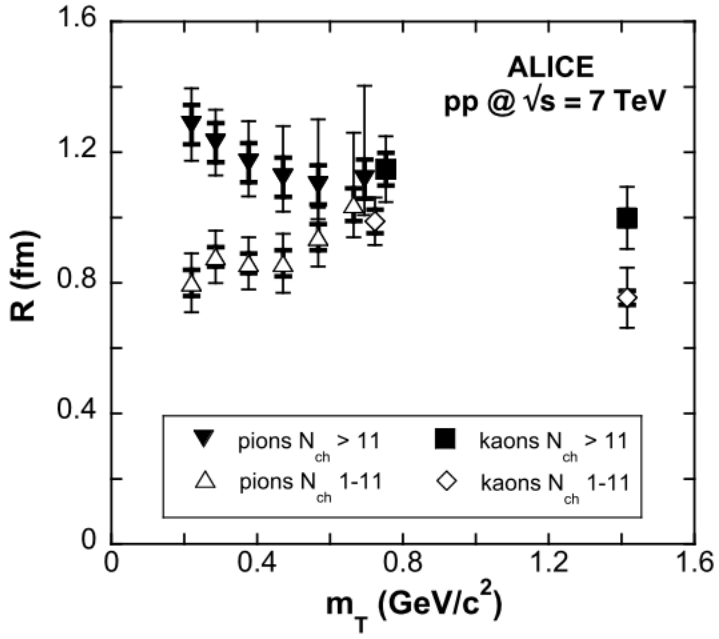

Figure 5.10: Extracted radius parameters from ALICE [149] in pp collisions at $\sqrt{s} = 7$ TeV.

The analysis presented in this thesis is the first centrality- and K_{T}-differential $K^0_{\mathrm{S}}K^0_{\mathrm{S}}$ femtoscopic analysis for heavy-ion collisions. It is also the first analysis to present three-dimensional $K^0_{\mathrm{S}}K^0_{\mathrm{S}}$ correlations, as well as the first to perform the method of Sec. 5.4 to include the strong FSI for three-dimensional correlations.

Chapter 6
Experimental Details

This chapter will document the details of the experimental aspects of this thesis.

6.1 Data selection and software

The data used in this thesis were taken from the 2010 and 2011 runs of Pb-Pb collisions at $\sqrt{s_{\mathrm{NN}}} = 2.76$ TeV from the LHC at CERN and were measured by the ALICE detector. The analysis was mostly done with the ROOT [150] data analysis software using the ALICE Off-line framework known as AliRoot [151].

Monte Carlo simulation "runs" were performed by the ALICE collaboration using the HIJING model [152]. Particle transport through the simulated detector was done using GEANT3 [153].

6.2 Event selection

6.2.1 Triggering

The main on-line trigger for ALICE physics events is generally a coincidence measurement of signals in the VZERO, SPD, and ZDC detectors (or some combination of these). An off-line event selection then discards unwanted events, such as: an "event" triggered by noise in the SPD; beam-gas events, which generally occur outside of the nominal interaction region and can be discarded using VZERO timing asymmetry; parasitic collisions involving ions outside of the main bunches, which are generally cut using a vertex z-position cut; and

electromagnetic interactions, which generally only involve ultra-peripheral collisions outside of the centrality region looked at by most analyses.

The 2010 data was collected using the minimum-bias triggers "MBand" (signals in VZERO-A and VZERO-B) and "MBor" (signals in VZERO and SPD). The 2011 data was collected using three triggers, two of which correspond to a specific centrality class: minimum bias, semi-central (0-50%), and central (0-10%). The 2011 minimum-bias trigger required signals in both ZDC detectors in addition to the VZERO measurements. The central and semi-central triggers required a certain threshold on the sum of the amplitudes measured in VZERO-A and VZERO-B [93].

6.2.2 Event centrality

The event centrality in ALICE is primarily determined by fitting the VZERO detectors' measured amplitudes with the Glauber model. Fig. 6.1 shows the distribution of the sum of amplitudes measured in the two VZERO detectors. The fit of the Glauber model to the measured data distribution determines the *anchor point*, which is the VZERO amplitude equivalent to 90% of the hadronic cross section.

The relationship between a VZERO amplitude and a centrality percentile is determined by integrating over the VZERO distribution and normalizing by the 90% region determined by the anchor point. For example, the 0-10% centrality class is bounded by the amplitude $\mathrm{V0}_{10}$ which satisfies

$$\frac{\int_{\mathrm{V0}_{10}}^{\mathrm{inf}} (dN_{\mathrm{evt}}/dV) dV}{\int_{\mathrm{V0}_{90}}^{\mathrm{inf}} (dN_{\mathrm{evt}}/dV) dV} = \frac{1}{9} \,, \tag{6.1}$$

where V is the VZERO amplitude and $\mathrm{V0}_{90}$ is the VZERO anchor point. Fig. 6.1 shows several centrality classes determined by this method. Similar Glauber fits were performed on the distribution of hits in the outer layer of the SPD and the reconstructed track in the TPC; these measurements were used for determining the systematic errors of the centrality determination. The resolution of the centrality determination ranges from 0.5% for central collisions to 2% in peripheral collisions [94].

Fig. 6.2 shows the measured centrality distributions for the 2010 and 2011 runs used

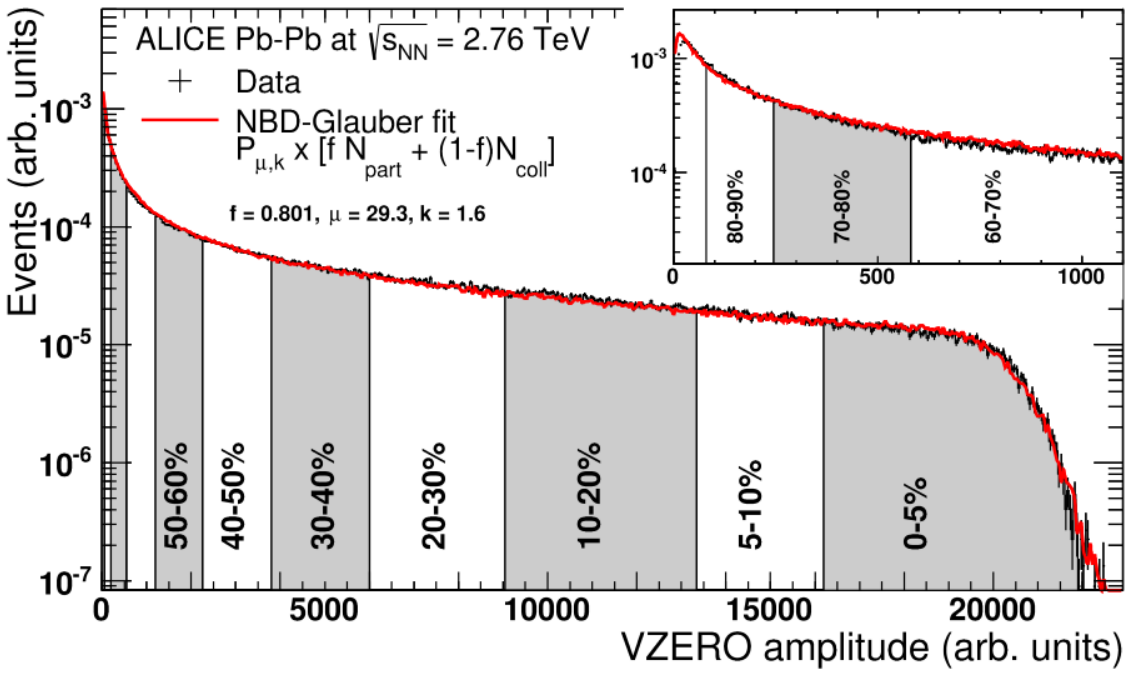

Figure 6.1: VZERO amplitude distribution used for centrality determination in ALICE [94]. The distribution was fit with an MC-Glauber calculation to detemine the centrality anchor point. Various centrality classes are shown.

in this thesis. For the 2011 data, there is a noticeable non-uniformity in the 0-10% class. To check the effect of this, a flattening procedure was performed in order to make the distribution uniform. However, the mean centrality before the flattening procedure was 4.9%, and the results of the analysis did not change after flattening, so the procedure was discarded in order to preserve statistics. A similar asymmetry exists in the 10-20% region but does not affect the results.

The plots in Fig. 6.2 each show two distributions: the events that passed the triggers and were analyzed, and the events that actually were used in the final results. Events were required to have a primary vertex z-position less than 10 cm away from the nominal interaction point of the ALICE detector and also needed to have two good K^0_S particles. These two requirements cause the difference between the two distributions, and the latter requirement is the cause of the gradual dropoff at large centrality percentile.

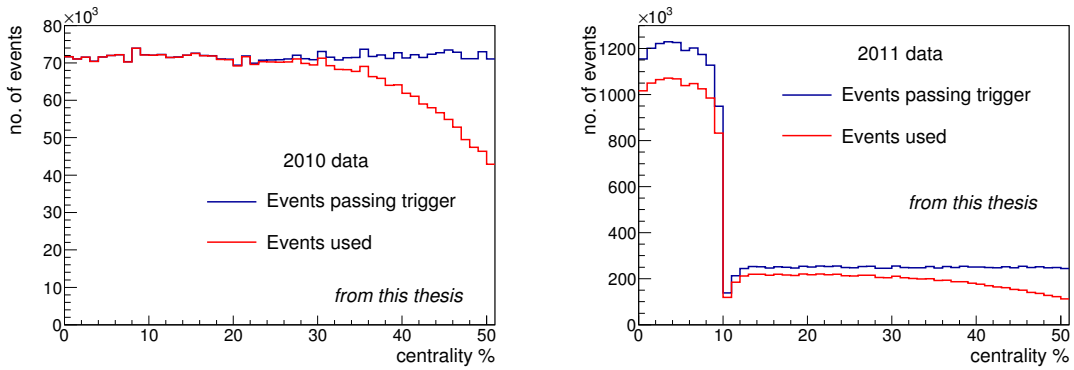

Figure 6.2: The centrality distributions measured from ALICE data from 2010 (left) and 2011 (right). The blue line refers to the events that passed the trigger and off-line physics selection, and the red line shows the events that were used in the analysis (passing z-vertex cut and possessing two K^0_S particles).

6.2.3 Primary vertex

The primary vertex position refers to the location of the nucleus-nucleus collision, which generally happens in an area parametrized by a Gaussian of width $\sigma_z \approx 5$ cm along the z-axis and a transverse width equal to the width of the beam, $\sigma_T \approx 15 - 75\,\mu$m. The position of the vertex is initially determined by tracklets (pairs of hits) measured by the SPD. This is done on-line and is needed for further on-line particle tracking. The vertex position is improved after track reconstruction is completed by using the full set of reconstructed tracks to determine the primary vertex position with the optimal resolution. The resolution of the vertex determination is ≈ 10 μm along the beam line and ≈ 25 μm in the transverse plane [154].

In this analysis and many others, the primary vertex position must be within 10 cm of the center of ALICE detector. This allows the events to use the full range of the ALICE detector and avoid edge-of-acceptance effects, as well as prevents infiltration from unwanted event types, such as parasitic or beam-gas collisions.

6.3 General particle selection

6.3.1 Track reconstruction

Track reconstruction [67] is done using the Kalman filter method. Hit points near the outermost layers of the TPC are used as seed values, and the tracking moves inward pad row by pad row through the TPC, updating the track information as it goes. Then, the tracks are propagated into the ITS, all the way to the innermost layer. Ambiguities in the track prolongation (such as more than one acceptable hit in an existing track's search window into the next layer) are allowed to propagate all the way through, and a χ^2 fit is performed to select the best track candidate. The track is then propagated back outward through the ITS and TPC (and onward to the TRD and TOF), and the track parameters are recalculated. This process is done twice: once with the track constrained to the primary vertex and once without this constraint, since some tracks are not expected to go through the primary vertex, e.g. secondary decay products. Several sets of track parameters are usually stored in the data files. For example, one can choose TPC-only tracks rather than TPS+ITS tracks, or tracks reconstructed with or without the primary vertex constraint. Different analyses prefer different types of tracks or track parameters. For example, femtoscopic analyses often use TPC-only momentum determination, as shared clusters in the ITS cause a momentum bias that leads to false correlations. Particle tracks are often selected at the individual analysis level by cutting on certain figures-of-merit associated with the tracking procedure. Several of these figures-of-merit include the number of TPC clusters (i.e. pad rows) or ITS layers that were used in the reconstruction of the track and the χ^2 value of the track minimization fit. One may also look at the unconstrained tracks and cut on the distance of closest approach (DCA) of the track to the primary vertex. This can help cut out secondary particles coming from decays; or, if you are looking for secondary particles, this can cut out primary tracks.

6.3.2 Charged-particle identification

Ionization energy loss dE/dx

Charged-particle identification in the ITS and TPC is based on the specific ionization energy loss dE/dx which describes the energy lost by the particle as it ionizes the constituent atoms of the medium through which it is passing. This parameter depends on the particle's mass, electric charge, and momentum, and is calculated using the Bethe-Bloch equation [137]

$$-\frac{dE}{dx} = Kz^2\frac{Z}{A}\left[\frac{1}{2}\ln\frac{2m_e c^2\beta^2\gamma^2 T_{\max}}{I^2} - \beta^2 - \frac{\delta(\beta\gamma)}{2}\right] . \tag{6.2}$$

Here, z^2 is the electric charge of the particle, β and γ are the relativistic kinematic variables, and $T_{\max}$ is the maximum energy transfer in a particle-electron collision; the rest of the variables relate to the electron or the medium. At low momentum, the dE/dx curve falls as β^{-2}, and then begins to rise ("relativistic rise"). dE/dx curves for different particles are separated by their masses at low momentum and eventually join at higher momentum, making dE/dx PID only usable for low-momentum particles. Fig. 6.3 shows the dE/dx curves measured by ALICE in the TPC. The ITS also can be used to measure dE/dx (see Fig. 3.4).

dE/dx PID is employed in the analysis by fitting the energy-loss signal with a Bethe-Bloch parametrization [155]

$$f(\beta\gamma) = \frac{P_1}{\beta^{P_4}}\left(P_2 - \beta^{P_4} - \ln\left[P_3 + \frac{1}{(\beta\gamma)^{P_5}}\right]\right) , \tag{6.3}$$

where the P_i are open fit parameters; these fits are shown in Fig. 6.3. The bands are each fit with a Gaussian around the mean value determined by the above parametrization, and a width σ is extracted. Then, each track is assigned a number N_σ signifying its distance from the mean of each band based on its measured dE/dx signal and momentum. One can then choose the desired N_σ to determine the strength of the PID cut.

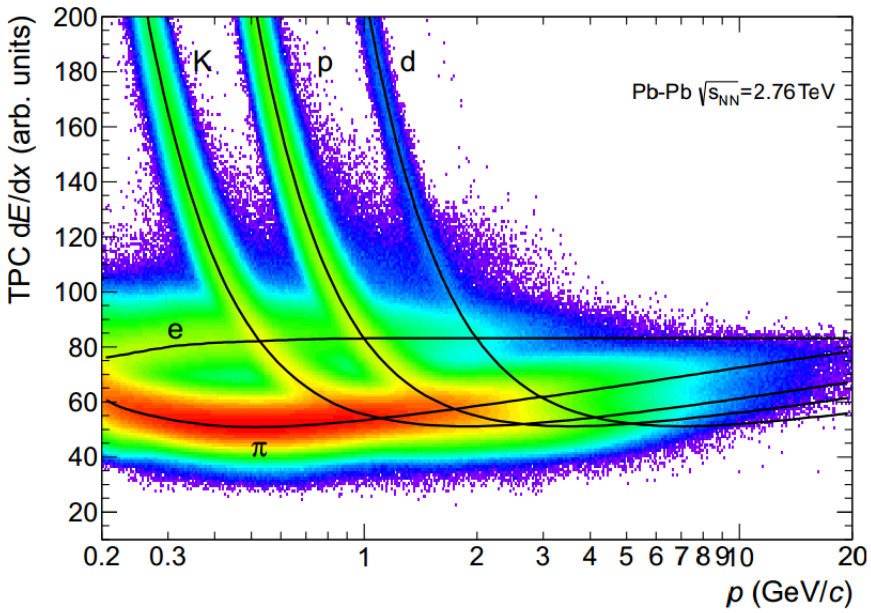

Figure 6.3: dE/dx signal from the ALICE TPC as a function of momentum in Pb-Pb events [93]. The black lines refer to a Bethe-Bloch parametrization fit to each particle species (see Eq. 6.3).

Time-of-Flight

Particles can also be identified by measuring their velocities using the TOF detector. The start time for this calculation is measured by the T0 Cherenkov detectors with a resolution of 20-25 ps [93]. The end time is then measured by the TOF detector located ≈ 4 m from the beam line. The entire TOF measurement provides a overall time resolution of about 80 ps for intermediate-momentum pions [93]. Looking at the β vs. momentum distribution, the particles separate into bands, as seen in Fig. 6.4.

Similar to the dE/dx case, one can fit a Δt distribution for a specific momentum with multiple Gaussians to determine the yields of each species. Fig. 6.5 shows an example of this procedure. Then, each track is assigned an N_{σ_i} signifying the number of Gaussian widths away from the mean value of the distribution for particle species i.

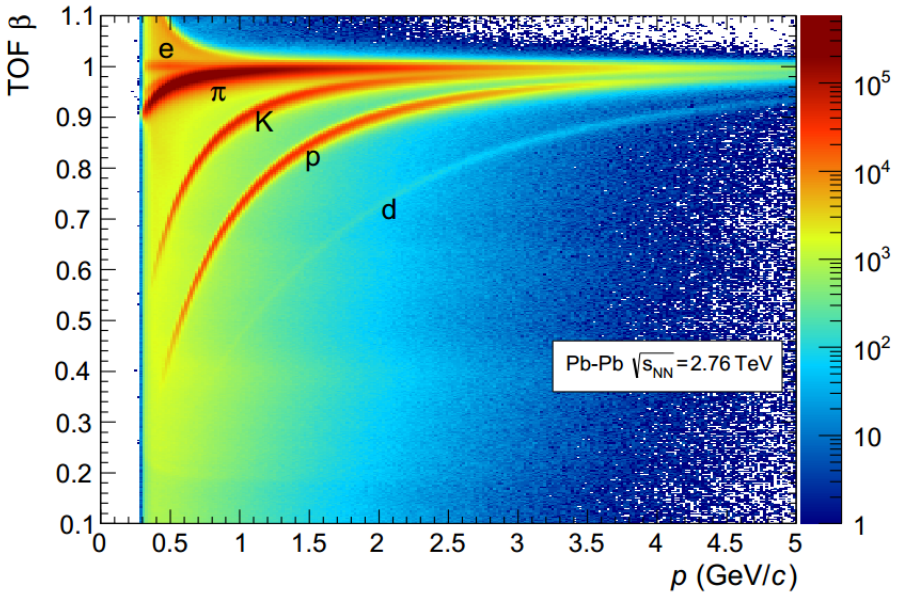

Figure 6.4: Particle identification using the ALICE TOF, showing particle velocity (β) vs momentum [93].

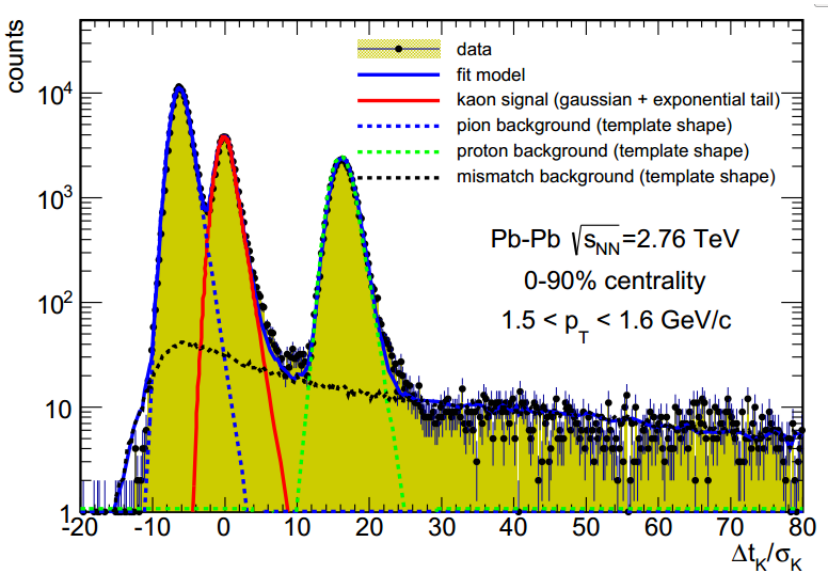

Figure 6.5: The measured TOF time signal relative to the expected time for kaons, divided by the expected kaon resolution [93]. The distribution is fit with multiple Gaussians to find the yields of several particle species for a specific momentum, which is used to calculate N_σ for TOF PID.

6.3.3 V0 finder

Some neutral particles (including the K^0_S) are reconstructed via their decay into charged particles. The detector directly measures the charged daughter tracks, and then reconstructs the decay vertex based on several topological parameters. ALICE has in place a secondary vertex reconstruction algorithm, known as the V0 finder, that searches for decay vertex candidates (called "V0s") during the particle reconstruction process. The V0 finder looks for two oppositely charged tracks that meet several topological requirements that would correspond to an actual decay vertex; see Fig. 6.6 for a schematic of these parameters. V0 candidates need to have

- daughter tracks with a large DCA to the primary vertex, to ensure daughter tracks are not primary
- a small DCA between the daughter tracks, to ensure daughters came from same decay
- a small parent DCA to the primary vertex, to ensure the parent is primary
- a small pointing angle (angle between the parent's momentum and position vectors)
- a decay length within some specified fiducial volume

These cuts are used in addition to any single-particle cuts performed on the daughters to ensure well-reconstructed tracks. Candidates that pass these first-order cuts can then be further trimmed in individual analyses by tightening the cuts, in order to achieve lower backgrounds and higher purity samples, and employing species-specific cuts, such as daughter track PID and parent invariant mass cuts.

The ALICE V0 finder has two reconstruction modes: *online* or *on-the-fly* and *off-line*. The on-the-fly reconstruction happens during the initial track reconstruction. The algorithm can make the assumption that a track is a secondary particle and recalculate the track parameters using the actual hits (clusters) in the TPC and ITS without the assumption that it must pass through the primary vertex. This improves the position and momentum resolution of the secondary vertex. Since this method uses the cluster information, which

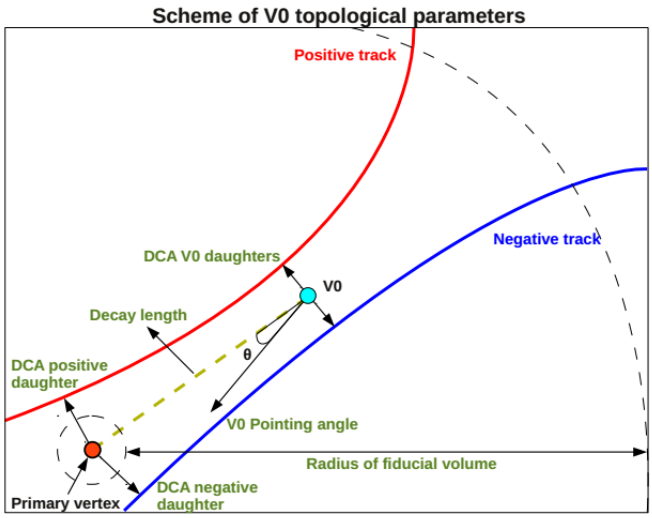

Figure 6.6: Schematic view of topological parameters used for V0 decay vertex reconstruction (plot taken from [156]).

is not stored after tracking, it must be performed during the tracking procedure. The offline V0 finder is performed after the tracking procedure is complete, simply by combining opposite sign tracks with the parameters discussed above. While this method can be tweaked and re-performed without having to reprocess the full cluster information, it generally has poorer performance than the on-the-fly method.

The parameters of the parent V0 are calculated from the parameters of the daughter tracks using conservation of momentum and relativistic kinematics. The parent momentum is simply the sum of the daughter momenta, $\vec{p}_{\mathrm{V0}} = \vec{p}_1 + \vec{p}_2$. The position of the decay vertex is located on the line connecting the daughter tracks at their DCA to each other, and the distance from each daughter track is proportional to the precision of the track parameter values. The invariant mass of the parent is determined from the mass and momentum of the daughters using conservation of total four-momentum, where

$$\begin{aligned} M_{V0}^2 &= (p_1 + p_2)^2 \\ &= (E_1 + E_2)^2 - |\vec{p}_1 + \vec{p}_2|^2 \\ &= m_1^2 + m_2^2 + 2(E_1 E_2 - \vec{p}_1 \cdot \vec{p}_2) \ . \end{aligned} \tag{6.4}$$

Of course, one needs to assume masses for the daughter particles in order to perform this calcution. One can then cut on the calculated invariant mass to select a specific species of V0.

6.4 Neutral kaon selection

In this section, I will discuss the specific procedure for selecting K^0_S particles used in this thesis. The process of selecting a pure sample is very important for femtoscopic analyses. In analyses that simply deal with integrated particle yields, such as spectra, one can usually fit some function to the invariant mass distribution and subtract the background to obtain the yield of the true signal. In femtoscopy, we must use all the particles in our signal region; there is no way to subtract out the bad particles that infiltrate the signal. On top of that, the background particles in our signal will either dilute the signal (if the particles have no correlation of their own) or disrupt the signal by imparting their own correlation, which is often unknown. Thus, a high purity sample is very important for this analysis. In this chapter, the K^0_S signal purity is determined from the $\pi^+\pi^-$ invariant mass plot by calculating

$$P = \frac{\text{Signal}}{\text{Signal} + \text{Background}} \, . \tag{6.5}$$

The background is determined by fitting a straight line to the regions outside of the accepted signal region, while the signal+background value is just taken from the distribution.

6.4.1 Daughter tracks

As stated earlier, the K^0_S particle is reconstructed via its pion daughter tracks. The cut values used for the pion tracks are shown in Table 6.1. The tracks are forced to be "TPC-refit" tracks, which means that, during the tracking procedure, the track parameters were refit using the TPC information on the outward propagation from the primary vertex after the initial inward propagation. No similar refit status using the ITS was required. There are no cuts on the number of TPC hits, the number of ITS hits, or the χ^2 value of the track fit. The tracks are required to be in the pseudorapidity range $|\eta| < 0.8$ in order to avoid

TPC refit	Yes
$\|\eta\|$	< 0.8
daughter-daughter DCA_{3D}	< 0.3 cm
daughter-primary vertex DCA_{3D}	> 0.4 cm
p_T	> 0.15 GeV/c
$N_{\sigma,TPC}$	< 3
$N_{\sigma,TOF}$ (for $p > 0.8$ GeV/c)	< 3

Table 6.1: Daughter track selection criteria.

edge effects related to the TPC acceptance window. The tracks have a minimal allowed transverse momentum to avoid low tracking efficiencies at low p_T. Daughters must have a (three-dimensional) DCA to each other smaller than 3 mm and a primary vertex DCA larger than 4 mm.

The cut values can be loosened to increase statistics or tightened to increase the purity of the sample. The topological cut values used here were determined by studying ALICE MC simulations, forming parameter distributions from real and fake particles, and looking for the values which would optimize signal purity and statistics. The cut values were later varied to study the systematic errors associated with the chosen values (see Sec. 6.8).

For pions, particle PID is not significantly important, since the vast majority of particles are indeed pions; however, we have used it here to ensure a pure sample. Daughters are required to be within 3σ of the expected value for the pion band of the TPC dE/dx distribution. TOF is used when available for particles with momentum over 0.8 GeV/c; this lower bound is used to ensure efficient TOF results. When available, daughter tracks must have a TOF time difference less than 3σ away from the expected pion value. The TOF PID supercedes the TPC PID when both are available.

6.4.2 K^0_S V0 selection

The cut values for the V0 selection are shown in Table 6.2. The V0s are reconstructed using the "on-the-fly" V0 finder. This reconstuction method was chosen mainly because it was seen to give more effective results, both in statistics and purity. For example, looking at 0-10% centrality, the off-line finder passes (after all my cuts) 9.1 V0s per event with a

Single V0 cuts	
V0 reconstruction	"on-the-fly"
$\|\eta\|$	< 0.8
decay length (3D, lab frame)	< 30 cm
decay length (2D, lab frame)	> 0.2 cm (default V0 cut)
cosine of pointing angle	> 0.99
$\mathrm{DCA}_{\mathrm{3D}}$ to primary vertex	< 0.3 cm
invariant mass	$0.480 < m < 0.515$ GeV/c^2
Pair cuts	
Unique daughters	"Merit" cut (see text)
Average separation	> 5 cm

Table 6.2: V0 selection criteria.

95% purity value, while the on-the-fly finder passes 11.4/event at 97% purity. The V0s are required to be in the range $|\eta| < 0.8$. This cut is usually used to avoid detector acceptance effects, which is why the daughter tracks must obey this cut; the cut is used for the parents primarily to be consistent with other analyses, such as charged kaons, which will also use this cut for efficiency purposes. The V0 decay must happen in the lab frame fiducial volume denoted by an outer radius of 30 cm (in 3D) and an inner radius of 2 mm (2D, in the transverse plane). The former cut was chosen due to purity/statistics reasons, while the latter cut is a default cut in the V0 finder. The DCA of the V0's extrapolated path to the primary vertex must be less than 3 mm and the cosine of the $\vec{r}, \vec{p}$ pointing angle must be greater than 0.99; both of these cuts ensure the V0s are primary particles. Lastly, to select K^0_{S} rather than some other V0 decay, we only choose V0s in the invariant mass range $0.480 < m < 0.515$ GeV/c^2.

6.4.3 Unique daughters

One issue that arises in K^0_{S} analyses is the use of the same daughter track to reconstruct more than one K^0_{S}. A pair of K^0_{S} candidates that share a daughter (determined by the track ID in the data file) will be falsely correlated; thus, we can simply assert that each *pair* of K^0_{S} particles used in the correlation must have unique daughters. However, a related problem remains, namely if three candidates are related via their products as seen in Fig. 6.7.

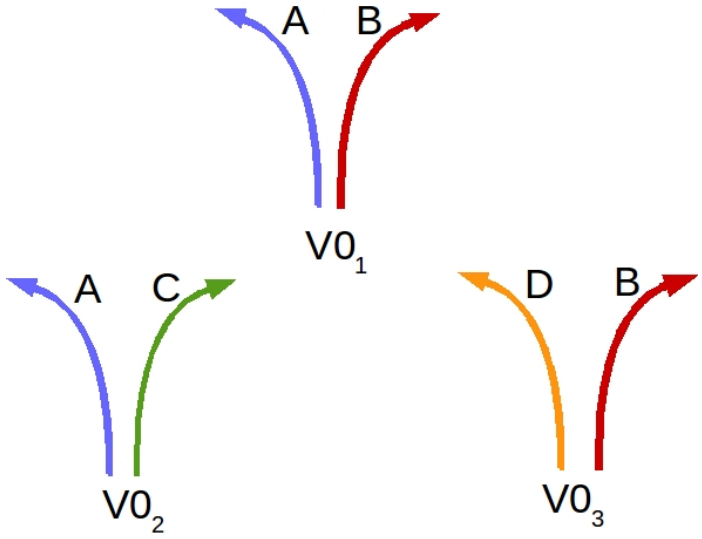

Figure 6.7: Schematic view of the "split K^0_S" problem. Here, candidates $V0_1$ and $V0_2$ share daughter A, and will not be paired; also, $V0_1$ and $V0_3$ share daughter B, and will not be paired. But, $V0_2$ and $V0_3$ would normally be allowed to pair up, even though they will likely be falsely correlated.

This scenario can happen if, for example, $V0_1$ is a real K^0_S and $V0_2$ and $V0_3$ are false combinations of real and/or fake daughters. This phenomenon has been given the name "split K^0_S". Candidates $V0_1$ and $V0_2$ share daughter A and thus will not be allowed to pair up. Also, $V0_1$ and $V0_3$ share daughter B, and will not be paired. $V0_2$ and $V0_3$, which do not share a daughter, would normally be allowed to pair up. However, they will likely be falsely correlated; in order for these V0s to pass the kinematic cuts in the analysis, it is very likely that daughters B and C are close in phase-space (since they both paired with A to make a K^0_S mass), and similarly with A and D. Then, $V0_2$ and $V0_3$ will likely also be close in phase-space, i.e. have low relative momentum and cause a false correlation in our signal region. Fig. 6.8 shows the q distribution of pairs of particles that come from the "side" regions of the mass distribution, i.e V0 candidates that have invariant masses just above or below the accepted K^0_S region (see Tab. 6.2). The distribution including all side pairs have a normal combinatoric shape, while the "split" side pairs that come strictly from the scenario above, i.e. $V0_2$ and $V0_3$, are focused at low q. The peak is not at $q = 0$ but is shifted to the right, reflecting the approximate similarity of the candidates in Fig. 6.7.

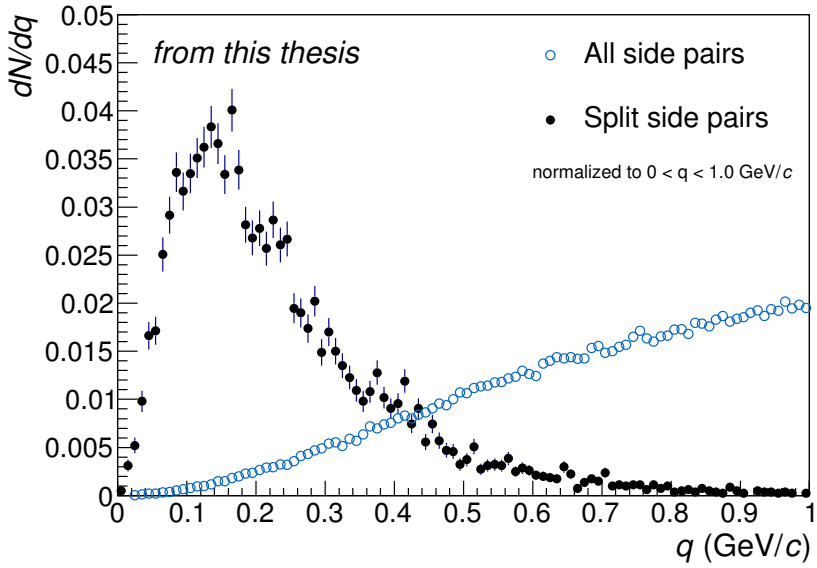

Figure 6.8: q distribution of pairs of fake V0s that have invariant masses just outside the accepted K^0_S mass range. The black points are pairs that come from a "split V0" (see Fig. 6.7)

.

To remedy this problem, we have enforced that if any two candidates share a daughter, one of them gets thrown completely out of the analysis. In order to enforce this, we have developed a "merit" cut, where we judge the candidates based on their topological parameters and keep the "better" one. Using MC simulations, several choices for the judgment parameter were tested. The invariant mass, daughter-daughter DCA, and V0 DCA were all considered, and their success at keeping the true particle and throwing away the fake candidate was 78%, 83%, and 90%, respectively. The combination of all three, where the particle which passed two of the three tests was kept, was seen to be successful at keeping the true particle in 95% of the trials. After employing this cut, it is estimated that the presence of "split K0s" in the final sample is lowered by 80%.

6.4.4 Two-track effects

Another experimental issue that affects femtoscopic analyses are the two-track effects known as *splitting* and *merging*. Splitting occurs when two tracks are reconstructed from the hit points of one real particle; this pair will give a false contribution at low q. Merging is the opposite problem, when the hit points from two real particles are reconstructed into only one track; this essentially removes a pair from the low-q region. Splitting and merging are "second-order" effects for K^0_S femtoscopy, since we are pairing V0s rather than the pion tracks; however, it is still worth accounting for and can be easily done. To combat this problem, we measured the average separation of same-sign daughter tracks for each K^0_S pair as it passed through the TPC. We measured the distance between the daughter tracks at up to nine points along the track path, corresponding to 20 cm radial steps from $R = 85$ cm to $R = 245$ cm, which are the approximate limits of the TPC. Fig. 6.9 shows the average separation of same-sign daughter tracks from pairs in the same event divided by a similar distribution from mixed events; this will divide out the combinatoric shape and show us the true two-particle effect. One can see the significant splitting peak below 1 cm, and the wider merging depletion out to $\approx$ 4-5 cm. From this, we decided to enforce that each K^0_S pair's same-sign daughters must have an average separation of more than 5 cm. It can be noted that cutting out closely separated pairs may cut out some of our signal, as K^0_S pairs with similar momentum will likely have daughters with similar momentum and thus similar trajectories. However, there is no expectation for the K^0_S decay plane to be correlated between pairs, and the signal lost by the enforcement of the cut is not significant.

6.4.5 Purity of sample

Using the cuts discussed in this section, we are left with a sample of K^0_S pairs that exhibits very high purity. Fig. 6.10 shows an invariant mass plot for a minimum-bias sample of K^0_S particles used in this analysis. This sample is taken from collisions with centrality 0-50%. The purity for these particles, calculated from Eq. 6.5, is $\approx$ 95%. This suggests that the analysis will have a very small and likely negligible contamination from feed-up correlations

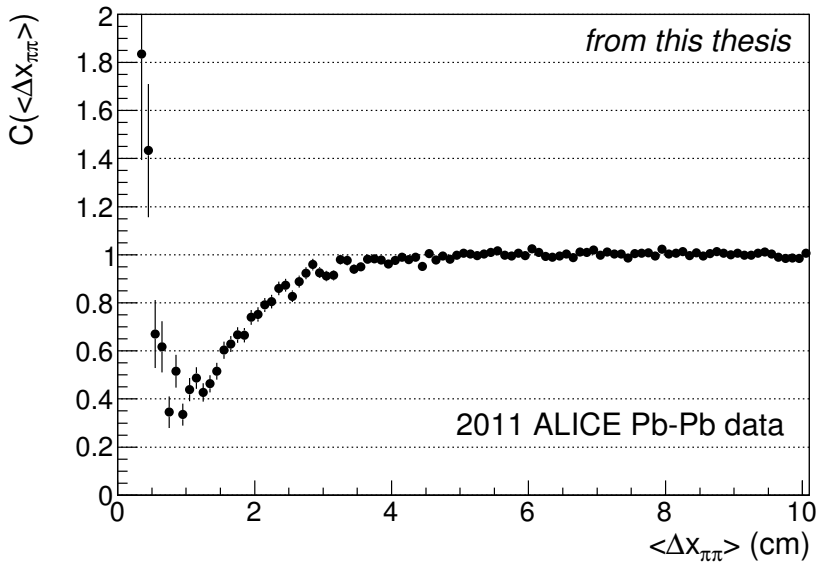

Figure 6.9: Correlation distribution of average separation of same-sign $\pi\pi$ daughters of K^0_S pairs. The average separation is calculated from up to nine points along the track path within the TPC. The correlation is built from the same-event distribution divided by the mixed-event distribution. Mixed-events are normalized to have the same primary vertex position. The distribution shows the splitting peak at low average separation followed by the merging depletion.

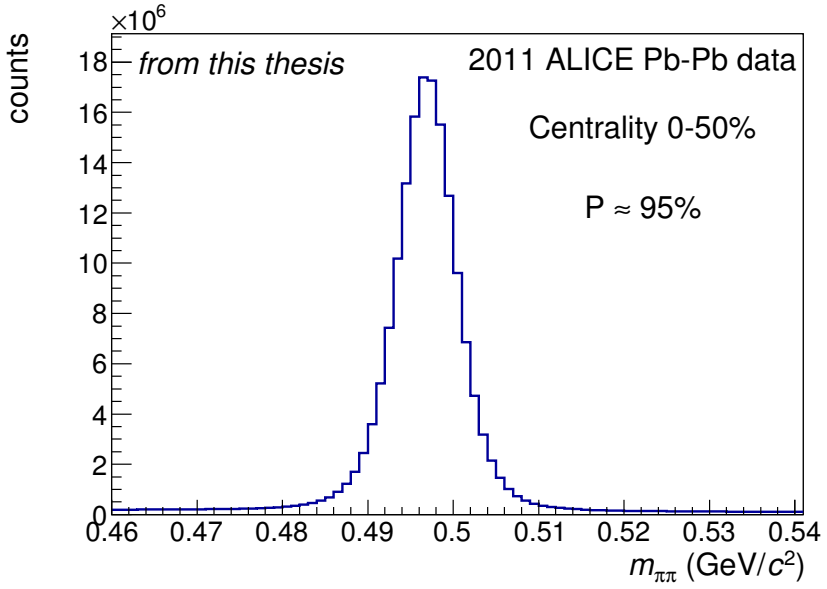

Figure 6.10: Invariant mass plot for $\pi^+\pi^-$ from K^0_S decays after implementing daughter and V0 cuts.

(e.g. $\pi\pi$ or πK^0_S), correlations of misidentified particles (e.g. $\pi \rightarrow K$), or non-correlated particles (e.g non-K^0_S pions or fake tracks).

Fig. 6.11 shows the purity values for different p_T bins. We see that the purity remains above 90% for $p_T > 0.2$ GeV/c, dropping to $\approx 70\%$ at $p_T = 0.1$ GeV/c, and peaking around $p_T \approx 1$ GeV/c. The mean p_T for the K^0_S particles used in this analysis is $\langle p_T \rangle \approx 1.1 - 1.2$ GeV/c, which is where the purity plot peaks; this generally leads to overall purity values of $\approx 95\%$ for most subsets of the sample. For example, Fig. 6.12 shows the purity values for different K_T bins. We see that the purity remains constant for all K_T at a value of $\approx 95\%$.

6.5 Correlation functions

This section will discuss various aspects of the experimental correlation function, including forming, correcting, and fitting, as well as the associated systematic errors involved with these processes.

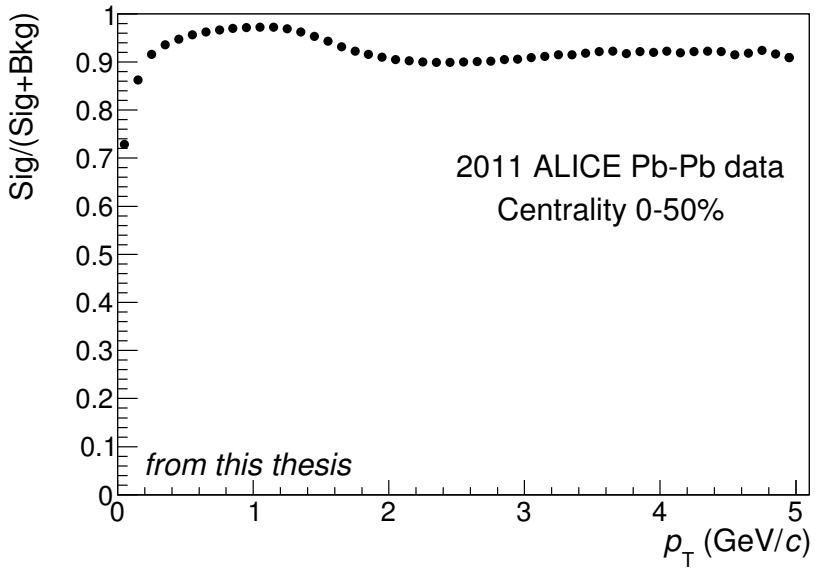

Figure 6.11: K^0_S purity vs. p_T.

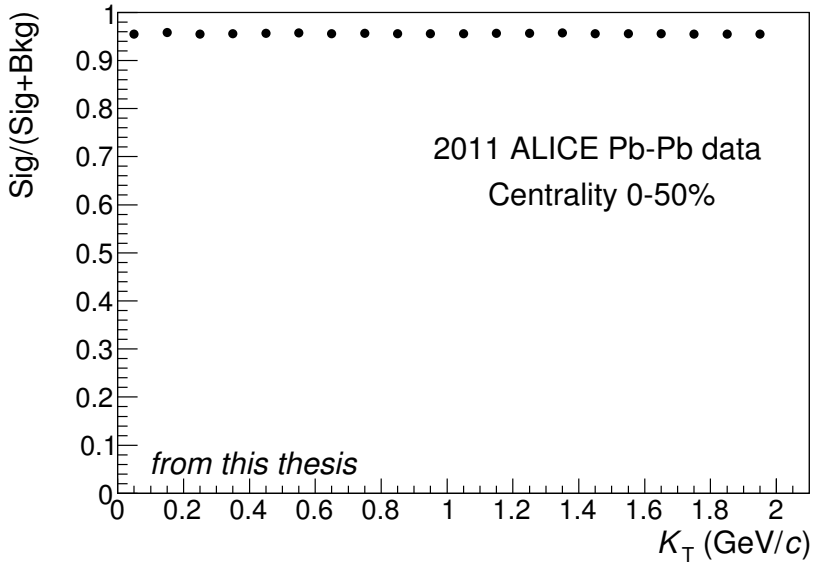

Figure 6.12: K^0_S purity vs. pair K_T.

6.5.1 Formation of the correlation function

As we stated earlier, the experimental function $C(q) = A(q)/B(q)$ is formed by building a relative momentum distribution $A(q)$ of pairs from the same event divided by a similar distribution $B(q)$ from mixed events. These distributions have 10 MeV wide q bins; this number was chosen to accommodate the available statistics and give enough bins to properly resolve the enhancement at low q. For this analysis, the correlation functions are presented in three centrality bins (0-10%, 10-30%, and 30-50%) and four K_{T} bins (0.2-0.6, 0.6-0.8, 0.8-1.0, 1.0-1.5 GeV/c). The bin sizes were chosen based on the available statistics. This is the first K^0_{S} femtoscopic analysis in AA collisions that is performed differentially in centrality or pair momentum.

This thesis presents one-dimensional (1D) and three-dimensional (3D) correlation functions. The 1D distributions were binned in the invariant relative momentum $q_{\mathrm{inv}} = \sqrt{-q^\mu q_\mu} = |\vec{q}_{\mathrm{PRF}}|$. The 3D distributions were binned in the PRF out-side-long relative momentum discussed in Ch. 4. The PRF out-side-long variables are obtained from the lab frame by the following relations:

$$q_o = \frac{M_{\mathrm{inv}}}{M_{\mathrm{T}}} \frac{(K_x q_x + K_y q_y)}{K_{\mathrm{T}}} - \frac{K_{\mathrm{T}}}{M_{\mathrm{T}} M_{\mathrm{inv}}} K^\mu q_\mu \tag{6.6}$$

$$q_s = \frac{K_x q_y - K_y q_x}{K_{\mathrm{T}}} \tag{6.7}$$

$$q_l = \frac{K_0 q_z - K_z q_0}{M_{\mathrm{T}}} \tag{6.8}$$

where $M^2_{\mathrm{inv}} = K^\mu K_\mu$.

Each correlation function is normalized to unity in the region where no correlation is expected, i.e. large q. The 1D correlation functions are normalized by dividing the numerator and denominators each by the number of pairs in the region $0.8 < q_{\mathrm{inv}} < 1.0$. The 3D correlation functions are normalized to the region $0.3 < q_i < 0.5$ in each q direction.

For the 3D analysis, an additional tweak was made when binning the $\vec{q}$ distributions. The ALICE data files store the particles in an array whose order is somehow correlated to the momentum of the particle. When looking at the 3D correlation functions, there is a $q \to -q$ asymmetry in the out direction. To combat this ordering, the order of the particles

in a pair was randomly flipped. Regardless of this order flip, this "problem" would be avoided during the fitting procedure because the correlation functions are folded into the "+++" octant, i.e. $q_i \rightarrow |q_i|$, but inclusion of this solution allows us to present plots of correlation functions correctly.

3D $\rightarrow$ 1D projections

The 3D correlation function is obviously very difficult to visualize in its original form. So, we transform it into a plottable form by projecting it along one of the three q components at a time, summing over a small region of bins in the other two directions. Usually in this analysis, the projection along q_i will be summed over $|q_{j,k}| < 0.03$ GeV/c.

6.5.2 Event mixing

As stated earlier, to form the denominator of our correlation function, we use pairs coming from mixed events. This allows us to divide out the combinatoric phase space populated by random K^0_S pairs without getting rid of the desired correlation, since pairs from different events cannot be correlated via quantum statistics or final-state interactions. In this analysis, we mix each event with five other events in its same mixing class, which is 5% wide in centrality and 2 cm wide in the z-position of the primary vertex. This is to ensure that the pair phase space sampled by the mixed-event distribution has the same structure as that from the same-event distribution.

6.5.3 Weighted combination of the correlation functions

Ideally, each correlation function would only consist of pairs that occupy the exact same phase space, which is sensitive to not only physical characteristics such as K_T and centrality, but also detector effects such as detector acceptance or functional status changes (e.g. detector dead zones or set-up characteristics, which often change over time). One could then create correlation functions for each of these "bins", fit and extract radii from each separately, and average the final results. Due to finite statistics, this is impossible. However, an effort has been made to account for these issues. In the 1D analysis, correlation

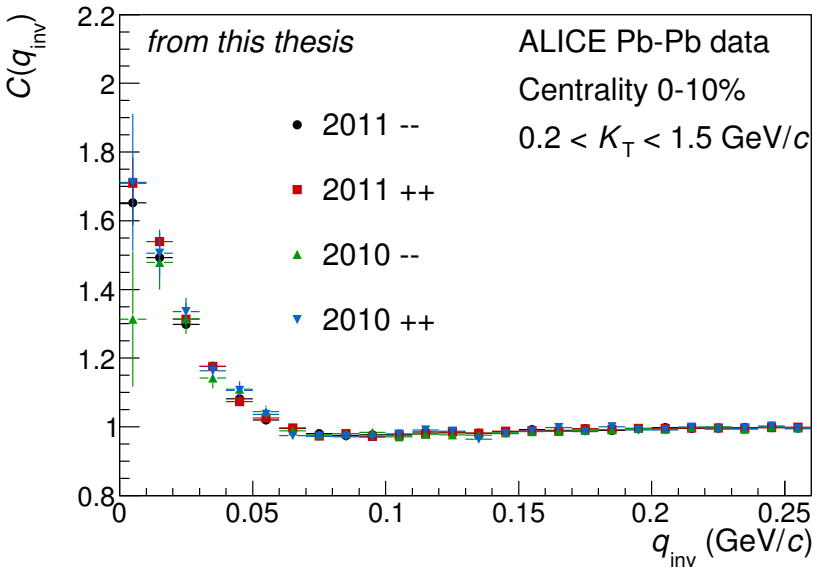

Figure 6.13: K^0_S correlation functions from different years of data taking (2010 and 2011) and different ALICE detector magnetic field orientations ("++" and "– –").

functions are formed separately for each 5% centrality class (2 or 4 bins), each year of data taking (2 bins), and each magnetic field orientation ("positive" and "negative", i.e. 2 bins). These correlation functions are then averaged, weighted by the number of pairs in their denominators. Thus, the 0-10% (10-30% and 30-50%) centrality correlation functions are the weighted average of 8 (16) separate correlation functions. For the 3D analysis, this was not performed, as the fitting procedure uses the numerator and denominator separately, and a good method to perform the averaging was not found. However, this averaging procedure is not expected to make a large difference for this analysis; checks were performed to look at the difference between results from the 2010 and 2011 data and the separate magnetic field orientations, and no significant differences were found. Fig. 6.13 shows a set of example correlation functions from different "analysis bins", which are seen to be very consistent.

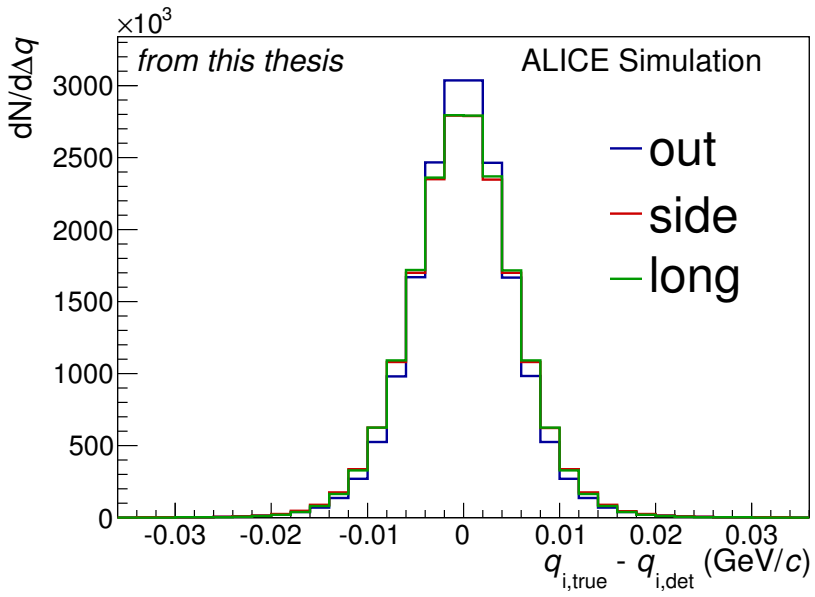

Figure 6.14: The smearing effect of finite momentum resolution on the relative momentum variables. $q_{\mathrm{i,true}}$ is the true momentum of the simulated particle, and $q_{\mathrm{i,det}}$ is the momentum "detected" using the simulated detector configuration.

6.5.4 Momentum resolution

The finite track momentum resolution of the detectors will smear the momentum distribution of reconstructed tracks. This will also affect the relative momentum distributions. This effect can be studied using HIJING MC simulations that have been run through the detector configuration using GEANT3, allowing us access to both the actual particle momentum and the momentum measured in the detector. Fig. 6.14 shows the effect of momentum smearing on the relative momentum variables; the distributions are smeared by $\approx$ 5-10 MeV/c.

To see how this affects the correlation function, we perform the following procedure. Two correlation functions were built from HIJING+GEANT3 simulated data, one using true relative momenta q_{true} and one using the "detected" q_{det}. Because HIJING does not incorporate quantum statistics or final-state interactions, the "signal" distributions were filled using weights calculated from Eq. 5.12. The weights were calculated using q_{true} and assuming some input radius R for the 1D analysis or set of radii for the 3D analysis and

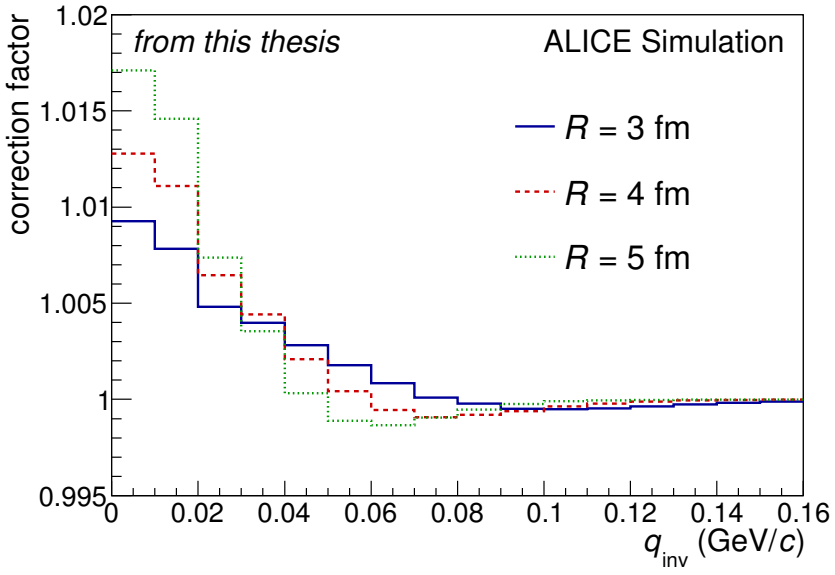

Figure 6.15: Momentum-resolution correction factor for several values of the input radius. The experimental correlation function is multiplied by this factor (using the approximately correct radius) before the fitting procedure. An iterative process can be employed to find the correct radius.

λ; the process was done for several choices of these parameters. The denominator of each correlation function was simply filled with unit weights. Then, the correction factor was found by diving the "true" correlation function by the "detected" one. Fig. 6.15 shows the correction factor for several radii.

Finally, the experimental correlation functions were multipied by this correction factor before the fitting procedure. Figures 6.16 and 6.17 show the effects of the momentum-resolution correction on the 1D and 3D correlation functions. The effect on the fit parameters is quite small, increasing the radii by a few percent at most and λ by 5-10%. An iterative process can be employed to find the correct radius; one can assume a radius, calculate the correction factor and correct the correlation function, fit it, extract a radius, and repeat the process. Because of the small effect here, this process was not necessary, and the systematic error associated with choosing the wrong radius was seen to be quite small (see Sec. 6.8).

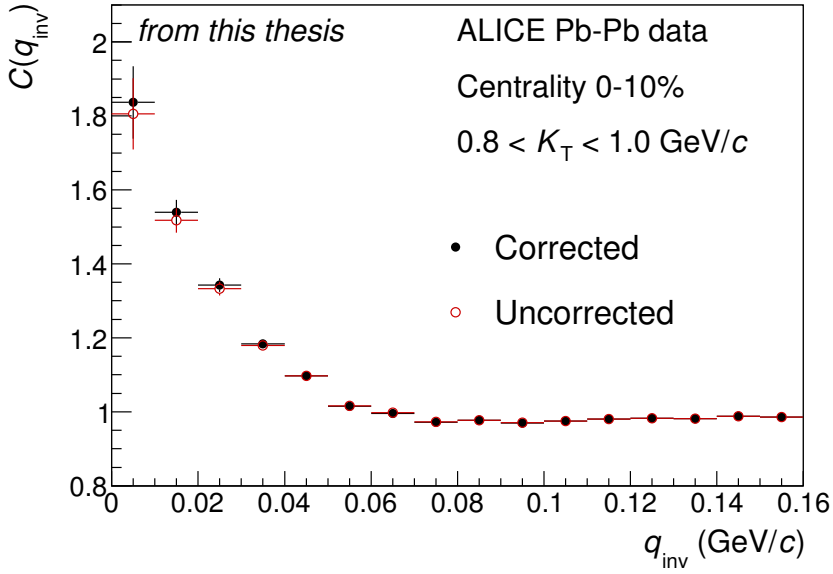

Figure 6.16: Effect of the momentum-resolution correction on the 1D correlation function.

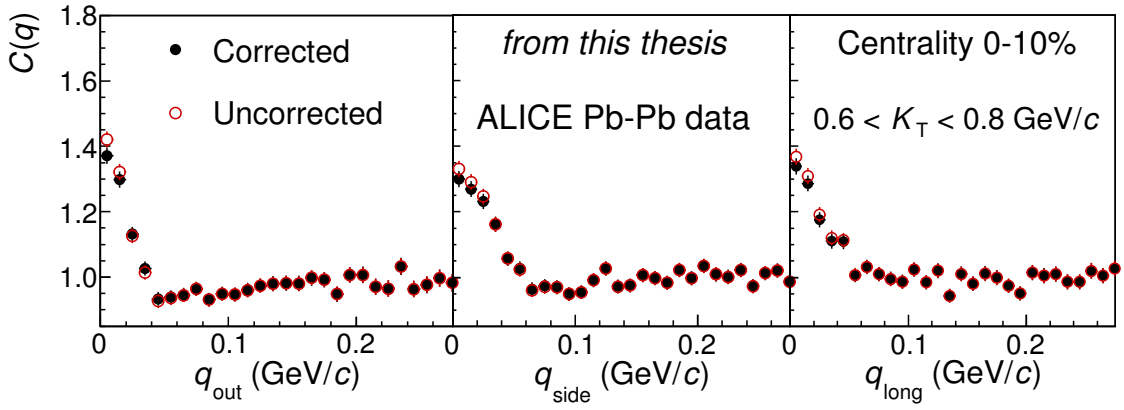

Figure 6.17: Effect of the momentum-resolution correction on the 3D correlation function. Projections along q_i are summed over $|q_{j,k}| < 0.03$ GeV/c.

6.5.5 Non-flat background

The analysis assumes a flat background at high q for the correlation functions, i.e. $C(q \to \infty) = 1$. However, a sloping, non-femtoscopic background is seen in some of the correlations; this effect grows with increasing K_{T} and with decreasing (more peripheral) centrality. The cause of this background is not fully understood. Mini-jets cause a similar background in pp collisions, but are unlikely to be significant in high-multiplicity systems. Other possible explanations that have been discussed include momentum-conservation effects or a residual effect of v_2. In the most significant example, the background differs from 1 by $< 5\%$ for the most peripheral centrality bin and highest K_{T} bin.

To account for this background, the correlation function was fit with an extra polynomial factor as

$$C_{\mathrm{fit}}(q) = \left[\lambda C_{\mathrm{theory}}(q) + (1 - \lambda)\right] F_{bkg}(q) \tag{6.9}$$

where $F_{bkg}(q)$ is a first- or second-order polynomial. The effect of this additional factor is an increase of the extracted radius and λ. Most bins saw a small increase of $\approx$ 1-2% for the radius and $< 10\%$ for λ; the most affected bin saw an increase of $\approx 10\%$ for the radius and $\approx 20\%$ for λ. Fig. 6.18 shows a close-up view of the high-q region of the correlation function; one can easily see the sloping background for the peripheral, high-K_{T} bin compared to the flat background for the central, low-K_{T} bin.

This procedure was only done in the 1D analysis. The presence of a non-femtoscopic background was not obvious in the 3D correlation functions. Also, the fit to the 3D correlation functions does not go out as far in q as does the 1D analysis, i.e. it would miss the area where it would able to access the pure background shape.

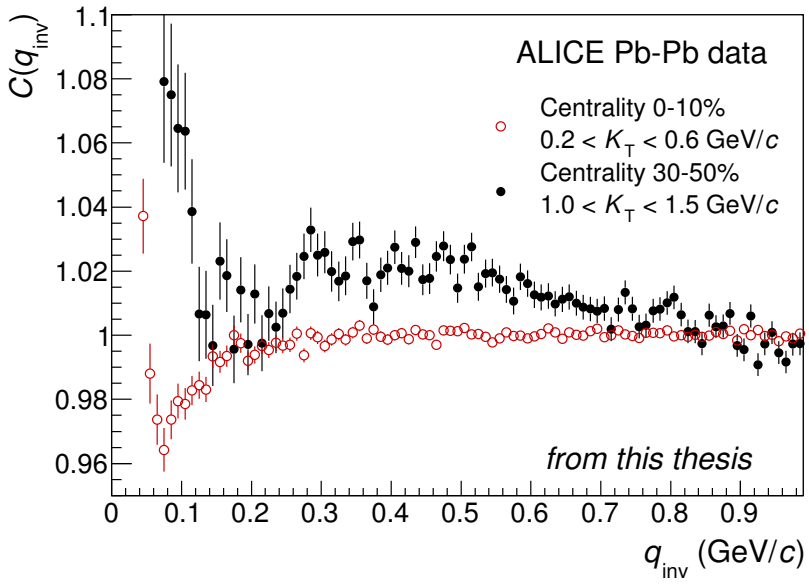

Figure 6.18: Plot showing the non-femtoscopic sloping background at high q. It is clearly visible at high K_T in peripheral collisions, but is absent for low K_T and central collisions. The slope is accounted for by including a polynomial factor in the fit function.

6.6 Fitting

6.6.1 Fitting 1D correlation functions

For the 1D analysis, we fit the momentum-resolution-corrected correlation functions with the theoretical correlation function of Eq. 5.12 with five or six open parameters: R, λ, an overall normalization factor N, and the two or three parameters of the background polynomial. We use a χ^2 fit procedure, where we minimize the value

$$\chi^2 = \sum_{i}^{q\ bins} \frac{(C_{\rm exp}(q_i) - C_{\rm theory}(q_i))^2}{\sigma_i^2} \tag{6.10}$$

where σ_i is the statistical error of the $i^{\rm th}$ bin of $C_{\rm exp}$. A common figure-of-merit for this type of fit is the summed χ^2 divided by the "number of degrees of freedom" of the fit, i.e. the number of fit points minus the number of open parameters. A χ^2/NDF value near 1 is desired, where higher numbers will indicate a worse fit or underestimated statistical errors,

and lower numbers can reflect overfitting or overestimated errors. The fit is perfomed by the MINUIT program [157]. The statistical error on the extracted fit parameters is determined (by MINUIT) by finding the region in multi-dimensional parameter space around the $\chi^2_{\rm MIN}$ value within which $\chi^2 < \chi^2_{\rm MIN} + 1$; this "width" in parameter space is the 1σ standard deviation associated with the fit parameters.

The range in q over which one should perform the fit is not obvious, and in most femtoscopic analyses, including this one, variation of the fit range leads to a systematic error. Generally speaking, we are fitting a Gaussian fit function to a distribution that often has non-Gaussian features; thus, changing the fit range will generally change the extracted Gaussian width. In this analysis, we have chosen to fit out to $q_{\rm inv} = 0.4$ GeV/c, which corresponds to 40 q bins. A systematic error associated with varying this choice will be discussed later.

As stated earlier, the FSI parameters in the fit function are taken from experiment, which has presented four different sets of values (see Table 5.2). Each correlation function was fit with each set of values, and the average of the extracted parameters from the four fit attempts was used as the final value.

6.6.2 Fitting 3D correlation functions

The method for fitting the 3D correlation functions is different in many ways to the 1D analysis. As mentioned in Ch. 5, an analytic expression for the 3D theoretical correlation function is not available. Instead, we perform a MC simulation of the freeze-out positions (using a 3D Gaussian with input width parameters) and momenta of each pair and calculate their two-particle wavefunction, building up the correlation function over many iterations of the simulation. It was found that a simulation consisting of one billion pairs was necessary to form a correlation function with statistical error bars small enough that we would be confident in neglecting them. This billion-pair simulation only takes ~ 15 min to perform. However, each iteration of the fitter needs to perform a full simulation for the new set of

input parameters[17], and since the minimization of the fit function often needs $\sim$ 200-300 iterations, the process is unreasonably time-consuming.

In order to work around this problem, we use a grid-interpolation method to perform the fit. First, we build a $4\times4\times4$ grid of simulated correlation functions (of one billion pairs each) for the following sets of input radii: $R_o = [6, 7, 8, 9]$ (fm) and R_s, $R_l = [2, 3, 4, 5]$ (fm). The correlation function for each combination of (R_o, R_s, R_l) acts as a node of the grid. Then, one calculates the desired correlation function for a specific, non-nodal set of input radii by interpolating between the grid nodes using a three-dimensional polynomial-interpolation method. The interpolated value $C(q_n; R_o, R_s, R_l)$ is determined by the expression

$$C(q_n; R_o, R_s, R_l) = \sum_{i=1}^{4}\sum_{j=1}^{4}\sum_{k=1}^{4}\left(\prod_{\substack{m=1\\m\neq i}}^{4}\frac{R_o - R_{o,m}}{R_{o,i} - R_{o,m}}\right)\left(\prod_{\substack{m=1\\m\neq j}}^{4}\frac{R_s - R_{s,m}}{R_{s,j} - R_{s,m}}\right)\left(\prod_{\substack{m=1\\m\neq k}}^{4}\frac{R_l - R_{l,m}}{R_{l,k} - R_{l,m}}\right) \times C(q_n; R_{o,i}, R_{s,j}, R_{l,k}) \ . \quad (6.11)$$

This allows us to quickly perform the fit operation while using large-statistics simulations. This method has been used in and was taken from other ongoing ALICE femtoscopic analyses.

Separate grids must be constructed using each of the four sets of FSI parameters. Also, since there are still some statistical fluctuations present in the simulations, three separate grids were constructed for each set of parameters. Thus, each correlation function was fit using twelve (4×3) different grids. The average of these twelve fits was used as the final result.

The χ^2 fit method discussed in the last section assumes Gaussian-distributed statistics. However, in the 3D case, the bin populations can approach small numbers, necessitating the use of Poisson statistical analysis. For the 3D analysis, we use a log-likelihood fit function, where the parameter (calculated for each q bin and summed over all bins) to be minimized

[17] Actually, since the fitter adjusts the parameters one at a time, new simulations are only needed for the iterations that change a radius parameter. Changes in λ or the normalization factor can be enacted via an overall scaling of the fully-built correlation function and do not require a new simulation.

is [158]

$$\chi^2_{LL} = -2\left[A\ln\left(\frac{C(A+B)}{A(C+1)}\right) + B\ln\left(\frac{A+B}{B(C+1)}\right)\right], \tag{6.12}$$

where A and B are the number of same-event and mixed-event pairs from experiment and C is the value of the theoretical correlation function calculated by Eq. 6.11. This expression approaches the usual "least-squares" χ^2 distribution in the limit of large A and B. To test, the correlation functions were fit with both expressions, and the results were seen to be consistent.

The fits were performed out to $q_i = 0.25$ GeV/c. Again, there is no obvious choice for fit range, and the variation in the results of fits using other fit ranges was used as a systematic error. Since the correlation functions are symmetric around $q_i \to -q_i$, they were "folded" into the "+++" octant by binning in the absolute values of q_i. Thus, all projection plots will only be shown for positive q_i.

The 3D correlation functions were also corrected for the effects of momentum resolution, similar to the 1D analysis case except that the correction factors had to be calculated for various combinations of the three radii. Because of the time consumption of the simulations, this was only performed for the 64 combinations used in the fitting grids, and the correction factor from the nearest combination was used, where there would be at most a 0.5 fm difference between the radius of the correction factor used and the actual radius. It will be shown in the systematic errors discussion that errors in the assumed radius have a very small effect on the results.

6.7 PRF $\to$ LCMS boosting for the 3D analysis

The simulation used to build the theoretical 3D correlation function is performed in the PRF. For one, the two-particle FSI amplitude is simpified by performing the calculation in the PRF using an equal emission-time approximation. Also, moving to a different frame would force us to account for the time component when simulating the freeze-out positions. For example, in the LCMS frame, $R_o^2 = \langle(\tilde{r}_o - \beta\tilde{t})^2\rangle$, so one would also need to simulate the time separation of the particles. Even if the r_o and t distributions are both Gaussians, a

K_{T} (GeV/c)	$\langle\gamma\rangle$	σ_γ
[0.2,0.6]	1.39	0.11
[0.6,0.8]	1.71	0.09
[0.8,1.0]	2.02	0.10
[1.0,1.5]	2.53	0.24

Table 6.3: Lorentz γ values and their standard deviations for the different 3D analysis K_{T} bins.

non-fixed pair velocity β will prevent the q_o aspect of the correlation function from having a Gaussian shape. In simpler words, the simulation of the space-time distributions would be complicated in a non-trivial way when performed in the LCMS frame.

Most 3D femtoscopic analyses, however, present their results in the LCMS frame. In order to compare with these analyses, we have used the relation $q_{o,\mathrm{LCMS}} = \gamma q_{o,\mathrm{PRF}}$, where γ refers to the Lorentz boost factor between the PRF and LCMS frames, to perform a similar boost on the radii, namely $R_{o,\mathrm{PRF}} = \gamma R_{o,\mathrm{LCMS}}$; R_s and R_l are equivalent in both frames. This scaling of the outward radius is exact for a fixed γ, or since

$$\gamma = \frac{1}{\sqrt{1-\beta^2}}, \text{ where } \beta = \left.\frac{p_{1,o}+p_{2,o}}{E_1+E_2}\right|_{LCMS}, \tag{6.13}$$

it is exact for a fixed β. However, due to statistics, we cannot perform the analysis for fixed β; the finite size of the K_{T} bins leads to a spread of β and γ values for each analysis bin. We used the average γ value for each K_{T} bin to perform the scaling, and an error involved with this boosting factor is included in the systematic errors (see Sec. 6.8). Fig. 6.19 shows the γ distributions for each of the K_{T} bins used in this analysis, and Tab. 6.3 shows the average γ values and their standard deviations.

6.8 Systematic errors

The sources of systematic errors are mostly the same for the 1D and 3D analyses. Two exceptions are the background parametrization, which is only in the 1D analysis, and the γ-boosting, which is only in the 3D analysis. Some of the details about the estimations of the errors and the values of the errors will vary between analyses.

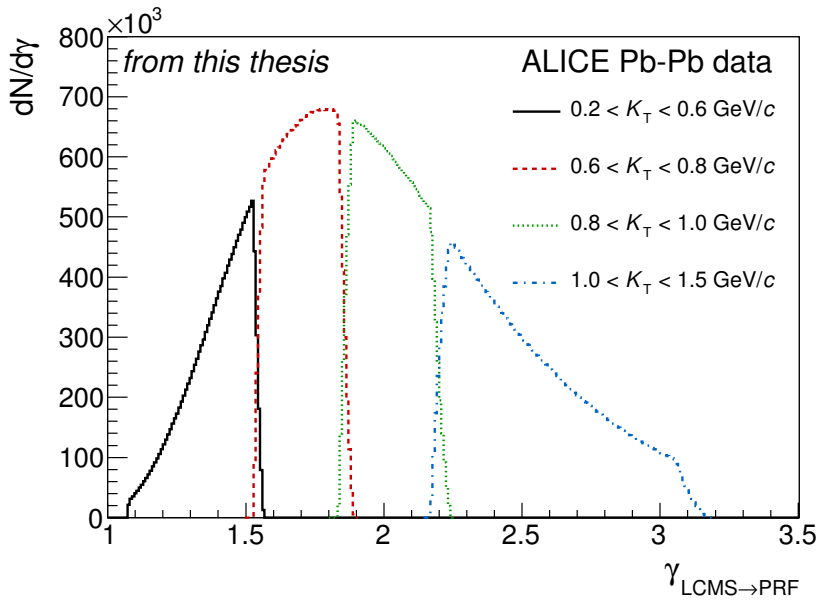

Figure 6.19: Lorentz γ distributions for different K_{T} bins. γ describes the boost between the LCMS frame and the PRF. The mean values and standard deviations of the distributions can be found in Tab. 6.3.

The calculation of the errors for the 1D analysis was rather straightforward. However, for the 3D analysis, due to the statistical fluctuations in the theoretical correlation functions used to fit the data, the systematic studies were also subject to statistical fluctuations, and it was often difficult to find a systematic error that was consistent (or at least smoothly changing) across centrality and K_{T} bins. Several of the errors (especially those associated with varying fit ranges and FSI parameters) were ultimately determined by taking various averages and fitting trend lines to the error estimations. To be safe, most of these errors are conservatively estimated. Also, these errors act together as an implicit error associated with the fluctuations of the fit method, and no explicit error was calculated. Some of the errors were allowed to have asymmetric values; however, most of them were found to be quite symmetric.

Cut parameter	tight	normal	loose
mass range (GeV/c^2)	[0.485,0.510]	[0.480,0.515]	[0.480,0.515]
max DCA K^0_S to PV (cm)	0.25	0.30	0.35
min DCA π to PV (cm)	0.45	0.40	0.35
max DCA π^+ to π^- (cm)	0.25	0.30	0.35
K^0_S 3D decay length (cm)	0.5-30	0.2-30	0.2-40
min avg. sep. (cm)	6	5	4

Table 6.4: Values used to determine systematic error of varying particle cuts for the 1D analysis.

Cut parameter	tight	normal	loose
mass range (GeV/c^2)	[0.490,0.505]	[0.480,0.515]	[0.450,0.550]
max DCA K^0_S to PV (cm)	0.1	0.3	1.0
min DCA π to PV (cm)	1.0	0.4	0.1
max DCA π^+ to π^- (cm)	0.1	0.3	1.0
min avg. sep. (cm)	10	5	0

Table 6.5: Values used to determine systematic error of varying particle cuts for the 3D analysis.

6.8.1 V0 cut values

The choice of cut values for the V0 selection can lead to changes in the results, mostly by affecting the purity of the sample. For both analyses, this study was performed for different centrality bins, but was K_{T}-integrated. For the 1D case, the values of several cuts were varied by up to $\pm$30%. Table 6.4 shows the values of the varied cuts in the 1D analysis. The effect on the fit parameters was 1-4% for R_{inv} and 2-10% for λ.

For the 3D analysis, the cuts were varied by larger differences; these values can be seen in Tab. 6.5. The correlation functions were refit using six of the twelve simulation grids (the different grids gave consistent results). The average of the six fits for each set of varied values were calculated, and the difference of these averages was used as the error. The effect on the fit parameters was 0-3% for the radii and 3-6% for λ.

6.8.2 Background parametrization

The error associated with the extra factor included in the 1D fits to account for the non-flat background was calculated by varying the form from linear to quadratic. The effect was very small for many bins but for some bins went up to 5% for R_{inv} and 4% for λ. This background factor was not included in the 3D fits.

6.8.3 Fit range

In the 1D case, the maximum q_{inv} used in the fit was varied from 0.4 GeV/c by $\pm$0.1 GeV/c. The errors calculated from these variations were up to 4% for R_{inv} and up to 3% for λ.

To study the fit range sensitivity of the 3D analysis, each correlation function was fit out to 0.15, 0.25, and 0.35 GeV/c in each q_i. This was done for all twelve of the simulation grids in order to minimize the statistical fluctuations. The differences between the extreme fit ranges and the normal fit range were calculated for each grid, and then averaged. This led to errors of 3-6% for the radii and 3-8% for λ.

6.8.4 FSI model parameters

For the 1D analysis, the fit parameters presented as the final results are the average of the fits using the four different sets of FSI model parameters. The maximum difference of the individual fits from the average was used as the error, which was 1-2% for R_{inv} and 5-10% for λ.

In the 3D analysis, the error associated with the FSI parameters was calculated by fitting each correlation function with the twelve simulation grids (three grids for each set of parameters) and taking the standard deviation of these fits. This led to errors of 3-8% for the radii and 7% for λ.

6.8.5 Momentum resolution

To find the errors associated with the momentum-resolution correction, the correction factor was adjusted by $\pm$20%. The overall effect of the momentum-resolution correction was small,

Centrality	$\langle K_{\mathrm{T}} \rangle$ (GeV/c)	Bkg.	Range	Model	Cuts	Avg. Sep.	Total
0-10%	0.48	< 1	< 1	1	2	< 1	2
	0.70	1	< 1	1	2	< 1	3
	0.90	1	< 1	1	2	< 1	2
	1.19	1	< 1	1	3	< 1	3
10-30%	0.48	1	2	1	1	1	3
	0.70	1	< 1	1	2	1	2
	0.90	< 1	< 1	1	2	1	3
	1.19	5	2	1	2	< 1	6
30-50%	0.48	5	4	1	3	2	7
	0.70	2	1	1	2	< 1	3
	0.90	4	4	1	4	2	7
	1.19	4	3	2	1	2	6

Table 6.6: Approximate systematic errors for R_{inv}. All values are given as %. The individual errors are added in quadrature to get the total.

and so its error is similarly small. For the 1D analysis, the errors were less than 1% and neglected. In the 3D analysis, the errors were mostly negligible and went up to 1% for the radii and 1-2% for λ.

6.8.6 γ boost

For the 3D analysis, the γ value used to boost the radii from the PRF to the LCMS frame had a finite spread for each K_{T} bin. The standard deviation of each distribution from the mean value (see Tab. 6.3) was used as an additional systematic error for R_{out}.

6.8.7 Total systematic errors

The total systematic errors were calculated by adding the individual contributions in quadrature. The values for the individual and combined errors for all centrality and K_{T} bins in the 1D and 3D analyses are shown in Tables 6.6 to 6.10.

6.8.8 Systematics for the correlation functions

Systematic errors were also included in some plots of the correlation functions that will be shown in Ch. 7. These errors are essentially cosmetic, showing the uncertainty in the

Centrality	$\langle K_{\mathrm{T}} \rangle$ (GeV/c)	Bkg.	Range	Model	Cuts	Avg. Sep.	Total
0-10%	0.48	< 1	< 1	5	9	3	11
	0.70	1	1	6	8	< 1	10
	0.90	1	< 1	6	7	< 1	9
	1.19	1	1	7	8	< 1	11
10-30%	0.48	1	2	6	3	4	8
	0.70	1	< 1	6	7	2	10
	0.90	< 1	1	7	2	< 1	7
	1.19	4	3	7	7	< 1	11
30-50%	0.48	3	3	7	2	3	9
	0.70	1	1	8	2	1	8
	0.90	2	3	9	10	5	15
	1.19	2	3	10	5	2	12

Table 6.7: Approximate systematic errors for λ in the 1D analysis. All values are given as %. The individual errors are added in quadrature to get the total.

Cent.	$\langle K_{\mathrm{T}} \rangle$ (GeV/c)	Param.	Fit	FSI	Mom. Res.	Cuts	γ	Total
0-10%	0.49	λ	+4,–3	±7	+2,–2	+3,–6	-	+9,–10
		R_{out}	+4,–4	±5	+0,–0	+0,–0	±8	+11,–10
		R_{side}	+4,–4	±3	+2,–0	+3,–3	-	+6,–6
		R_{long}	+4,–4	±6	+0,–0	+3,–3	-	+8,–8
	0.71	λ	+4,–3	±7	+2,–2	+3,–6	-	+9,–10
		R_{out}	+4,–4	±5	+0,–0	+0,–0	±5	+8,–8
		R_{side}	+4,–4	±3	+1,–1	+3,–3	-	+6,–6
		R_{long}	+4,–4	±6	+0,–0	+3,–3	-	+8,–8
	0.90	λ	+6,–5	±7	+2,–2	+3,–6	-	+10,–11
		R_{out}	+3,–3	±5	+0,–0	+0,–0	±5	+8,–8
		R_{side}	+5,–5	±3	+0,–0	+3,–3	-	+7,–7
		R_{long}	+6,–6	±6	+1,–0	+3,–3	-	+9,–9
	1.19	λ	+6,–5	±7	+2,–2	+3,–6	-	+10,–11
		R_{out}	+3,–3	±5	+0,–0	+0,–0	±10	+11,–10
		R_{side}	+4,–4	±3	+0,–0	+3,–3	-	+6,–6
		R_{long}	+4,–4	±6	+0,–0	+3,–3	-	+8,–8

Table 6.8: Approximate systematic errors for the radii and λ in the 3D analysis for 0-10% centrality. All values are given as %. These errors are allowed to be asymmetric (except for γ and FSI), and the "+" and "–" are signified. The individual errors are added in quadrature to get the total.

Cent.	$\langle K_{\mathrm{T}} \rangle$ (GeV/c)	Param.	Fit	FSI	Mom. Res.	Cuts	γ	Total
10-30%	0.49	λ	+4,–3	±7	+2,–2	+5,–5	-	+10,–9
		R_{out}	+5,–5	±5	+0,–0	+0,–0	±8	+11,–11
		R_{side}	+5,–5	±8	+0,–1	+3,–3	-	+10,–10
		R_{long}	+5,–5	±8	+0,–0	+3,–3	-	+10,–10
	0.70	λ	+5,–5	±7	+1,–1	+5,–5	-	+10,–10
		R_{out}	+5,–5	±5	+0,–0	+0,–0	±5	+9,–9
		R_{side}	+5,–5	±8	+0,–0	+3,–3	-	+10,–10
		R_{long}	+5,–5	±8	+0,–0	+3,–3	-	+10,–10
	0.90	λ	+5,–5	±7	+1,–2	+5,–5	-	+10,–10
		R_{out}	+4,–4	±5	+0,–0	+0,–0	±5	+8,–8
		R_{side}	+4,–4	±8	+0,–0	+3,–3	-	+9,–9
		R_{long}	+4,–4	±8	+0,–0	+3,–3	-	+9,–9
	1.18	λ	+8,–8	±7	+1,–1	+5,–5	-	+12,–12
		R_{out}	+4,–4	±5	+0,–0	+0,–0	±10	+12,–12
		R_{side}	+4,–4	±8	+0,–0	+3,–3	-	+9,–9
		R_{long}	+4,–4	±8	+0,–0	+3,–3	-	+9,–9

Table 6.9: Approximate systematic errors for the radii and λ in the 3D analysis for 10-30% centrality. All values are given as %. These errors are allowed to be asymmetric (except for γ and FSI), and the "+" and "–" are signified. The individual errors are added in quadrature to get the total.

Cent.	$\langle K_{\mathrm{T}} \rangle$ (GeV/c)	Param.	Fit	FSI	Mom. Res.	Cuts	γ	Total
30-50%	0.48	λ	+5,–5	±7	+1,–1	+3,–3	-	+9,–9
		R_{out}	+7,–7	±5	+0,–0	+0,–1	±8	+12,–12
		R_{side}	+7,–7	±8	+0,–0	+3,–3	-	+11,–11
		R_{long}	+7,–7	±8	+0,–0	+3,–3	-	+11,–11
	0.70	λ	+6,–6	±7	+1,–1	+3,–3	-	+10,–10
		R_{out}	+6,–6	±3	+0,–0	+0,–1	±5	+9,–9
		R_{side}	+6,–6	±7	+0,–0	+3,–3	-	+10,–10
		R_{long}	+6,–6	±8	+0,–0	+3,–3	-	+10,–10
	0.89	λ	+6,–6	±7	+1,–1	+3,–3	-	+10,–10
		R_{out}	+4,–4	±3	+0,–0	+0,–1	±5	+7,–7
		R_{side}	+4,–4	±7	+0,–0	+3,–3	-	+9,–9
		R_{long}	+4,–4	±8	+0,–0	+3,–3	-	+9,–9
	1.18	λ	+6,–6	±7	+1,–1	+3,–3	-	+10,–10
		R_{out}	+4,–4	±3	+0,–0	+0,–1	±10	+11,–11
		R_{side}	+4,–4	±7	+0,–0	+3,–3	-	+9,–9
		R_{long}	+5,–5	±8	+0,–0	+3,–3	-	+10,–10

Table 6.10: Approximate systematic errors for the radii and λ in the 3D analysis for 30-50% centrality. All values are given as %. These errors are allowed to be asymmetric (except for γ and FSI), and the "+" and "–" are signified. The individual errors are added in quadrature to get the total.

positions of the plot points, and are not used directly in any fitting. The sources of error used in these plots come from cut variations and momentum-resolution correction variations, with the error from the cut variations being the dominant contribution. In order to make the errors smooth, the error for each q bin was calculated as the average of the errors in nearby bins. Then, a trend line was fit to the errors to further smooth them out.

Chapter 7
Results

This chapter will show the results of the $K^0_S K^0_S$ femtoscopic correlations measured with ALICE. Unless otherwise stated, all results come from LHC Pb-Pb collisions at $\sqrt{s_{NN}} = 2.76$ TeV. Throughout this chapter, capital and lowercase $K_T(M_T)$ and $k_T(m_T)$ will be used interchangeably for pair transverse momentum (mass); this should not be confusing with regards to the literature, where they are also used interchangeably and generally are not used to stand for other parameters.

7.1 1D analysis

7.1.1 Correlation functions

Figures 7.1, 7.2, and 7.3 show the momentum-resolution-corrected 1D correlation functions for three centrality bins and four K_T bins. Included in the plots are fit lines using Eqs. 5.12 and 6.9; the lines use the FSI parameters from [141], though fit lines using the other sets of parameters look extremely similar. Several important features of the correlation functions and their fits are visible in these plots. One can see the large enhancement at low q_{inv} from the Bose-Einstein correlations. As q_{inv} increases, the data points drop below 1 due to the strong FSI. At high q_{inv}, the correlation is flat at 1 as expected. One can also see that the fit function fits the data well and is able to capture the three main features (enhancement, dip, flat background) of the data; though, for some of the correlation functions, the fit line lies under the data at low q_{inv}.

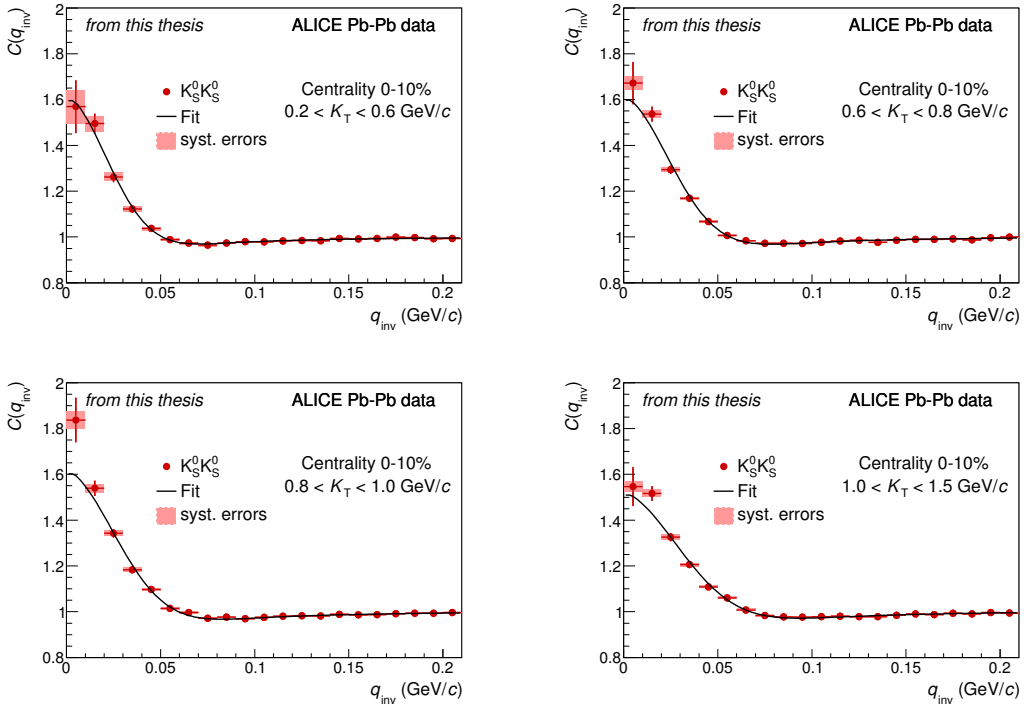

Figure 7.1: 1D correlation functions for centrality 0-10%. Also included is the fit incorporating quantum statistics and final-state interactions, using the parameter set from [141].

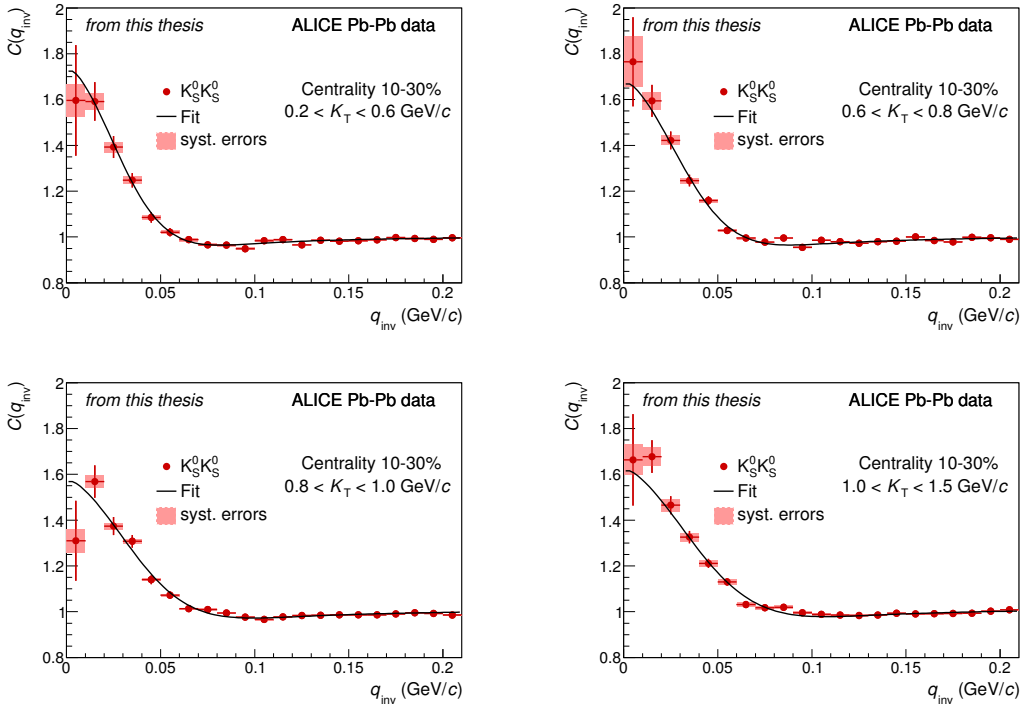

Figure 7.2: 1D correlation functions for centrality 10-30%. Also included is the fit incorporating quantum statistics and final-state interactions, using the parameter set from [141].

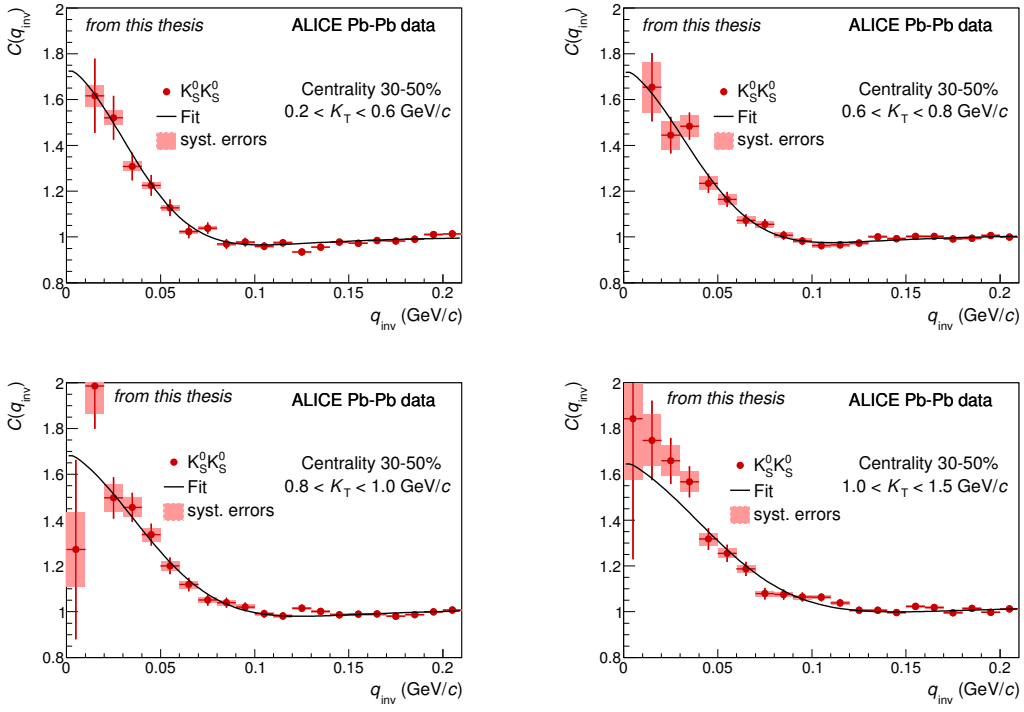

Figure 7.3: 1D correlation functions for centrality 30-50%. Also included is the fit incorporating quantum statistics and final-state interactions, using the parameter set from [141].

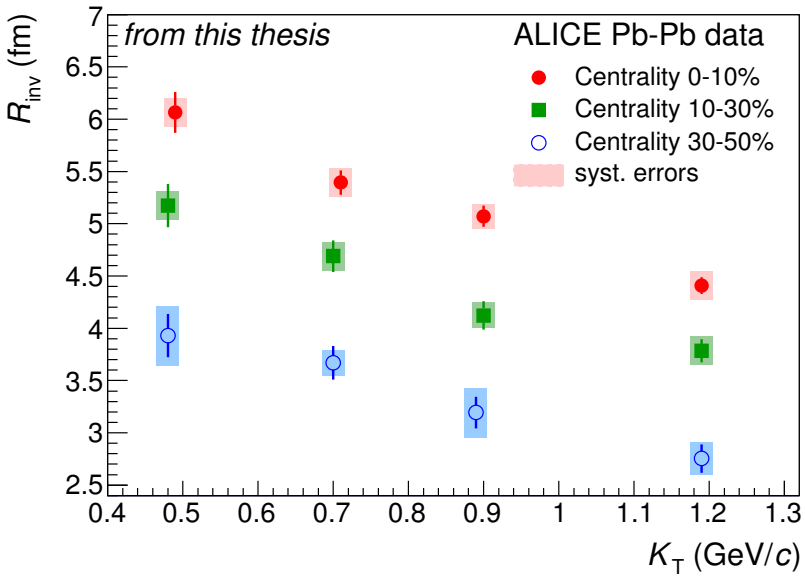

Figure 7.4: 1D $K^0_S K^0_S$ R_{inv} vs. K_T for different centrality bins.

7.1.2 R_{inv}

Fig. 7.4 shows the extracted 1D R_{inv} as a function of K_T for different centrality bins. The radii are the average of the fits from the four sets of FSI parameters. The radii decrease as one goes to more peripheral collisions; this reflects the change in the overall system size. The radii also decrease with increasing K_T; this is the expected behavior for a system that is expanding via radial flow, as was discussed in Ch. 4. This reinforces the interpretation presented in the flow analyses that collective flow is exhibited by neutral kaons in these collisions [159]. The values of the radii and their errors are listed in Tab. 7.1.

7.1.3 1D λ parameter

Fig. 7.5 shows the extracted 1D λ parameters as a function of K_T for different centrality bins. The values of λ and their errors are listed in Tab. 7.1. The values are in the range 0.5-0.75, and there are no obvious trends with centrality or K_T. There may be a moderate decreasing trend with increasing K_T, which is seen in hydrodynamic simulations (see

Cent.	$\langle K_{\mathrm{T}} \rangle$ (GeV/c)	R_{inv} (fm)	stat.(fm)	syst.(fm)	λ	stat.	syst.
0-10%	0.48	6.07	0.20	0.14	0.62	0.04	0.07
	0.70	5.39	0.12	0.14	0.61	0.03	0.06
	0.90	5.07	0.10	0.12	0.61	0.03	0.05
	1.19	4.41	0.08	0.14	0.51	0.02	0.05
10-30%	0.48	5.17	0.21	0.15	0.73	0.07	0.06
	0.70	4.69	0.15	0.12	0.67	0.05	0.07
	0.90	4.12	0.14	0.11	0.56	0.04	0.04
	1.19	3.79	0.11	0.21	0.58	0.04	0.06
10-30%	0.48	3.93	0.21	0.29	0.70	0.08	0.06
	0.70	3.67	0.16	0.12	0.67	0.07	0.05
	0.90	3.19	0.15	0.23	0.61	0.07	0.09
	1.19	2.75	0.14	0.15	0.52	0.06	0.06

Table 7.1: Fit result values for 1D R_{inv} and λ for all centrality and k_T bins with statistical and systematic errors.

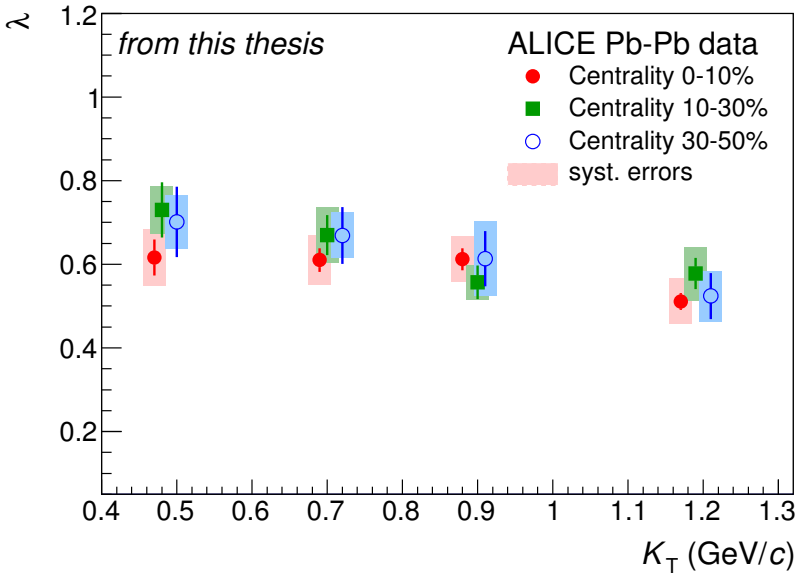

Figure 7.5: 1D $K^0_{\mathrm{S}}K^0_{\mathrm{S}}$ λ vs. K_{T} for different centrality bins.

Sec. 7.1.5 and [125]). It can be argued that this falling λ trend may be due to increasingly non-Gaussian features of the correlation function, which may grow with K_{T}. For the 1D analysis, we model the shape of the source as a spherical Gaussian with one characteristic width. If the source is not actually spherical, then this model starts to fail. We will see in the 3D results section that R_{out} in the PRF is significantly larger than R_{side} and R_{long}, making the PRF source significantly non-Gaussian (in 1D). Also, while R_{side} and R_{long} drop with K_{T}, R_{out} in the PRF actually increases with K_{T}, making the source *increasingly* non-Gaussian with K_{T}. This may be the cause for the decreasing 1D λ.

Several other factors may lead to the overall low λ values (compared to unity). If we take a single-particle purity value of 95%, then the pair parity would be 90%, bringing λ similarly down to 0.9. Also, the presence of decay products may lower λ. Using the THERMINATOR event generator [160], we studied the percentage of K^0 particles coming from various sources:

- 60% direct
- 25% from K^* (semi long-lived, $c\tau \sim 4$ fm)
- 5% from ϕ meson (long-lived, $c\tau \sim 50$ fm)
- 10% from higher-mass resonances.

If we assume that only the direct kaons contribute to the correlation, then we could estimate the correlated pair "purity" of the sample as $(0.6 * 0.95)^2 = 0.32$. If we include all of the K^* products in the correlation, which is reasonable since the mean decay length is on the order of the extracted correlation radius, the estimated pair "purity" would be $(0.85 * 0.95) = 0.65$. Thus, the extracted λ parameters are consistent with estimations from experimental pair purity and resonance considerations.

7.1.4 Comparison with other analyses

Fig. 7.6 shows the comparison of 1D R_{inv} for pions, charged kaons, neutral kaons, protons and anti-protons from ALICE Pb-Pb collisions. The radii are shown as a function of pair

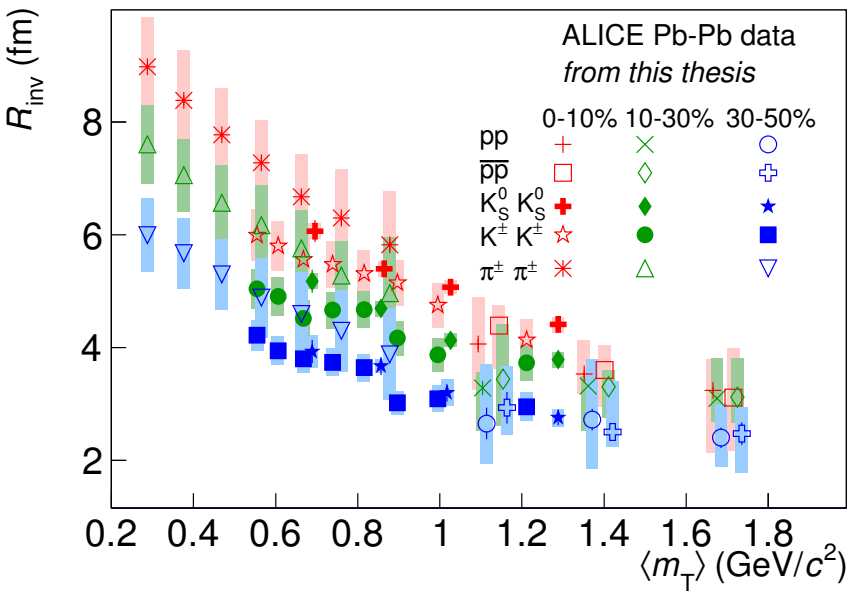

Figure 7.6: 1D $R_{\rm inv}$ vs. $M_{\rm T}$ from pions, charged kaons, neutral kaons, protons and antiprotons from ALICE Pb-Pb collisions at $\sqrt{s_{\rm NN}} = 2.76$ TeV. Statistical (thin lines) and systematic (filled rectangles) are shown. These results will be featured in an upcoming ALICE paper.

transverse mass $M_{\rm T}$. We see that the radii from the other analyses exhibit the same expected trends of decreasing radii with increasing $M_{\rm T}$ and for more peripheral collisions. We also see that the radii for the different species are consistent at overlapping $M_{\rm T}$ values *within systematic errors*, which can be quite large. A common expectation often stated in femtoscopic analyses is that source sizes in a flowing system are expected to exhibit approximately common $M_{\rm T}$-scaling, where the radii fall along the same $M_{\rm T}$ trend line. However, as discussed earlier, this common scaling is predicted for simpler expansion scenarios that are not completely justified at LHC energies [122, 123]. A recent study [124] showed that while one may expect common scaling for the 3D radii in the LCMS frame, one *should not* expect such scaling for the 1D $R_{\rm inv}$ measured in the PRF. This is due to that fact that the Lorentz γ factor that modifies $R_{\rm out}$ when switching between LCMS and PRF will be different for different particle masses. If one scales $R_{\rm inv}$ by a kinematic factor incorporating γ, which is similar to calculating $R_{\rm inv}$ in the LCMS frame, one can somewhat recover the common scaling. Fig. 7.7 shows the data points from Fig. 7.6 divided by the kinematic

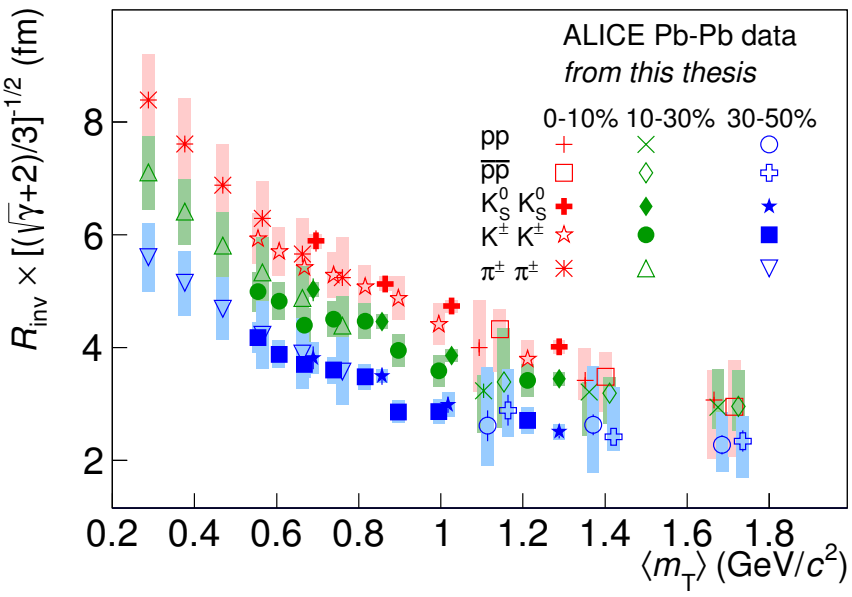

Figure 7.7: 1D R_{inv} scaled with a kinematic factor vs. M_{T} from pions, charged kaons, neutral kaons, protons and antiprotons from ALICE Pb-Pb collisions at $\sqrt{s_{\text{NN}}} = 2.76$ TeV. Statistical (thin lines) and systematic (filled rectangles) are shown.

factor $\sqrt{(\gamma_{\text{T}}^{1/2} + 2)/3}$. Here, the points exhibit a clearer common scaling than the unscaled points, matching the expectations from [124].

One can see in Fig. 7.6 that the neutral kaon radii lie systematically above the charged kaon radii (though still within systematic uncertainties). This difference is larger for central collisions. While some factors could cause differences between the two analyses, one generally expects similar femtoscopic results for charged and neutral kaons (e.g. [125]). At this time, the reason for this difference is unknown. It should be noted that the flow analysis at ALICE [159] also sees an unexpected difference in results between charged and neutral kaons which becomes more significant for more central collisions. One idea is that this is due to an inefficiency in the V0 finder in regions of high local track density, which could be sensitive to the azimuthal angle of the tracks with respect to the event plane. However, attempts to account for this issue were unsuccessful.

Fig. 7.8 shows the 1D λ parameters from the various ALICE Pb-Pb analyses. The results are somewhat scattered, but the heavier particles are generally consistent with each other

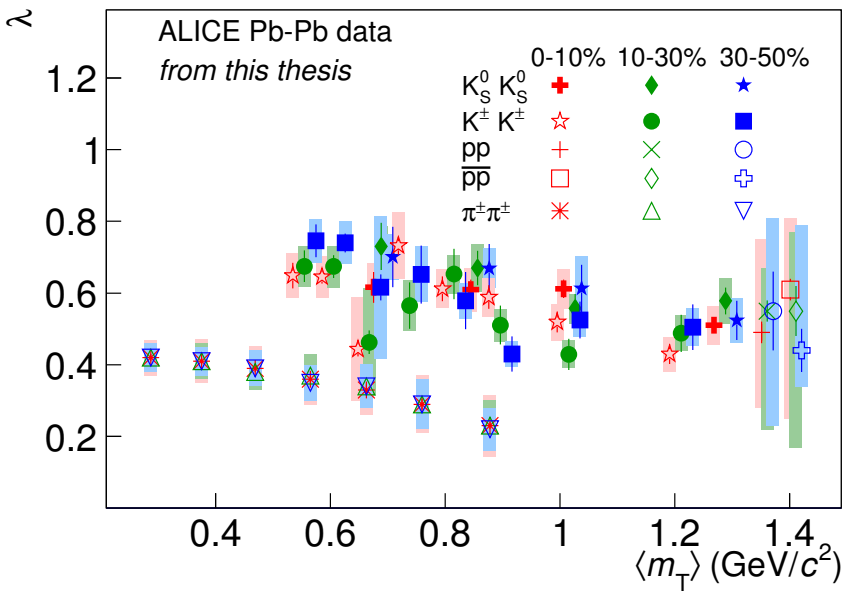

Figure 7.8: 1D λ vs. M_{T} from pions, charged kaons, neutral kaons, protons and antiprotons from ALICE Pb-Pb collisions at $\sqrt{s_{\mathrm{NN}}} = 2.76$ TeV. Statistical (thin lines) and systematic (filled rectangles) are shown. These results will be featured in an upcoming ALICE paper.

in the 0.4-0.8 range, while the pions are in the 0.2-0.4 range. The pions and the heavier particles both have general decreasing trends with increasing M_{T}, which are likely due to the kinematic explanation given above. The pion values are lower than the other particles due primarily to resonance decay products; [161] shows how the inclusion of resonance decays can dramatically drop the λ value for pions.

7.1.5 Comparison with model

Fig. 7.9 shows the comparison of the ALICE charged and neutral kaon radii for 0-5% centrality along with the predictions from the HydroKinetic Model (HKM) [125]. This model combines a hydrodynamic expansion with a final-state hadronic-rescattering phase. The model predictions shown here are for $K^{\pm}K^{\pm}$; the model also presents neutral kaon radii, which are very consistent with the charged kaons. One can see that the predictions match the charged kaon values very well quantitatively and qualitatively. The neutral kaon results match the trend of the model predictions, but lie systematically above them in value.

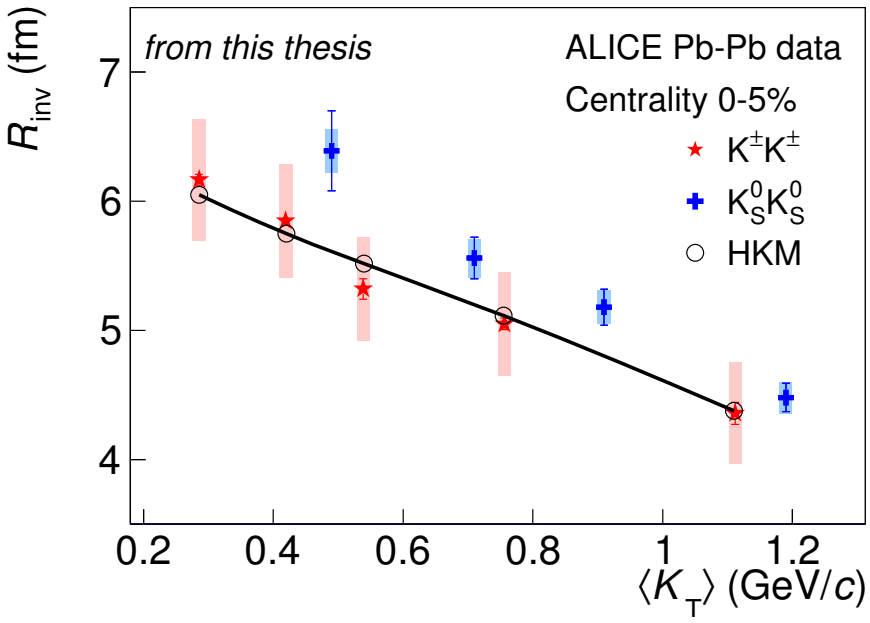

Figure 7.9: Comparison of the HKM model predictions for R_{inv} with the ALICE neutral and charged kaon results. The model predictions shown here are for $K^{\pm}K^{\pm}$. Statistical (thin lines) and systematic errors (rectangles) are shown.

Fig. 7.10 shows the comparison of the HKM λ predictions with the ALICE kaon results. The prediction matches the general decreasing trend of the data. However, the model overpredicts the data by 10-20%. A small overestimation is expected due to the fact that the model has no issues with pair purity or misidentified particles, but these factors likely cannot explain the whole difference between model and data. It is also unlikely that resonance considerations would add to the overprediction, as the model presents results with and without the inclusion of K^* and ϕ decay products, and the results are consistent. This could suggest that these decay products do not participate in the Bose-Einstein correlation, which is expected for products of ϕ but unknown for K^*.

7.2 3D analysis

7.2.1 Correlation functions

Figures 7.11 to 7.13 show the 1D projections of the momentum-resolution-corrected 3D correlation functions for three centrality bins and four K_{T} bins. These correlations are

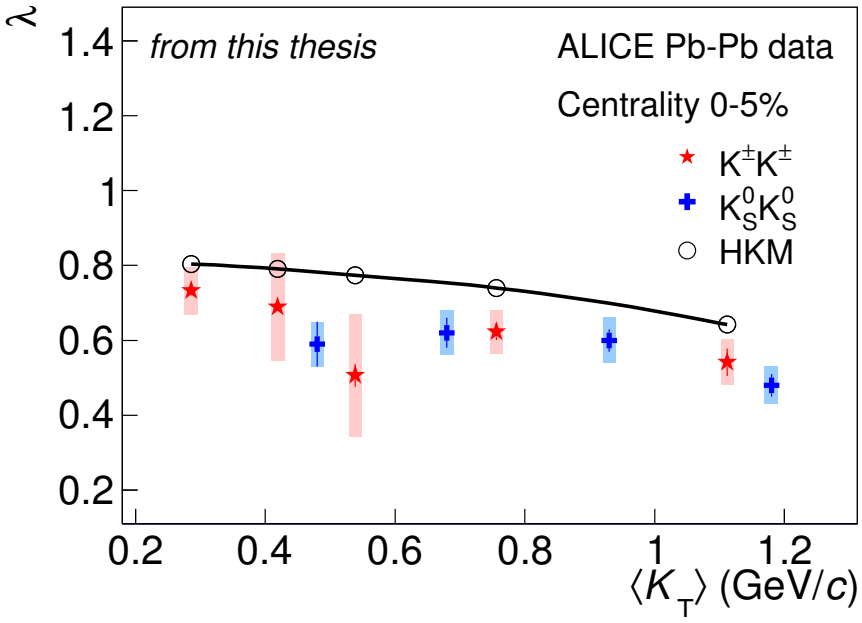

Figure 7.10: Comparison of the HKM model predictions for 1D λ with the ALICE neutral and charged kaon results. The model predictions shown here are for $K^{\pm}K^{\pm}$. Statistical (thin lines) and systematic errors (rectangles) are shown.

Cent.	K_{T} (GeV/c)	Param.	Value	stat.	syst.
0-10%	0.49	λ	0.54	0.03	+0.05,–0.05
		R_{out}	5.35	0.18	+0.57,–0.54
		R_{side}	4.83	0.14	+0.30,–0.28
		R_{long}	4.91	0.13	+0.38,–0.38
	0.71	λ	0.69	0.03	+0.06,–0.07
		R_{out}	4.58	0.08	+0.38,–0.38
		R_{side}	4.73	0.12	+0.28,–0.28
		R_{long}	4.44	0.15	+0.35,–0.35
	0.90	λ	0.70	0.03	+0.07,–0.07
		R_{out}	4.39	0.04	+0.33,–0.33
		R_{side}	3.92	0.13	+0.26,–0.26
		R_{long}	3.68	0.12	+0.33,–0.33
	1.19	λ	0.71	0.02	+0.07,–0.07
		R_{out}	3.54	0.03	+0.40,–0.40
		R_{side}	3.48	0.09	+0.20,–0.20
		R_{long}	2.98	0.10	+0.23,–0.23

Table 7.2: Fit values for the 3D LCMS radii and λ for 0-10% centrality. All values for the radii are in fm. The statistical errors are symmetric; the systematic errors are asymmetric, and the directions are denoted.

Cent.	K_{T} (GeV/c)	Param.	Value	stat.	syst.
10-30%	0.49	λ	0.66	0.06	+0.06,–0.06
		R_{out}	4.51	0.14	+0.48,–0.48
		R_{side}	4.37	0.26	+0.43,–0.43
		R_{long}	4.93	0.15	+0.49,–0.49
	0.70	λ	0.78	0.05	+0.08,–0.08
		R_{out}	4.26	0.17	+0.38,–0.38
		R_{side}	4.13	0.23	+0.41,–0.41
		R_{long}	4.00	0.20	+0.40,–0.40
	0.90	λ	0.69	0.04	+0.07,–0.07
		R_{out}	3.78	0.14	+0.31,–0.31
		R_{side}	3.45	0.17	+0.33,–0.33
		R_{long}	3.10	0.19	+0.29,–0.29
	1.18	λ	0.71	0.04	+0.08,–0.08
		R_{out}	2.92	0.09	+0.34,–0.34
		R_{side}	2.75	0.13	+0.26,–0.26
		R_{long}	2.58	0.13	+0.24,–0.24

Table 7.3: Fit values for the 3D LCMS radii and λ for 10-30% centrality. All values for the radii are in fm. The statistical errors are symmetric; the systematic errors are asymmetric, and the directions are denoted.

Cent.	K_{T} (GeV/c)	Param.	Value	stat.	syst.
30-50%	0.48	λ	0.77	0.09	+0.07,–0.07
		R_{out}	4.35	0.23	+0.51,–0.51
		R_{side}	3.58	0.34	+0.40,–0.40
		R_{long}	3.52	0.39	+0.39,–0.39
	0.70	λ	0.72	0.07	+0.07,–0.07
		R_{out}	3.49	0.12	+0.30,–0.30
		R_{side}	3.24	0.25	+0.31,–0.31
		R_{long}	3.00	0.26	+0.31,–0.31
	0.89	λ	0.73	0.07	+0.07,–0.07
		R_{out}	2.89	0.08	+0.20,–0.20
		R_{side}	2.96	0.24	+0.25,–0.25
		R_{long}	2.19	0.15	+0.21,–0.21
	1.18	λ	0.67	0.05	+0.07,–0.07
		R_{out}	2.40	0.06	+0.26,–0.26
		R_{side}	2.23	0.13	+0.19,–0.19
		R_{long}	1.70	0.11	+0.17,–0.17

Table 7.4: Fit values for the 3D LCMS radii and λ for 30-50% centrality. All values for the radii are in fm. The statistical errors are symmetric; the systematic errors are asymmetric, and the directions are denoted.

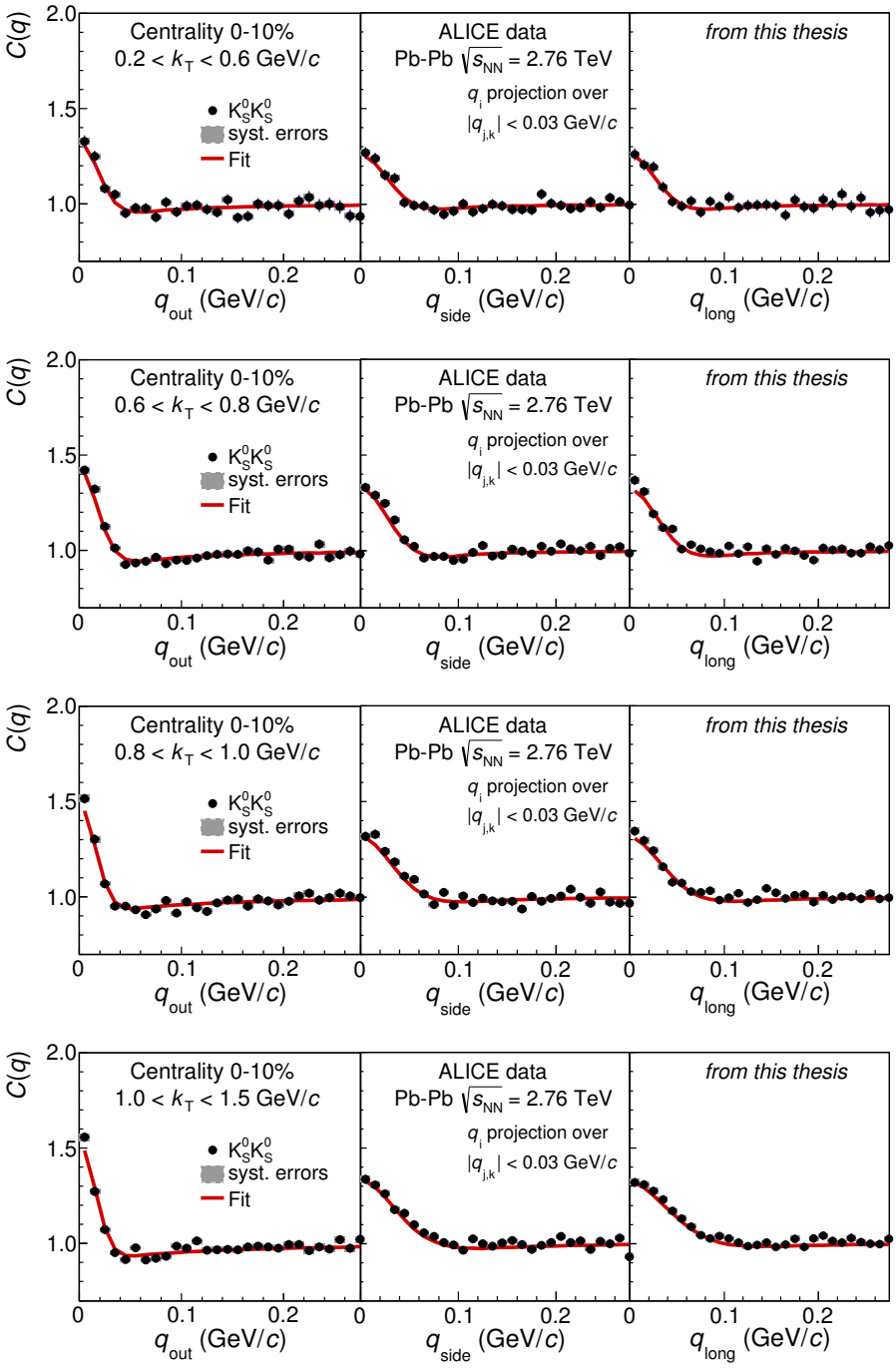

Figure 7.11: 3D correlation function projections for centrality 0-10%. Also included is the projection of the fit incorporating quantum statistics and final-state interactions, using the parameter set from [141].

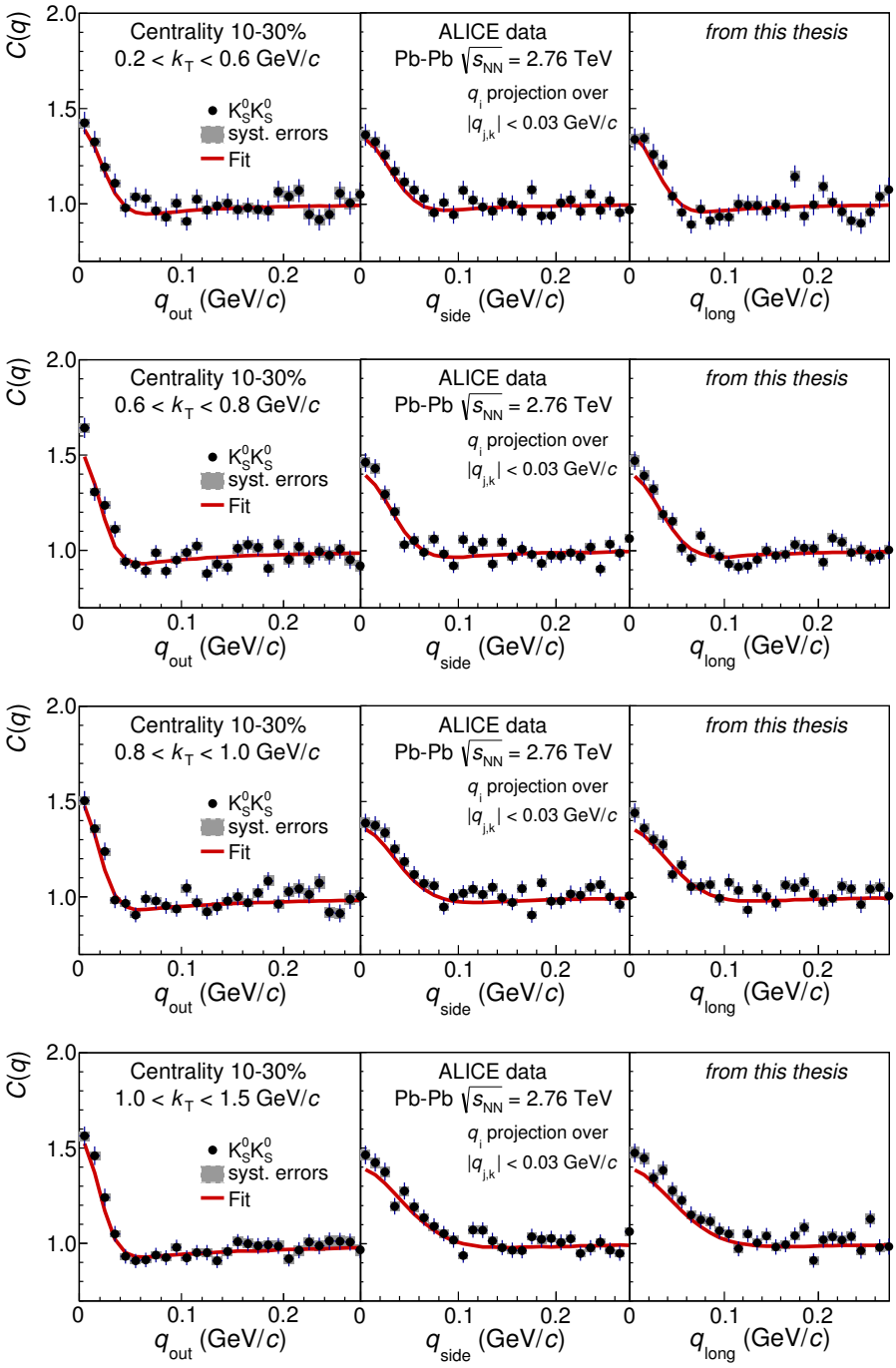

Figure 7.12: 3D correlation function projections for centrality 10-30%. Also included is the projection of the fit incorporating quantum statistics and final-state interactions, using the parameter set from [141].

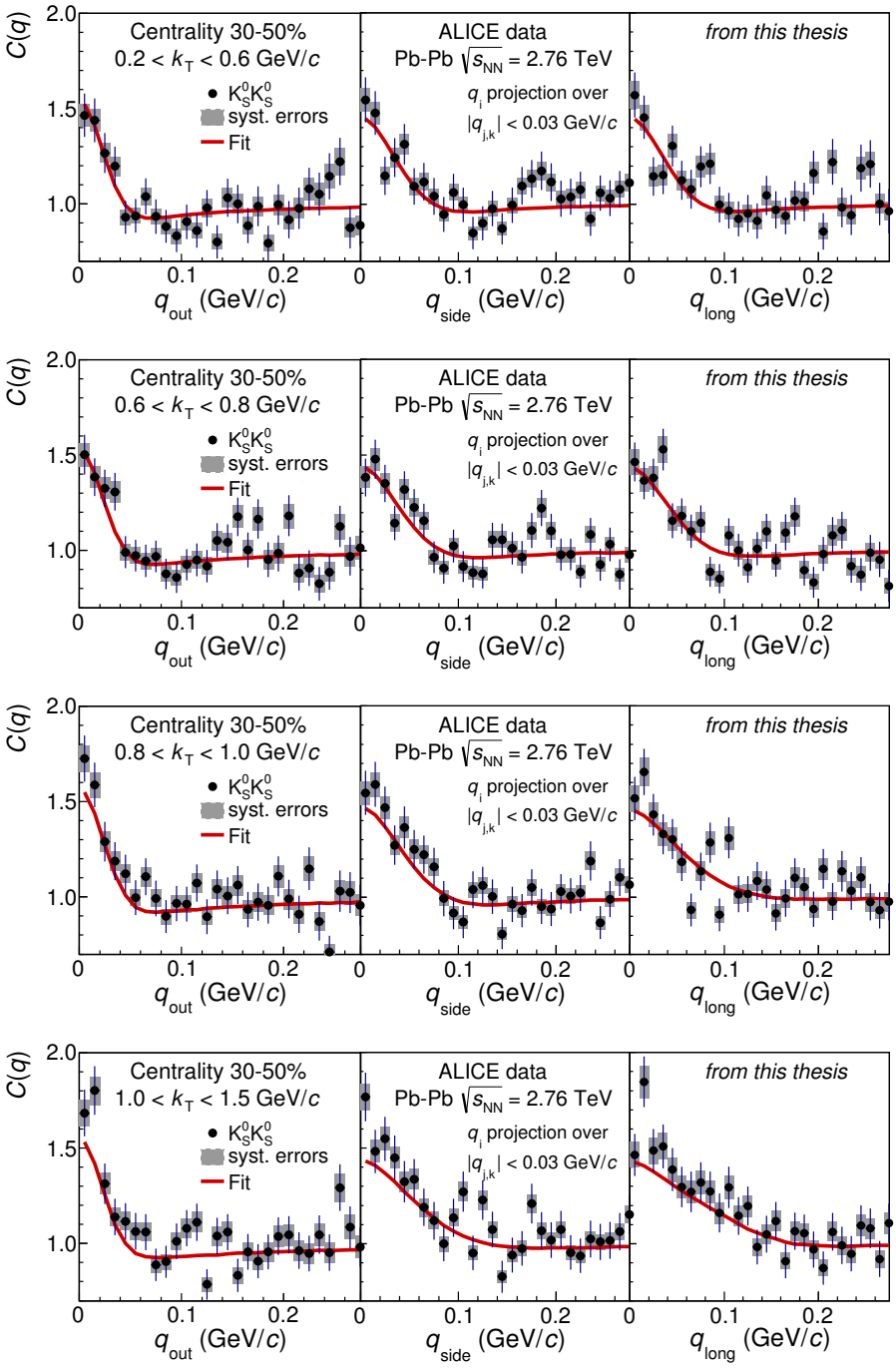

Figure 7.13: 3D correlation function projections for centrality 30-50%. Also included is the projection of the fit incorporating quantum statistics and final-state interactions, using the parameter set from [141].

measured in the PRF. The 1D plots are formed by projecting the 3D correlation function onto the q_i axis while summing over $|q_{j,k}| < 0.3$ GeV/c (which refers to three 10 MeV/c q bins). Included in the plots are the projections of the fit function using the FSI parameters from [141]. One can see the same important features as pointed out in the 1D correlation functions, namely the clear Bose-Einstein enhancement at low q, the dip below 1 at mid q, and a flat background at high q. It should be noted that the extracted λ value from these fits is significantly higher than the y-intercept of the plotted projections. This is due to the finite size of the region summed over in $q_{j,k}$ while projecting q_i; if one only used 1 bin instead of summing over several bins, the y-intercept would match the extracted λ as it does in the 1D analysis. One can also see from these projections that the width of the q_{out} correlation is narrower than the q_{side} and q_{long} correlations. Thus, the assumption of a spherically Gaussian source in the PRF employed by the 1D analysis is not well justified.

7.2.2 3D radii

Fig. 7.14 shows the 3D LCMS radii vs. M_{T} in three centrality bins for $K^0_{\text{S}}K^0_{\text{S}}$ and $\pi\pi$ from ALICE. The values for the $K^0_{\text{S}}K^0_{\text{S}}$ radii and their errors are listed in Tables 7.2 to 7.4. As mentioned before, the K^0_{S} radii were measured and fit in the PRF, and the extracted R_{out} was scaled by the γ boost factor. The pion results were measured and fit directly in the LCMS frame. The radii for all three directions show the expected trends: decreasing with increasing M_{T} and for more peripheral collisions.

We can compare the pion and kaon results to look for common M_{T}-scaling. For R_{side} and R_{long}, the kaon and pion results are consistent within errors for overlapping M_{T} values, though the kaon points are systematically slightly higher than the pion results. One could claim approximate common M_{T}-scaling, more so at large M_{T}; kinematics and statistics do not allow us to extend the kaon results to lower M_{T}, where it looks like the deviation might be largest. However, for R_{out}, there is a significant difference between the kaon and pion results, and no common M_{T}-scaling can be claimed here.

As stated earlier, while approximate common M_{T}-scaling is a qualitative expectation of hydrodynamics, it is unclear how quantitatively exact this scaling should be. Ref. [124]

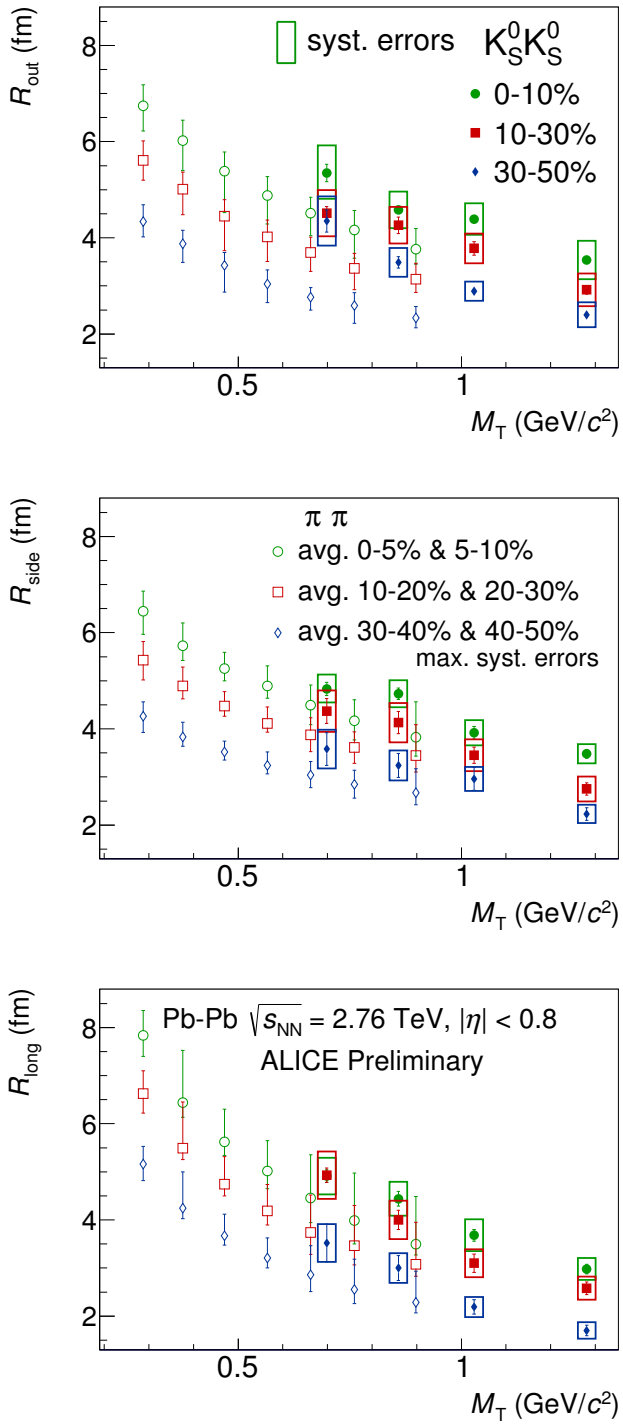

Figure 7.14: 3D LCMS radii vs. M_T for $K^0_S K^0_S$ and $\pi\pi$ from ALICE. For the kaons, statistical (thin lines) and systematic (boxes) errors are shown. For the pions, systematic errors (thin lines) are shown, while statistical errors are negligible. The pion points are averaged from narrower centrality bins (as told in the legend). The systematic errors for the pions are the maximum errors from the pre-averaged points.

predicts common scaling for pions, kaons, and protons to within 10-20%; however, that model does not take final-state hadronic rescattering into account. The HKM model [125], which includes hadronic rescattering, predicts no common scaling between pions and kaons at LHC energies and suggests that it is the effects of final-state hadronic rescattering that can drive the species to different freeze-out characteristics. Thus, the fact that we see no conclusive common M_{T}-scaling should not be entirely surprising.

7.2.3 $R_{\mathrm{out}}/R_{\mathrm{side}}$ ratio

The $R_{\mathrm{out}}/R_{\mathrm{side}}$ ratio can be connected to the emission duration, i.e. the difference in proper time of the freeze-out of different particles. From Eqs. 4.30 and 4.31,

$$\frac{R_{\mathrm{out}}^2}{R_{\mathrm{side}}^2} = 1 + \frac{\beta_{\mathrm{T}}^2(\Delta t_*)^2}{R_*^2} \tag{7.1}$$

where R_* and Δt_* are combinations of geometric and dynamic (flow) considerations. One of the expectated characteristics of the QGP was a longer-lived system which would exhibit a longer freeze-out duration, and femtoscopists expected to find increased $R_{\mathrm{out}}/R_{\mathrm{side}}$ ratios significantly above unity. However, the data showed that the ratio remains near unity even at LHC energies [120]. Fig. 7.15 presents the K_{S}^0 ratio from ALICE, showing consistency with unity for all centralities and M_{T} values. However, this does not necessarily suggest that the emission duration is indeed small. The true relationship between the extracted radii and the emission duration has significant dependences on flow terms and is certainly non-trivial, especially at large M_{T}; in fact, Heinz and Jacak say that "the extraction of the emission duration must thus be considered the most model-dependent aspect of the HBT analysis [101]". Further discussion goes beyond the scope of this thesis.

7.2.4 R_{long}^2 vs. M_{T}: freeze-out time

Using Eq. 4.32, we can extract a proper kinetic freeze-out time τ_f from the M_{T} dependence of R_{long}^2. This τ_f represents the average kinetic freeze-out proper time for particles emitted thermally, assuming a boost invariant source with weak transverse expansion. Fig. 7.16 shows the ALICE results of R_{long}^2 vs. M_{T} for pions [120] and K_{S}^0 in 0-5% central collisions.

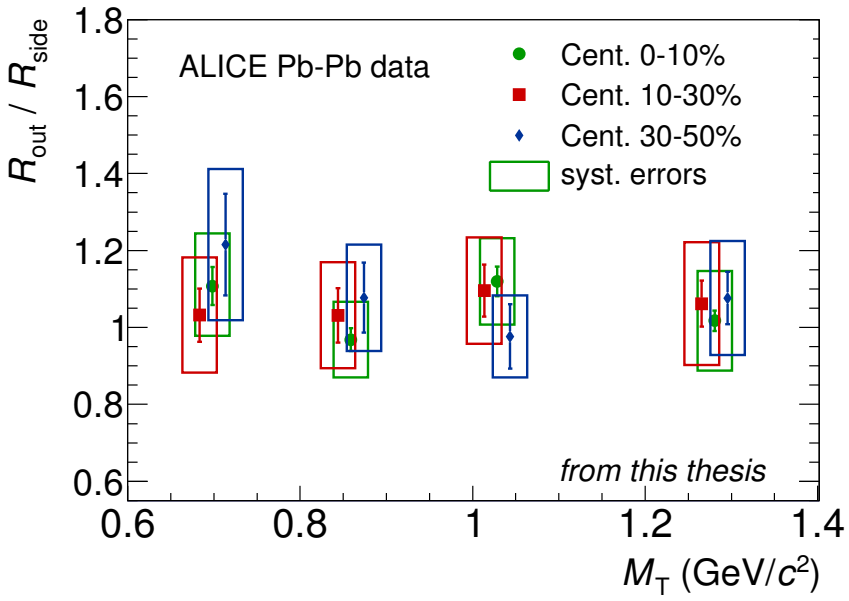

Figure 7.15: The $R_{\text{out}}/R_{\text{side}}$ ratio of $K^0_S K^0_S$ correlations from ALICE. Statisical (thin lines) and systematic (boxes) errors are shown. The M_T values for 10-30% and 30-50% are shifted slightly for clarity.

The points were fit three times: just pions, just kaons, and the combination of pions and kaons. All three fits were consistent with a freeze-out time of $\tau_f \approx 10$ fm/c. The fit assumed a thermal emission temperature of 120 MeV; this was varied by ± 20 MeV to estimate a systematic error of $\approx 10\%$. While this is a simplified model that is likely only partially justified here, it still suggests that there is no obvious significant differences in the average freeze-out times of kaons and pions in LHC collisions.

7.2.5 3D λ parameter

Fig. 7.17 shows the 3D λ parameters extracted from the ALICE $K^0_S K^0_S$ correlations. The λ values and their errors are listed in Tables 7.2 to 7.4. The values are in the range 0.5-0.8, and there are no significant trends with centrality or M_T. These values are similar to the 1D results and, like those results, are mostly consistent with the predictions made from resonance decay and experimental purity considerations. Because of the error bars, we cannot say for certain whether or not we see the downward trend visible in the 1D analysis,

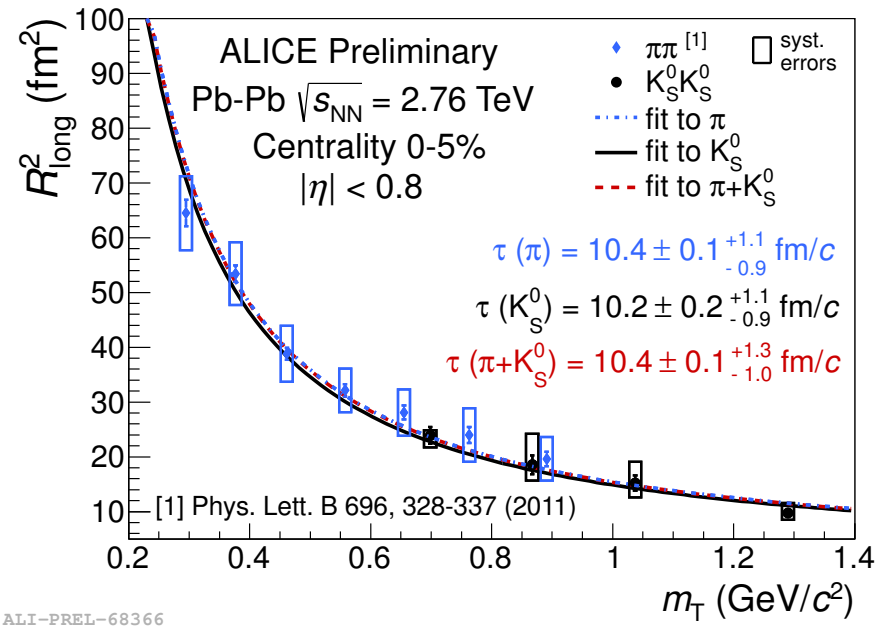

Figure 7.16: R^2_{long} vs. M_{T} for K^0_{S} and pions [120] from ALICE. Statistical (thin line) and systematic (boxes) errors are shown. The lines are fits to the data using Eq. 4.32 assuming a temperature of 120 MeV. The freeze-out proper times τ were extracted from the fits, and the systematic errors on τ come from varying the temperature by ±20 MeV.

which arose because of the non-Gaussian and specifically non-spherical shape of the PRF source; however, we would not expect to see such a trend here. Generally speaking, we may in fact expect to see the opposite trend, with λ rising with M_{T} due to increased purity and decreased resonance contributions; however, in this analysis, purity and resonance effects are minimal and not expected to change much with M_{T}.

7.2.6 Comparison with model

Fig. 7.18 shows the three 3D LCMS radii and the $R_{\text{out}}/R_{\text{side}}$ ratio vs. M_{T} for 0-5% central collisions from ALICE $\pi\pi$ [120] and $K^0_{\text{S}}K^0_{\text{S}}$ along with the HKM predictions [125]. The comparison between pions and kaons was discussed above and is the same for this centrality bin. The HKM predictions do not predict a common M_{T}-scaling for pions and kaons, and the most significant difference is predicted for R_{long}. The experimental K^0_{S} results are very consistent with the HKM predictions except possibly for R_{long} at low M_{T}. The HKM

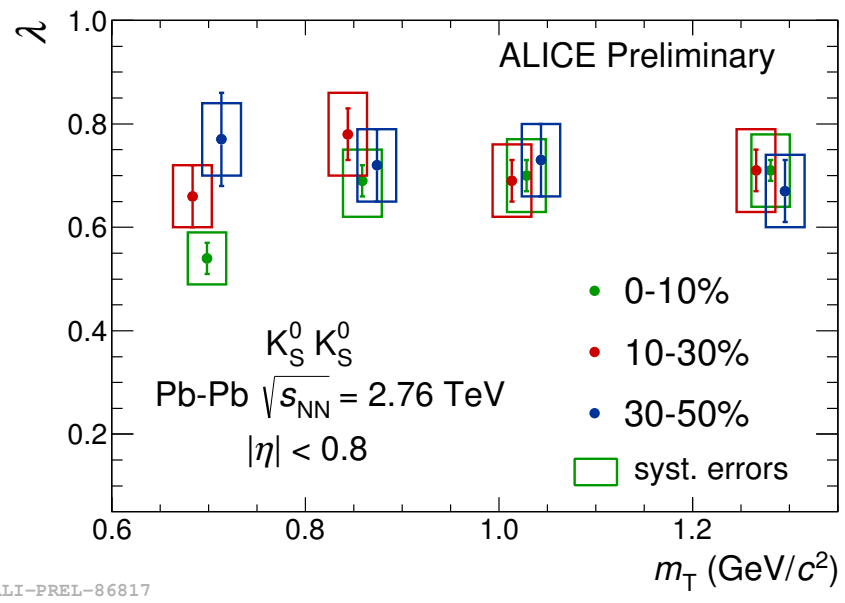

Figure 7.17: 3D $K^0_S K^0_S$ λ vs. M_T for different centrality bins. Statisical (thin lines) and systematic (boxes) errors are shown. The M_T values for 10-30% and 30-50% are shifted slightly for clarity.

predictions match the experimental pion results for R_{out} at all M_T and for R_{side} and R_{long} at low M_T; however, they underpredict the latter two radii at higher M_T. Thus, both the model predictions and the experimental data see different M_T-scalings for R_{out}, whereas the data exhibit a common M_T-scaling for the sideward and longitudinal radii which the model fails to recover due to the underprediction of the pions.

For the outward-sideward ratio, the pion and kaon values are mostly consistent with unity. The HKM predictions show a flat distribution at 1.1 for both species, overpredicting the pion values, which is often the case with hydrodynamical models for this variable, but remaining partially consistent with the kaon values.

Fig. 7.19 shows the 3D λ values vs. M_T for 0-5% central collisions from ALICE $\pi\pi$ [120] and $K^0_S K^0_S$ along with the HKM predictions [125]. The pion "values" are presented as a range, as this was the only information given in [120], which also states that the values increase slightly with M_T. The HKM overpredicts the kaon λ significantly, similar to the 1D analysis. As stated earlier, since the model predictions have no purity issues, one would

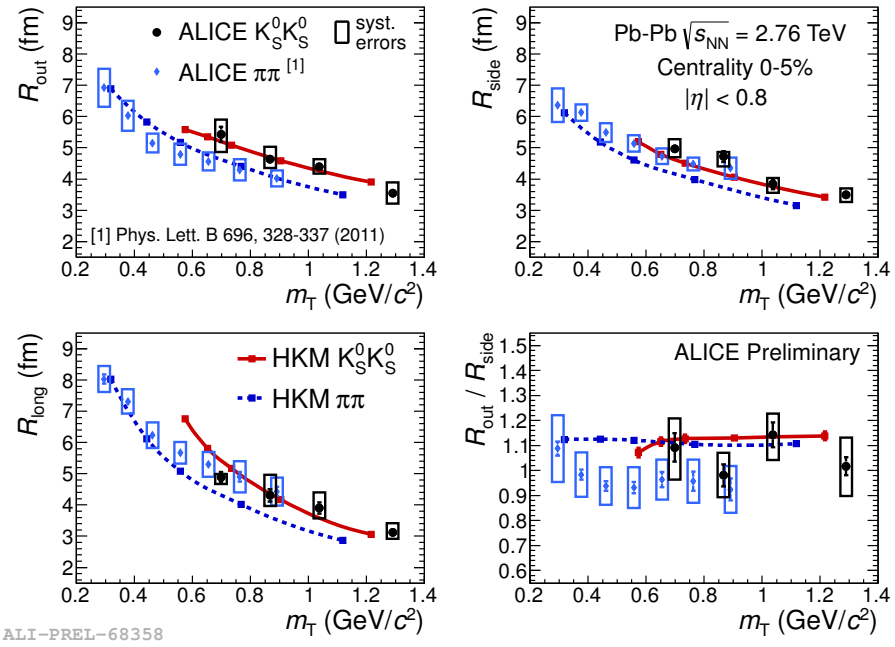

Figure 7.18: 3D LCMS radii vs. M_T for $K^0_S K^0_S$ and $\pi\pi$ from ALICE [120] and HKM [125]. Statisical (thin lines) and systematic (boxes) errors are shown for the ALICE points.

expect the experimental values to indeed be lower; though, with the high purity values from experiment, we would expect only a $\sim 10\%$ drop due to this effect. Also, the inclusion or exclusion of K^* and ϕ meson resonance decay products in the model effects their λ very little, suggesting that resonance contributions do not lead to the differences seen here. We also see that the kaon and pion λ values are similar. However, we do not make any physics messages regarding this as we would not necessarily expect any connection here, especially considering the various contributions that affect λ.

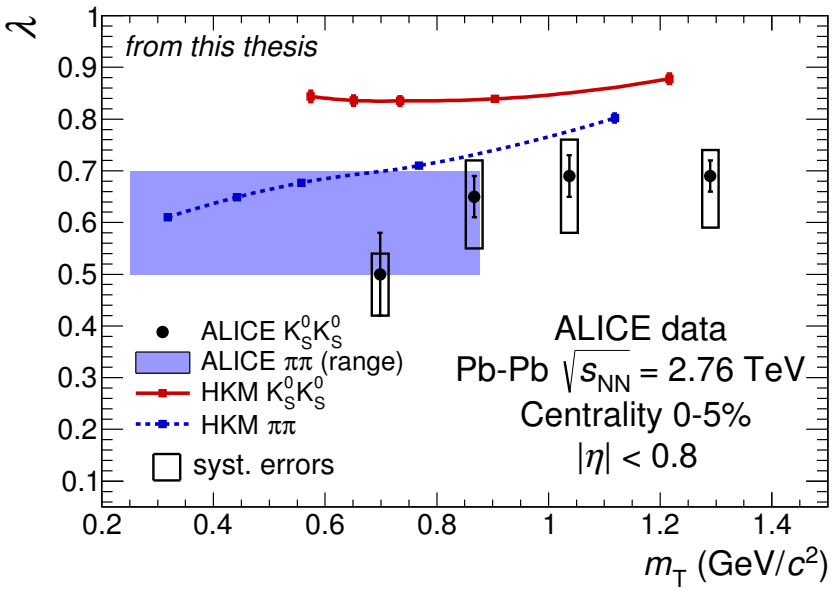

Figure 7.19: 3D λ vs. M_{T} for $K^0_{\mathrm{S}}K^0_{\mathrm{S}}$ and $\pi\pi$ from ALICE [120] and HKM [125]. Statisical (thin lines) and systematic (boxes) errors are shown for the ALICE kaon points. The pion "values" are shown as a range, as this was the information presented in [120].

Chapter 8
Summary

This thesis presented the results of neutral kaon femtoscopy from Pb-Pb collisions at center-of-mass energies $\sqrt{s_{\mathrm{NN}}} = 2.76$ TeV at the LHC measured by the ALICE collaboration. This analysis is the first presentation of $K^0_{\mathrm{S}}K^0_{\mathrm{S}}$ femtoscopy in heavy-ion collisions that is differential in centrality and transverse pair momentum K_{T}. It is also the first presentation of three-dimensional $K^0_{\mathrm{S}}K^0_{\mathrm{S}}$ femtoscopy and the first analysis (that we know of) to include strong final-state interactions in a three-dimensional fitting procedure.

We discussed the single- and two-particle neutral kaon systems, showing that strong final-state interactions have a significant effect on the $K^0\bar{K}^0$ correlation due to the near-threshold $f_0(980)$ and $a_0(980)$ resonances and must be included in the fit function in addition to the usual quantum-statistical Bose-Einstein correlations. The theoretical $K^0_{\mathrm{S}}K^0_{\mathrm{S}}$ correlation function incorporating quantum statistics and strong FSI is calculated using the Lednický-Lyuboshitz analytical model in the 1D analysis and using a Monte Carlo emission simulation combined with a two-particle wavefunction weight calculation in the 3D analysis.

In the 1D analysis, we presented the femtoscopic radius R_{inv} for three centrality bins and four K_{T} bins. The radii decrease with increasing K_{T}, which is expected for expanding sources, and for more peripheral collisions, which reflects the change in size of the collision region. The λ parameter is in the range 0.50-0.75 and agrees with expectations which take into account resonance decay and experimental pair parity considerations. The λ parameter also falls slightly for increasing K_{T}, which we attribute to the fact that the source size in the pair rest frame becomes increasingly less spherical and less able to be characterized

by a one-dimensional Gaussian. The K^0_S radii are consistent with the charged kaon radii within uncertainties, though the neutral kaon values lie systematically above the charged kaon values, and this difference becomes larger for more central collisions. The comparison of $R_{\rm inv}$ for pion, kaons, and protons as a function of pair transverse mass $M_{\rm T}$ does not show a common $M_{\rm T}$-scaling, especially at low $M_{\rm T}$. However, we discussed the expectation that one should not expect such a common scaling in the PRF $R_{\rm inv}$ due to kinematic effects. Comparisons with the HKM model in central collisions show that the predictions match the qualitative trend of the K^0_S radii (λ parameter) while underpredicting (overpredicting) the radius (λ) values.

In the 3D analysis, we also presented the LCMS out-side-long radii, the outward-sideward ratio, and the λ parameter for three centrality bins and four $K_{\rm T}$ bins. The radii decrease with increasing $K_{\rm T}$ and for more peripheral collisions as expected. Comparisons with ALICE pion results show approximately common $M_{\rm T}$-scaling in the sideward and longitudinal radii but significantly different scalings for the outward radius. The K^0_S radii are consistent with HKM predictions for central collisions. The HKM model predicts different $M_{\rm T}$-scalings for pions and kaons in all three radii but underpredicts the pions in the sideward and longitudinal directions. The $R_{\rm out}/R_{\rm side}$ ratio for K^0_S is consistent with unity for all centralities and $M_{\rm T}$ and also with pions and HKM predictions for central collisions. The $M_{\rm T}$ dependence of $R^2_{\rm long}$ was used to extract an average emission proper time of ~ 10 fm/c for K^0_S in central collisions, which is consistent with pion results. The 3D λ parameter is in the range 0.5-0.8 and shows no strong dependence on centrality or $M_{\rm T}$, and HKM predictions significantly overpredict the λ values in central collisions.

References

[1] Toia, A. "Participants and spectators at the heavy-ion fireball". *CERN Courier*, (2013). http://cerncourier.com/cws/article/cern/53089. Cited on page 4.

[2] Glauber, R. *Lectures in Theoretical Physics,* Brittin, W.E. and Dunham, L.G., eds., Volume 1, 1–315. New York: Interscience (1959). Cited on page 4.

[3] Miller, M., Reygers, K., Sanders, S., and Steinberg, P. "Glauber Modeling in High Energy Nuclear Collisions". *Ann. Rev. Nucl. Part. Sci.* **57**, 205–243 (2006), arXiv:nucl-ex/0701025. Cited on page 4.

[4] Collins, J., Soper, D., and Sterman, G. "Factorization of Hard Processes in QCD". *Adv. Ser. Direct. High Energy Phys.* **5**, 1–91 (1988), arXiv:hep-ph/0409313. Cited on page 6.

[5] Craig, R. "Measure of the inclusive jet cross section using the midpoint algorithm in Run II at CDF". PhD thesis, University of Florida, (2006). Cited on page 7.

[6] Shuryak, E. "Theory of Hadronic Plasma". *Zh. Eksp. Teor. Fiz.* **74**, 408–420 (1978). Cited on page 8.

[7] Adams, J. *et al.* [STAR Collaboration]. "Experimental and Theoretical Challenges in the Search for the Quark Gluon Plasma: The STAR Collaboration's Critical Assessment of the Evidence from RHIC Collisions". *Nucl. Phys. A* **757**, 102–183 (2005). Cited on pages 8, 11, 23, and 27.

[8] Adcox, K. *et al.* [PHENIX Collaboration]. "Formation of dense partonic matter in relativistic nucleus-nucleus collisions at RHIC: Experimental evaluation by the PHENIX collaboration". *Nucl. Phys. A* **757**, 184–283 (2005). Cited on pages 8, 11, 23, and 27.

[9] Arsene, I. *et al.* [BRAHMS Collaboration]. "Quark-gluon plasma and color glass condensate at RHIC? The perspective from the BRAHMS experiment". *Nucl. Phys. A* **757**, 1–27 (2005). Cited on pages 8, 23, and 27.

[10] Back, B. *et al.* [PHOBOS Collaboration]. "The PHOBOS perspective on discoveries at RHIC". *Nucl. Phys. A* **757**, 28–101 (2005). Cited on pages 8, 23, and 27.

[11] Heinz, U. "The strongly coupled quark-gluon plasma created at RHIC". *J. Phys. A* **42**, 214003 (2009), arXiv:0810.5529 [nucl-th]. Cited on page 8.

[12] Yagi, K., Hatsuda, T., and Miake, Y. *Quark-Gluon Plasma.* Cambridge University Press, (2005). Cited on pages 8, 9, and 14.

[13] Karsch, F. "Lattice QCD at high temperature and density". *Lect. Notes Phys.* **583**, 209–249 (2002), arXiv:hep-lat/0106019. Cited on page 9.

[14] Nayak, T. "Heavy Ions: Results from the Large Hadron Collider". *Pramana* **79**, 719–735 (2012), arXiv:1201.4264 [nucl-ex]. Cited on page 10.

[15] Aaron, F. *et al.* [H1 and ZEUS Collaborations]. "Combined Measurement and QCD Analysis of the Inclusive ep Scattering Cross Sections at HERA". *JHEP* **1001**, 109 (2010), arXiv:0911.0884 [hep-ex]. Cited on page 10.

[16] Matsui, T. "Dynamical evolution of the quark-gluon plasma and phenomology". *Nucl. Phys. A* **461**, 27–48 (1987). Cited on page 11.

[17] Iancu, E. and Venugopalan, R. "The Color Glass Condensate and High Energy Scattering in QCD". In *Quark-Gluon Plasma 3,* Hwa, R.C. and Wang, X.N., eds., 249. Singapore: World Scientific (2004). Cited on page 11.

[18] Elze, H. and Heinz, U. "Quark-Gluon Transport Theory". *Phys. Rep.* **183**, 81 (1989). Cited on page 11.

[19] Molnar, D. and Gyulassy, M. "New solutions to covariant nonequilibrium dynamics". *Phys. Rev. C* **62**, 054907 (2000). Cited on page 11.

[20] Son, D. and Starinets, A. "Viscosity, Black Holes, and Quantum Field Theory". *Ann. Rev. Nucl. Part. Sci.* **57**, 95–118, arXiv:0704.0240 [hep-th]. Cited on page 12.

[21] Andronic, A., Braun-Munzinger, P., Redlich, K., and Stachel, J. "The statistical model in Pb-Pb collisions at the LHC". *Nucl. Phys. A* **904-905**, 535c–538c (2013), Quark Matter 2012 proceedings. Cited on page 12.

[22] Milano, L. for the ALICE collaboration. "Identified charged hadron production in Pb-Pb collision at the LHC with the ALICE experiment". *Nucl. Phys. A* **904-905**, 531c–534c (2013), Quark Matter 2012 proceedings. Cited on page 12.

[23] Abelev, B. *et al.* [ALICE Collaboration]. "Centrality dependence of π, K, p production in Pb-Pb collisions at $\sqrt{s_{\rm NN}} = 2.76$ tev". *Phys. Rev. C* **88**, 044910 (2013), arXiv:1303.0737 [hep-ex]. Cited on pages 12, 59, and 60.

[24] Feinberg, E. L. "Direct production of photons and dileptons in thermodynamical models of multiple hadron production". *Il Nuovo Cimento A* **34**, 391–412 (1976). Cited on page 13.

[25] Shuryak, E. "Quark-gluon plasma and hadronic production of leptons, photons and psions". *Phys. Lett. B* **78**, 150–153 (1978). Cited on page 13.

[26] Domokos, G. and Goldman, J. "Quark-matter diagnostics". *Phys. Rev. D* **23**, 203–213 (1981). Cited on page 13.

[27] Wilde, M. [ALICE Collaboration]. "Measurement of direct photons in pp and Pb-Pb collisions with ALICE". arXiv:1210.5958 [hep-ex] (2012). Cited on page 13.

[28] Shen, C. *et al.*. "Thermal photons as a quark-gluon plasmas thermometer reexamined". *Phys. Rev. C* **89**, 044910 (2014), arXiv:1308.2440 [nucl-th]. Cited on page 13.

[29] Bjorken, J. "Highly relativistic nucleus-nucleus collisions: the central rapidity region". *Phys. Rev. D* **27**(1), 140–151 (1983). Cited on page 14.

[30] Aamodt, K., *et al.* [ALICE Collaboration]. "Charged-particle multiplicity density at mid-rapidity in central Pb-Pb collisions at $\sqrt{s_{\rm NN}} = 2.76$ TeV". *Phys. Rev. Lett.* **105**, 252301 (2011), arXiv:1011.3916 [nucl-ex]. Cited on page 14.

[31] Krajczar, K., *et al.* [CMS Collaboration]. "Charged hadron multiplicity and transverse energy densities in PbPb collisions from CMS". *J. Phys. G* **38**, 124041 (2011). Cited on page 14.

[32] Baier, R., Schiff, D., and Zakharov, B.G. "Energy Loss in Perturbative QCD". *Annu. Rev. Nucl. Part. Sci.* **50**, 37–69 (2000). Cited on page 14.

[33] Aamodt, K., *et al.* [ALICE Collaboration]. "Suppression of charged particle production at large transverse momentum in central Pb-Pb collisions at $\sqrt{s_{\rm NN}} = 2.76$ TeV". *Phys. Lett. B* **696**, 30–39 (2011). Cited on page 15.

[34] Abelev, B., *et al.* [ALICE Collaboration]. "Measurement of charged jet suppression in Pb-Pb collisions at $\sqrt{s_{\rm NN}} = 2.76$ teV". *JHEP* **2014**(3), 13 (2014), arXiv:1311.0633. Cited on page 16.

[35] Matsui, T. and Satz, H. "J/ψ suppression by quark-gluon plasma formation". *Phys. Lett. B* **178**(4), 416–422 (1986). Cited on page 17.

[36] Manceau, L. "Quarkonium measurements in Pb-Pb and p-Pb collisions with ALICE at the LHC". *EPJ Web of Conferences* **60**, 13002 (2013), arXiv:1307.3098 [nucl-ex]. Cited on page 17.

[37] Rafelski, J. and Müller, B. "Strangeness production in the Quark-Gluon Plasma". *Phys. Rev. Lett.* **48**, 1066–1070 (1982). Cited on page 18.

[38] Elia, D. *et al.,* [ALICE Collaboration]. "Strangeness production in ALICE". *J. Phys.: Conf. Ser.* **455**, 012005 (2013), from International Workshop on Discovery Physics at the LHC (Kruger 2012). Cited on page 18.

[39] Heinz, U. and Kolb, P. "Early thermalization at RHIC". *Nuc. Phys. A* **702**, 269c–280c (2002). Cited on page 19.

[40] ALICE Collaboration. "Elliptic flow of identified hadrons in Pb-Pb collisions at $\sqrt{s_{\rm NN}} = 2.76$ TeV". CERN-PH-EP-2014-104, arXiv:1405.4632 [nucl-ex] (2014). Cited on page 19.

[41] Snellings, R. "Collective Expansion at the LHC: selected ALICE anisotropic flow measurements". arXiv:1408.2532 [nucl-ex] (2014). Cited on pages 19 and 20.

[42] Voloshin, S. and Zhang, Y. "Flow Study in Relativistic Nuclear Collisions by Fourier Expansion of Azimuthal Particle Distributions". *Z. Phys. C* **70**, 665–672 (1996). Cited on page 19.

[43] Aamodt, K. *et al.* [ALICE Collaboration]. "Elliptic flow of charged particles in Pb-Pb collisions at 2.76 TeV". *Phys. Rev. Lett.* **105**, 252302 (2010), arXiv:1011.3914 [nucl-ex]. Cited on page 20.

[44] Bilandzic, A. "Anisotropic flow of charged particles at$\sqrt{s_{\mathrm{NN}}} = 2.76$ TeV measured with the ALICE detector". *J. Phys. G* **38**, 124052 (2011), Quark Matter 2011 proceedings, arXiv:1106.6209 [nucl-ex]. Cited on page 20.

[45] Aamodt, K. *et al.* [ALICE Collaboration]. "Higher order anisotropic flow meaurements of charged particles in Pb-Pb collisions at 2.76 TeV". *Phys. Rev. Lett.* **107**, 032301 (2011), arXiv:1105.3865. Cited on page 20.

[46] Evans, L. and Bryant, P. (eds.). "LHC machine". *JINST* **3**(08), S08001 (2008). Cited on pages 22 and 25.

[47] Rubbia, C. "Future hadron collider: the LHC". *AIP Conf. Proc.* **272**, 321–333 (1992), CERN-PPE-92-160. Cited on page 22.

[48] "Building the LHC". http://timeline.web.cern.ch/timelines/Building-the-LHC?page=1. Accessed: 24 Sept 2014. Cited on page 23.

[49] "Interim summary report on the analysis of the 19 September 2008 incident at the LHC", (2008). CERN Document EDMS 973073. Cited on page 23.

[50] CERN press office. "The LHC sets new world record". Press release, (2009). http://press.web.cern.ch/press-releases/2009/11/lhc-sets-new-world-record. Cited on page 23.

[51] "LHC Smashes Highest Man-Made Temperature Record". http://news.discovery.com/space/alice-topples-record-temperatures-set-by-phenix-120821.htm, (2012). Accessed: 3 Dec 2014. Cited on page 23.

[52] CERN press office. "LHC sets world record beam intensity". Press release, (2011). http://press.web.cern.ch/press-releases/2011/04/lhc-sets-world-record-beam-intensity. Cited on page 23.

[53] Aad, G. *et al.* [ATLAS Collaboration]. "Observation of a new particle in the search for the Standard Model Higgs boson with the ATLAS detector at the LHC". *Phys. Lett. B* **716**, 1–29 (2012). Cited on page 23.

[54] Chatrchyan, S. *et al.* [CMS Collaboration]. "Observation of a new boson at a mass of 125 GeV with the CMS experiment at the LHC". *Phys. Lett. B* **716**, 30–61 (2012). Cited on page 23.

[55] Nobel Media AB 2014. "The Nobel Prize in Physics 2013". http://www.nobelprize.org/nobel_prizes/physics/laureates/2013 (2014). Cited on page 23.

[56] Lamont, M. "The LHC's first long run". *CERN Courier*, (2013). http://cerncourier.com/cws/article/cern/54381. Cited on page 23.

[57] TEVNPH Working Group. "Updated Combination of CDF and D0 Searches for Standard Model Higgs Boson Production with up to 10.0 fb of Data". FERMILAB-CONF-12-318-E, arXiv:1207.0449 [hep-ex] (2012). Cited on page 23.

[58] Lamont, M. "Status of the LHC". *Journal of Physics: Conference Series* **455**(1), 012001 (2013). Cited on page 23.

[59] Salgado, C. (ed.). "Proton-Nucleus Collisions at the LHC: Scientific Opportunities and Requirements". CERN-PH-TH/2011-119, LHC-Project-Report-1181, arXiv:1105.3919 [hep-ph] (2011). Cited on page 24.

[60] ATLAS Collaboration. "Letter of Intent for the Phase-I Upgrade of the ATLAS Experiment". Technical Report CERN-LHCC-2011-012, LHCC-I-020, CERN, (2011). Cited on page 24.

[61] CMS Collaboration. "Technical proposal for the upgrade of the CMS detector through 2020". Technical Report CERN-LHCC-2011-006, LHCC-P-004, CERN, (2011). Cited on page 24.

[62] Musa, L. and Safarik, K. for the ALICE Collaboration. "Letter of Intent for the Upgrade of the ALICE Experiment". Technical Report CERN-LHCC-2012-012. LHCC-I-022, CERN, (2012). Cited on page 24.

[63] "TE-EPC-LPC in LHC". http://te-epc-lpc.web.cern.ch/te-epc-lpc/machines/lhc/general.stm (2012). Cited on page 25.

[64] Benedikt, M., Collier, P., Mertens, V., Poole, J., and Schindl, K. "LHC Design Report, Vol III: The Injector Chain". CERN, (2004). CERN-2004-003. Cited on page 24.

[65] Aad, G. *et al.* [ATLAS Collaboration]. "The ATLAS Experiment at the CERN Large Hadron Collider". *JINST* **3**(08), S08003 (2008). Cited on page 26.

[66] Chatrchyan, S. *et al.* [CMS Collaboration]. "The CMS experiment at the CERN LHC". *JINST* **3**(08), S08004 (2008). Cited on page 26.

[67] Aamodt, K. *et al.* [ALICE Collaboration]. "The ALICE experiment at the CERN LHC". *JINST* **3**(08), S08002 (2008). Cited on pages 26, 27, 29, 30, and 72.

[68] Alves, Jr., A.A. *et al.* [LHCb Collaboration]. "The LHCb Detector at the LHC". *JINST* **3**(08), S08005 (2008). Cited on page 26.

[69] Anelli, G. *et al.* [TOTEM Collaboration]. "The TOTEM Experiment at the CERN Large Hadron Collider". *JINST* **3**(08), S08007 (2008). Cited on page 26.

[70] Adriani, O. *et al.* [LHCf Collaboration]. "The LHCf detector at the CERN Large Hadron Collider". *JINST* **3**(08), S08006 (2008). Cited on page 26.

[71] Pinfold, J. *et al.* [MoEDAL Collaboration]. "Technical Design Report of the MoEDAL Experiment". Technical Report CERN-LHCC-2009-006. MoEDAL-TDR-001, CERN, (2009). Cited on page 26.

[72] ALICE Collaboration. "ALICE: Technical proposal for A Large Ion Collider Experiment at the CERN LHC". Technical Report CERN-LHCC-95-71, LHCC-P-3, CERN, (1995). Cited on pages 26 and 27.

[73] Cabibbio, N. and Parisi, G. "Exponential hadronic spectrum and quark liberation". *Phys. Lett. B* **59**, 67–69 (1975). Cited on page 27.

[74] Shuryak, E. "Quantum chromodynamics and the theory of superdense matter". *Phys. Rept.* **61**(2), 71–158 (1980). Cited on page 27.

[75] Heinz, U. and Jacob, M. "Evidence for a New State of Matter: An Assessment of the Results from the CERN Lead Beam Programme". arxiv:nucl-th/0002042 (2000). Cited on page 27.

[76] Carminati, F. *et al.* [ALICE Collaboration]. "ALICE: Physics Performance Report, Volume I". *J. Phys. G: Nucl. Part. Phys.* **30**, 1517–1763 (2004). Cited on page 27.

[77] ALICE Collaboration. "ALICE Inner Tracking System (ITS): Technical Design Report". Technical Report CERN-LHCC-99-012, CERN, (1999). https://edms.cern.ch/file/398932/1. Cited on pages 27 and 29.

[78] ALICE Collaboration. "ALICE Time Projection Chamber: Technical Design Report". Technical Report CERN-LHCC-2000-001, CERN, (2000). http://cdsweb.cern.ch/record/451098. Cited on pages 27 and 32.

[79] ALICE Collaboration. "ALICE Transition-Radiation Detector: Technical Design Report". Technical Report CERN-LHCC-2001-021, CERN, (2001). http://cdsweb.cern.ch/record/519145. Cited on page 27.

[80] ALICE Collaboration. "ALICE Time-Of-Flight System (TOF): Technical Design Report". Technical Report CERN-LHCC-2000-012, CERN, (2000). http://cdsweb.cern.ch/record/430132. Cited on pages 27 and 33.

[81] ALICE Collaboration. "ALICE high-momentum particle identification: Technical Design Report". Technical Report CERN-LHCC-98-019, CERN, (1998). http://cdsweb.cern.ch/record/381431. Cited on page 28.

[82] ALICE Collaboration. "Technical design report of the photon spectrometer". Technical Report CERN-LHCC-99-004, CERN, (1999). http://cdsweb.cern.ch/record/381432. Cited on page 28.

[83] ALICE Collaboration. "ALICE electromagnetic calorimeter: addendum to the ALICE technical proposal". Technical Report CERN-LHCC-2006-014, CERN, (2006). http://cdsweb.cern.ch/record/932676. Cited on page 28.

[84] ALICE Collaboration. "ALICE Zero-Degree Calorimeter (ZDC): Technical Design Report". Technical Report CERN-LHCC-99-005, CERN, (1999). http://cdsweb.cern.ch/record/381433. Cited on page 28.

[85] ALICE Collaboration. "ALICE Time Photon Multiplicity Detector (PMD): Technical Design Report". Technical Report CERN-LHCC-99-032, CERN, (1999). http://cdsweb.cern.ch/record/451099. Cited on page 28.

[86] ALICE Collaboration. "ALICE forward detectors: FMD, T0 and V0: Technical Design Report". Technical Report CERN-LHCC-2004-025, CERN, (2004). http://cdsweb.cern.ch/record/781854. Cited on pages 28, 29, and 34.

[87] ALICE Collaboration. "ALICE dimuon forward spectrometer: Technical Design Report". Technical Report CERN-LHCC-99-022, CERN, (1999). http://cdsweb.cern.ch/record/401974. Cited on page 29.

[88] Fernández, A. *et al.* [ALICE Collaboration]. "ACORDE, a cosmic ray detector for ALICE". *Nucl. Instrum. Meth.* ***A*** **572**, 102 (2007). Cited on page 29.

[89] Zampolli, C. [ALICE Collaboration]. "Particle Identification with the ALICE detector at the LHC". In *Physics at LHC 2012*. (2012). Cited on page 30.

[90] Contin, G. "Performance of the present ALICE Inner Tracking System and the studies for the upgrade". *JINST* **7**, C06007 (2012). Cited on page 31.

[91] Alme, J. *et al.* [ALICE Collaboration]. "The ALICE TPC, a large 3-dimensional tracking device with fast readout for ultra-high multiplicity events". arXiv:1001.1950v1 [physics.ins-det] (2010). Cited on page 32.

[92] Alici, A. "Status and performance of the ALICE MRPC-based Time-Of-Flight detector". *JINST* **7**, P10024 (2012). Cited on page 33.

[93] Abelev, B. *et al.* [ALICE Collaboration]. "Performance of the ALICE Experiment at the CERN LHC". *Int. J. Mod. Phys. A* **29**, 1430044 (2014), arXiv:1402.4476. Cited on pages 33, 69, 74, and 75.

[94] Abelev, B. *et al.* [ALICE Collaboration]. "Centrality determination of Pb-Pb collisions at $\sqrt{s_{\rm NN}} = 2.76$ TeV with ALICE". *Phys. Rev. C* **88**, 044909 (2013), arXiv:1301.4361 [nucl-ex]. Cited on pages 34, 69, and 70.

[95] ALICE Collaboration. "Performance of the ALICE VZERO system". *JINST* **8**, P10016 (2013). Cited on page 34.

[96] Hanbury Brown, R. and Twiss, R. "A new type of interferometer for use in radio astronomy". *Phil. Mag.* **45**, 663–682 (1954). Cited on page 35.

[97] Hanbury Brown, R. and Twiss, R. "Correlation between Photons in two Coherent Beams of Light". *Nature* **177**, 27–29 (1956). Cited on page 35.

[98] Humanic, T. "Hanbury-Brown-Twiss Interferometry with Identical Bosons in Relativistic Heavy Ion Collisions: Comparisons with Hadronic Scattering Models". *Int. J. Mod. Phys. E* **15**, 197–236 (2006), arXiv:nucl-th/0510049. Cited on page 36.

[99] Goldhaber, G., Goldhaber, S., Lee, W., and Pais, A. "Influence of Bose-Einstein Statistics on the Antiproton-Proton Annihilation Process". *Phys. Rev.* **120**, 300 (1960). Cited on page 36.

[100] Heinz, U. "Concepts of heavy-ion physics", (2004). CERN-2004-001-D; arXiv:hep-ph/0407360. Cited on pages 38 and 48.

[101] Heinz, U. and Jacak, B. "Two-Particle Correlations in Relativistic Heavy-Ion Collisions". *Annu. Rev. Nucl. Part. Sci* **49**, 529–579 (1999), arXiv:nucl-th/9902020. Cited on pages 38, 47, and 124.

[102] Lisa, M., Pratt, S., Soltz, R., and Wiedemann, U. "Femtoscopy in Relativistic Heavy Ion Collisions: Two Decades of Progress". *Annu. Rev. Nucl. Part. Sci.* **55**, 357–402 (2005), arXiv:nucl-ex/0505014. Cited on page 38.

[103] Kopylov, G. and Podgoretsky, M. *Sov. J. Nucl. Phys.* **15**, 219 (1972). Cited on page 38.

[104] Kopylov, G. and Podgoretsky, M. *Sov. J. Nucl. Phys.* **18**, 336 (1973). Cited on page 38.

[105] Kopylov, G. and Podgoretsky, M. *Sov. J. Nucl. Phys.* **19**, 215 (1974). Cited on page 38.

[106] Anchishkin, D., Heinz, U., and Renk, O. "Final state interactions in two-particle interferometry". *Phys. Rev. C* **57**(3), 1428–1439 (1998). Cited on page 39.

[107] Heinz, U. "Measuring the size of things in the universe: HBT interferometry and heavy ion physics", *Proceedings CRIS'98,* Costa, S. *et al.*, eds., 66–94. World Scientific, Singapore (1998). arXiv:hep-ph/9806512. Cited on pages 39 and 40.

[108] Akkelin, S. and Sinyukov, Y. "The HBT-interferometry of expanding sources". *Phys. Lett. B* **356**, 525–530 (1995). Cited on pages 40 and 43.

[109] Koonin, S. "Proton pictures of high-energy collisions". *Phys. Lett. B* **70**(1), 43–47 (1977). Cited on page 42.

[110] Pratt, S., Csörgő, T., and Zimányi, J. "Detailed predictions for two-pion correlations in ultrarelativistic heavy-ion collisions". *Phys. Rev. C* **42**(6), 2646 (1990). Cited on page 42.

[111] Lednický, R. and Lyuboshitz, V. "Final state interaction effect of pairing correlations between particles with small relative momenta". *Sov. J. Nucl. Phys.* **35**, 770 (1982). Cited on pages 42 and 43.

[112] Sinyukov, Y. *et al.*. "Coulomb corrections for interferometry analysis of expanding hadron systems". *Phys. Lett. B* **432**, 248–257 (1998). Cited on page 42.

[113] Bowler, M. "Coulomb corrections to Bose-Einstein corrections have greatly exaggerated". *Phys. Lett. B* **270**, 69–74 (1991). Cited on page 42.

[114] Chapman, S., Nix, J., and Heinz, U. "Extracting source parameters from Gaussian fits to two-particle correlations". *Phys. Rev. C* **52**(5), 2694 (1995). Cited on page 43.

[115] Heinz, U. *et al.*. "Lifetimes and sizes from two-particle correlation functions". *Phys. Lett. B* **382**, 181–188 (1996). Cited on page 43.

[116] Bertsch, G., Danielewicz, P., and Herrmann, M. "Hanbury-Brown–Twiss analysis in a solvable model". *Phys. Rev. C* **49**, 442 (1994). Cited on page 44.

[117] Herrmann, M. and Bertsch, G. "Source dimensions in ultrarelativistic heavy-ion collisions". *Phys. Rev. C* **51**, 328 (1995). Cited on pages 44 and 48.

[118] Fowler, G., Stelte, N., and Weiner, R. "Condensates and Bose-Einstein correlations". *Nucl. Phys. A* **319**, 349–363 (1979). Cited on pages 46 and 53.

[119] Abelev, B. *et al.* [ALICE Collaboration]. "Two- and three-pion quantum statistics correlations in Pb-Pb collisions at $\sqrt{s_{\rm NN}}$ = 2.76 TeV at the CERN Large Hadron Collider". *Phys. Rev. C* **89**, 024911 (2014), arXiv:1310.7808 [nucl-ex]. Cited on pages 46 and 53.

[120] Aamodt, K. *et al.* [ALICE Collaboration]. "Two-pion Bose-Einstein correlations in central PbPb collisions at $\sqrt{s_{\rm NN}}$ = 2.76 TeV". *Phys. Lett. B* **696**, 328–337 (2011), arXiv:1012.4035 [nucl-ex]. Cited on pages 48, 124, 126, 127, 128, and 129.

[121] Pratt, S. "Resolving the HBT Puzzle in Relativistic Heavy Ion Collisions". *Phys. Rev. Lett.* **102**, 232301 (2009), arXiv:0811.3363 [nucl-th]. Cited on page 48.

[122] Makhlin, A. and Sinyukov, Y. "Hydrodynamics of Hadron Matter Under Pion Interferometric Microscope". *Z. Phys. C* **39**, 69 (1988). Cited on pages 48, 49, and 113.

[123] Sinyukov, Y. "Hanbury Brown/Twiss Correlations for Expanding Hadron and Quark - Gluon Matter". *Nucl. Phys. A* **498**, 151C–160C (1989). Cited on pages 49 and 113.

[124] Kisiel, A., Galazyn, M., and Bozek, P. "Pion, kaon, and proton femtoscopy in Pb–Pb collisions at $\sqrt{s_{\rm NN}}$ = 2.76 TeV modeled in 3+1D hydrodynamics". Preprint: arXiv:1409.4571 [nucl-th] (2014). Cited on pages 49, 113, 114, and 122.

[125] Shapoval, V., Braun-Munzinger, P., Karpenko, I., and Sinyukov, Y. "Femtoscopy correlations of kaons in Pb+Pb collisions, at LHC within hydrokinetic model". *Nucl. Phys. A* **929**, 1–8 (2014). Cited on pages 49, 112, 114, 115, 124, 126, 127, 128, and 129.

[126] Adamczyk, L. *et al.*, [STAR Collaboration]. "Beam energy dependent two-pion interferometry and the freeze-out eccentricity of pions in heavy ion collisions at STAR". Publication pending, arXiv:1403.4972 [nucl-ex] (2014). Cited on page 50.

[127] Loggins, V. and Voloshin, S. for the ALICE Collaboration. "Azimuthally differential pion femtoscopy in Pb-Pb collisions at $\sqrt{s_{\rm NN}}$ = 2.76 TeV with ALICE at the LHC". Paper in progress (2014). Cited on page 51.

[128] Kisiel, A. "Nonidentical-particle femtoscopy at $\sqrt{s_{\rm NN}}$ = 200 GeV in hydrodynamics with statistical hadronization". *Phys. Rev. C* **81**, 064906 (2010). Cited on page 52.

[129] Brown, D. and Danielewicz, P. "Imaging of sources in heavy-ion reactions". *Phys. Lett. B* **398**, 252–258 (1997). Cited on page 52.

[130] Shapoval, V., Sinyukov, Y., and Karpenko, I. "Emission source functions in heavy ion collisions". *Phys. Rev. C* **88**, 064904 (2014), arXiv:1308.6272 [hep-ph]. Cited on page 52.

[131] Kisiel, A., Zbroszczyk, H., and Szymanski, M. "Extracting baryon-antibaryon strong interaction potentials from p$\bar{\Lambda}$ femtoscopic correlation function". *Phys. Rev. C* **89**, 054916 (2014), arXiv:1403.0433 [nucl-th]. Cited on page 53.

[132] Heinz, U. and Zhang, Q. "What can we learn from three-pion interferometry?". *Phys. Rev. C* **56**, 426 (1997). Cited on page 53.

[133] Lednický, R. and Lyuboshitz, V. "Effect of the final-state interaction on pairing correlations of particles with small relative momenta". *Sov. J. Nucl. Phys.* **35**, 770 (1982). Cited on pages 55, 59, and 63.

[134] Bekele, S. and Lednicky, R. "Neutral kaon correlations in $\sqrt{s_{\rm NN}}$ = 200 GeV Au+Au collisions at RHIC". *Braz. J. Phys.* **37**(3A), 994 (2007). Cited on pages 55, 58, and 146.

[135] Gell-Mann, M. and Pais, A. "Behavior of Neutral Particles under Charge Conjugation". *Phys. Rev.* **97**, 1387 (1955). Cited on pages 55 and 56.

[136] Christenson, J. *et al.*. "Evidence for the 2π Decay of the K_2^0 Meson". *Phys. Rev. Lett.* **13**, 138 (1964). Cited on page 56.

[137] Yao, W. *et al.* (Particle Data Group). "Review of Particle Physics". *J. Phys. G: Nucl. Part. Phys.* **33**, 1 (2006). Cited on pages 57 and 73.

[138] Alexander, G. "Bose-Einstein and Fermi-Dirac interferometry in particle physics". *Rep. Prog. Phys.* **66**, 481 (2003). Cited on page 57.

[139] Lednicky, R. "Finite-size effects on two-particle production in continuous and discrete spectrum". *Phys. Part. Nucl.* **40**, 307–352 (2009), arXiv:nucl-th/0501065. Cited on pages 58 and 146.

[140] Martin, A., Ozmutlu, E., and Squires, E. "The $\pi\pi$ and $K\bar{K}$ amplitudes, the S* and the quark structure of 0^{++} resonances". *Nucl. Phys. B* **121**, 514–530 (1977). Cited on pages 58, 59, and 63.

[141] Antonelli, A. [KLOE Collaboration]. "Radiative phi decays". *eConf* **C020620**, THAT06 (2002), arXiv:hep-ex/029069. Cited on pages 59, 63, 106, 107, 108, 109, 119, 120, 121, and 122.

[142] Achasov, N. and Gubin, V. "Analysis of the nature of the $\vec{\varphi}\gamma\pi\eta$ and $\vec{\varphi}\gamma\pi^0\pi^0$ decays". *Phys. Rev. D* **63**, 094007 (2001). Cited on pages 59 and 63.

[143] Achasov, N. and Kiselev, A. "New analysis of the KLOE data on the $\vec{\varphi}\eta\pi^0\gamma$ decay". *Phys. Rev. D* **68**, 014006 (2003). Cited on pages 59 and 63.

[144] Ananthanarayan, B., Colangelo, G., Gasser, J., and Leutwyler, H. "Roy equation analysis of pi pi scattering". *Phys. Rept.* **353**, 207–279 (2001), arXiv:hep-ph/0005297. Cited on page 59.

[145] Cooper, A. *et al.* [Bombay-CERN-Collège de France-Madrid Collaboration]. "A study of $K\bar{K}$ correlations in $\bar{p}p$ annihilations at 0.76 GeV/c". *Nucl. Phys. B* **139**, 45–60 (1978). Cited on page 64.

[146] Acton, P. *et al.* [OPAL Collaboration]. "A study of $K^0_S K^0_S$ Bose-Einstein correlations in hadronic Z^0 decays". *Phys. Lett. B* **298**, 456–468 (1993). Cited on page 64.

[147] Jacholkowski, A. for the WA97 Collaboration. "Di-V^0 events in Pb-Pb collisions at 158 A GeV/c". *J. Phys. G: Nucl. Part. Phys.* **25**, 423 (1999). Cited on pages 64 and 65.

[148] Abelev, B. *et al.* [STAR Collaboration]. "Neutral Kaon Interferometry in Au+Au collisions at$\sqrt{s_{\rm NN}}$ = 200 GeV". *Phys. Rev. C* **74**, 054902 (2006), arXiv:nucl-ex/0608012. Cited on pages 64 and 65.

[149] Abelev, B. *et al.* [ALICE Collaboration]. "$K^0_S K^0_S$ correlations in pp collisions at $\sqrt{s}$ = 7 TeV from the LHC ALICE experiment". *Phys. Lett. B* **717**, 151–161 (2012), arXiv:1206.2056. Cited on pages 64 and 66.

[150] Root data analysis framework. http://root.cern.ch/drupal. Cited on page 68.

[151] Alice off-line project. http://aliweb.cern.ch/Offline/. Cited on page 68.

[152] Wang, X. and Gyulassy, M. "HIJING: A Monte Carlo model for multiple jet production in pp, pA, and AA collisions". *Phys. Rev. D* **44**, 3501 (1991). Cited on page 68.

[153] GEANT - Detector Description and Simulation Tool. http://wwwasd.web.cern.ch/wwwasd/geant/. CERN Program Library Long Writeup W5013. Cited on page 68.

[154] Alessandro, B. *et al.* [ALICE Collaboration]. "ALICE: Physics Performance Report, Volume II". *J. Phys. G: Nucl. Part. Phys.* **32**, 1295 (2006). Cited on page 71.

[155] Blum, W., Riegler, W., and Rolandi, L. *Particle Detection with Drift Chambers,* 2nd ed.,. Springer-Verlag, (2008). Cited on page 73.

[156] Carrazza, S. "Strange particle production in heavy-ion collisions with the ALICE experiment at CERN LHC". Master's thesis, Université de Lyon, Lyon, France, (2011). Cited on page 77.

[157] James, F. and Roos, M. "Minuit - a system for function minimization and analysis of the parameter errors and correlations". *Comput. Phys. Commun.* **10**(6), 343–367 (1975). Cited on page 95.

[158] Ahle, L. *et al.*, [E-802 Collaboration]. "System, centrality, and transverse mass dependence of two-pion correlation radii in heavy ion collisions at 11.6A and 14.6A GeV/c". *Phys. Rev. C* **66**, 054906 (2002). Cited on page 97.

[159] Abelev, B. *et al.* [ALICE Collaboration]. "Elliptic flow of identified hadrons in Pb-Pb collisions at$\sqrt{s_{\rm NN}}$ = 2.76 TeV". Preprint: CERN-PH-EP-2014-104, arXiv:1405.4632 [nucl-ex] (2014). Cited on pages 110 and 114.

[160] Chojnacki, M., Kisiel, A., Florkowski, W., and Broniowski, W. "THERMINATOR 2: THERMal heavy IoN generATOR 2". *Comput. Phys. Commun.* **183**, 746–773 (2012), arXiv:1102.0273 [nucl-th]. Cited on page 112.

[161] Kisiel, A., Florkowski, W., Broniowski, W., and Pluta, J. "Femtoscopy in hydrodynamics-inspired models with resonances". *Phys. Rev. C* **73**, 064902 (2006). Cited on page 115.

[162] Lednický, R., Lyuboshitz, V., and Lyuboshitz, V. "Final-state interaction in multichannel quantum systems and pair correlations of nonidentical and identical particles at low relative velocities". *Phys. At. Nucl.* **61**, 2950 (1998). Cited on pages 144 and 146.

Appendix A

Corrections to the 1D $K^0_S K^0_S$ correlation function

A.1 Effect of the inelastic $K^+K^- \to K^0\bar{K}^0$ transition

For the FSI effect on particle correlations to be significant, the particles must be moving with slow relative motion, which means the sums of the masses in the entrance and exit channels of the interaction must be similar. Therefore, the $K^0\bar{K}^0$ correlation should include the effect of both the elastic transition $K^0\bar{K}^0 \to K^0\bar{K}^0$ as well as the inelastic transition $K^+K^- \to K^0\bar{K}^0$. Due to isospin considerations, we assume that the particles in both channels are produced with the same probability, so the correlation function will be a sum of the $\vec{r}^*$-averaged squares of the wave functions $\Psi^{11}_{-\vec{k}^*}(\vec{r}^*)$ and $\Psi^{21}_{-\vec{k}^*}(\vec{r}^*)$ describing the elastic and inelastic transitions, respectively. Note also that since the solution of the scattering problem (Eq. 5.7) flips the time direction (hence, the $-\vec{k}^*$ subscript), we treat $K^0\bar{K}^0$ ($\equiv 1$) as the entrance channel and K^+K^- ($\equiv 2$) as the exit channel.

The s-wave dominated inelastic transition wavefunction is given by [162]

$$\Psi^{21}_{-\vec{k}^*}(\vec{r}^*) = f_c^{21}(k^*)\sqrt{\frac{m_{K^+}}{m_{K^0}}}\frac{\tilde{G}(\rho_2,\eta_2)}{r^*}\,, \tag{A.1}$$

where

- $\rho_2 = k_2^* r^*$, where $k_2^* = \sqrt{\frac{m_{K^+}}{m_{K^0}}k^{*2} + 2m_{K^+}(m_{K^+} - m_{K^0})}$ is the K^+ momentum in the PRF
- $\eta_2 = \frac{1}{k_2^* a_2}$, where $a_2 = \frac{1}{2m_{K^+}e^2} = -109.6$ fm is the K^+K^- Bohr radius

- $f_c^{21}(k^*)$ is the s-wave transition amplitude renormalized by the Coulomb interaction in the K^+K^- channel
- $\tilde{G}(\rho,\eta) = \sqrt{A_c(\eta)}[G_0(\rho,\eta) + iF_0(\rho,\eta)]$ is the combination of the singular and regular s-wave Coulomb functions G_0 and F_0
- $A_c(\eta) = \dfrac{2\pi\eta}{\exp(2\pi\eta) - 1}$ is the Coulomb penetration factor, i.e. Gamow factor.

The scattering amplitudes are now given by the 2×2 matrix

$$\hat{f}_c = \left(\hat{K}^{-1} - i\hat{k}_c\right)^{-1} . \tag{A.2}$$

$\hat{K}$ is a symmetric matrix in the channel representation, represented through the inverse diagonal elements K_I^{-1} of the $\hat{K}$-matrix in the representation of total isospin I

$$(\hat{K}^{-1})^{11} = (\hat{K}^{-1})^{22} = \frac{1}{2}[K_0^{-1} + K_1^{-1}] , \tag{A.3}$$

$$(\hat{K}^{-1})^{21} = (\hat{K}^{-1})^{12} = \frac{1}{2}[K_0^{-1} - K_1^{-1}] . \tag{A.4}$$

K_I^{-1} are assumed to be dominated by the f_0 and a_0 resonances for $I = 0$ and 1, giving

$$K_I^{-1} = (m_{\mathrm{r}}^2 - s - ik'_{\mathrm{r}}\gamma'_{\mathrm{r}})/\gamma_{\mathrm{r}}; . \tag{A.5}$$

$\hat{k}_c$ is a diagonal matrix in the channel representation:

$$k_c^{11} = k^* , \tag{A.6}$$

$$k_c^{22} = A_c(\eta_2)k_2^* - \frac{2ih(\eta_2)}{a_2} , \tag{A.7}$$

where $h(\eta) = \frac{1}{2}[\psi(i\eta) - \psi(-i\eta) - \ln\eta^2]$ using the di-gamma function $\psi(z) = \Gamma'(z)/\Gamma(z)$. The scattering amplitude for the elastic $1 \to 1$ transition in Eqs. 5.7 and 5.12 is then replaced by f_c^{11}.

Fig. A.1 shows the effect of the inclusion of the 2nd (inelastic) channel on the $K_{\mathrm{S}}^0 K_{\mathrm{S}}^0$ correlation function. One can see that the effect is quite small for the larger radii of high-energy heavy-ion collisions and grows with decreasing radii. While the correction to the FSI contribution can become significant, the presence of the large Bose-Einstein enhancement

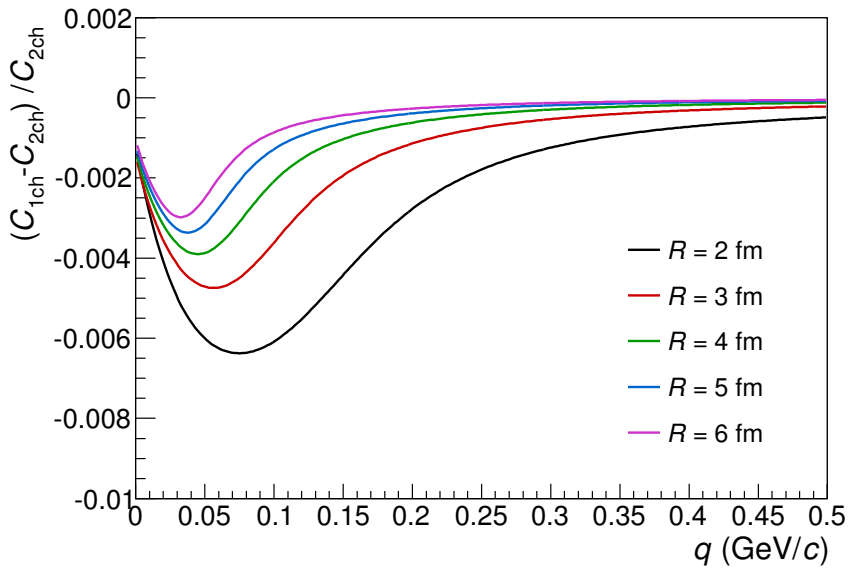

Figure A.1: Correction factor from the inclusion of the inelastic 2nd-channel FSI transition. $C_{2\text{ch}}$ is the $K^0_S K^0_S$ correlation function with both FSI channels, and $C_{1\text{ch}}$ is with only the elastic transition (both are without the deviation correction of Eq. A.8).

makes the correction to the full correlation function even less significant.

A.2 Deviation of FSI wavefunction in inner region

One should also correct for the deviation of the spherical waves from the true scattered waves in the inner region of the short-range potential. In other words, Eq. A.1 only holds outside of the range of the strong interaction potential. This correction can be written as [134, 139, 162]

$$\Delta C_{K\bar{K}} = -\frac{1}{2\sqrt{\pi}R^3}\left[|f_c^{11}|^2 d_0^{11} + |f_c^{21}|^2 d_0^{22} + 2\mathcal{R}(f_c^{11} f_c^{21*}) d_0^{21}\right] , \tag{A.8}$$

where $d_0^{ij} = 2\mathcal{R}[d(\hat{K}^{-1})^{ij}/dk^{*2}]$. Fig. A.2 shows this correction effect for various radii. It is comparable to the 2nd-channel correction and has only a very small effect on the full correlation function.

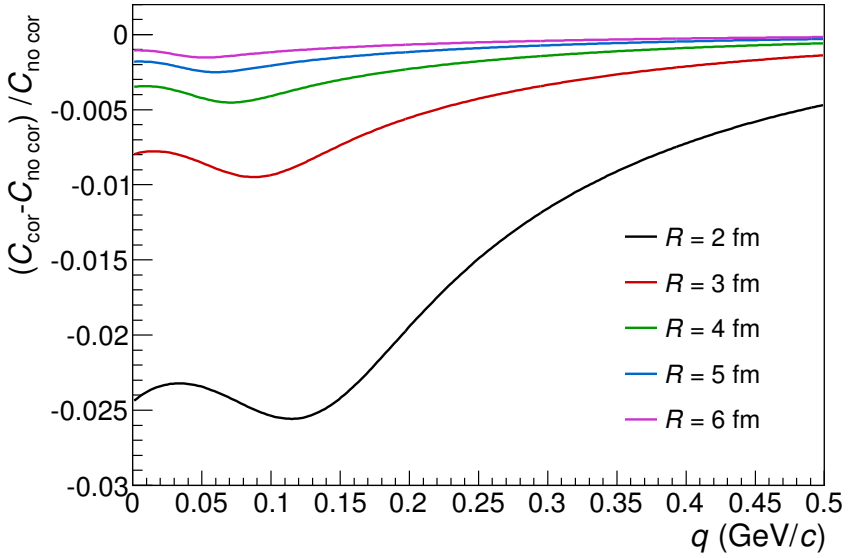

Figure A.2: Correction factor from the inclusion of the small-r^* wavefunction deviation, shown in Eq. A.8. $C_{\rm cor}$ is the full two-channel correlation function including the deviation correction; $C_{\rm no\,cor}$ is without the correction.